5-2020

Impact of magnetocaloric material properties on performance of a magnetocaloric heat pump.

Michael G. Schroeder
University of Louisville

IMPACT OF MAGNETOCALORIC MATERIAL

PROPERTIES ON PERFORMANCE OF A

MAGNETOCALORIC HEAT PUMP

By

Michael G. Schroeder
B.S. University of Toledo
M.S. University of Louisville

A Dissertation
Submitted to the Faculty of the University of Louisville
J.B. Speed School of Engineering
in Partial Fulfillment of the Requirements
for the Degree of

Doctor of Philosophy
in Mechanical Engineering

Department of Mechanical Engineering
University of Louisville
Louisville, KY

May, 2020

IMPACT OF MAGNETOCALORIC MATERIAL PROPERTIES ON

PERFORMANCE OF A MAGNETOCALORIC HEAT PUMP

By

Michael G. Schroeder

B.S. University of Toledo
M.S. University of Louisville

A Dissertation Approved on

Dec 17, 2019

By the Following Dissertation Committee:

_____
Ellen Brehob, Advisor

_____
Erin Gerber, Advisor

_____
Sam Park

_____
Andrea Kelecy

ACKNOWLEDGEMENTS

ABSTRACT

IMPACT OF MAGNETOCALORIC MATERIAL PROPERTIES ON PERFORMANCE OF A MAGNETOCALORIC HEAT PUMP

Michael G. Schroeder

December 17, 2019

In the field of magnetocaloric heat pumps much research has been performed around machine design and theoretical machines, but little has been researched around practical problems such as variability in material properties. The present work defines a simulation tool that has been proven with experimental data. Magnetocaloric material cascades were statistically analyzed and parameterized, such that they could be recreated parametrically using a split Lorentz function with normally distributed parameters. Correlated curve-defining values with standard deviations were used as input into the simulation tool to determine the effect of variation on cooling heat pump performance for a household refrigerator application. A 10% reduction in efficiency and cooling power density occurred on average with the addition of material variability. Data from the study was further used to estimate system magnetic cost at greater than $1500 per heat pump. Strategies for dramatically lowering cost were also shown and discussed, backed by additional simulation data. Finally, a 400% percent increase in cost was shown as a result of material variation at current levels.

TABLE OF CONTENTS

LIST OF FIGURES

1 – INTRODUCTION

1.1 - Motivation

Energy usage has become increasingly scrutinized in all forms, with special emphasis placed on the largest contributors. This scrutiny has largely been a product of global warming concerns which are tied to greenhouse gas emissions from power producing facilities using fossil fuels. Heat pump applications represent up to half of commercial and domestic energy use (Conti et al., 2014). According to U.S. Department of Energy (2012) residential energy consumption was 20.99 quadrillion Btu in 2009, split up as shown in Figure 1.

RESIDENTIAL SITE ENERGY CONSUMPTION BY END USE
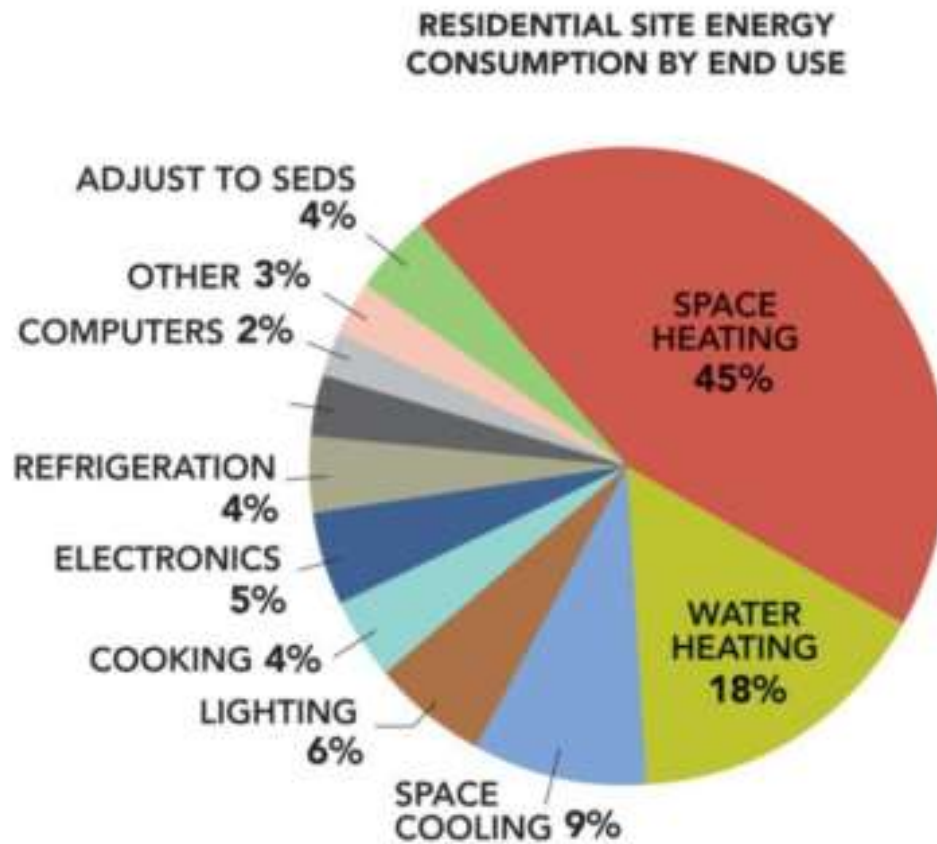
Figure 1: Residential site energy consumption according to U.S. Department of Energy (2012)

Figure 1 demonstrates the magnitude of scale that even a small increase in efficiency can bring, especially in heat pump technology. Energy consumption for spacing heat, space cooling, water heating, and refrigeration all can be directly reduced by improvements in heat pump technology. Many heat pumps utilize a vapor compression cycle, which is at a high degree of maturity, having been in use for the last century. Alternative technologies that may exceed the efficiency of vapor compression heat pumps are attractive as a means for reducing global energy usage.

As a material phenomenon the magnetocaloric effect has been documented for over a century (BUH, 2010). As a means for achieving cryogenic temperatures, the magnetocaloric effect (MCE) has been utilized for several decades (Sager and Paulson, 1982). More recently, materials research has shown that materials can exhibit the magnetocaloric effect near room temperature. This discovery has brought on a new surge of research in the field, focused on replacing vapor compression. In theory a magnetocaloric heat pump can demonstrate efficiency exceeding that of vapor compression (Engelbrecht, 2008; Gschneider Jr. et al., 2005), in excess of 50% of Carnot efficiency.

1.2 – The Magnetocaloric Effect

The magnetocaloric effect is the change in temperature of a material when it is exposed to or removed from a magnetic field. The effect is generally caused by the difference in entropy between a magnetically aligned and a magnetically random structure in magnetic materials. Magnetocaloric materials may exhibit first order phase transitions (FOPT) or second order phase transitions (SOPT), and some materials exhibit both. By definition a first order phase transition material exhibits a discontinuity in the first derivative of Gibbs free energy, while a second order phase transition material exhibits a discontinuity in the second derivative (Aprea et al., 2015). Pecharsky and Gschneidner Jr (1999) created an excellent graphic depicting the transition.
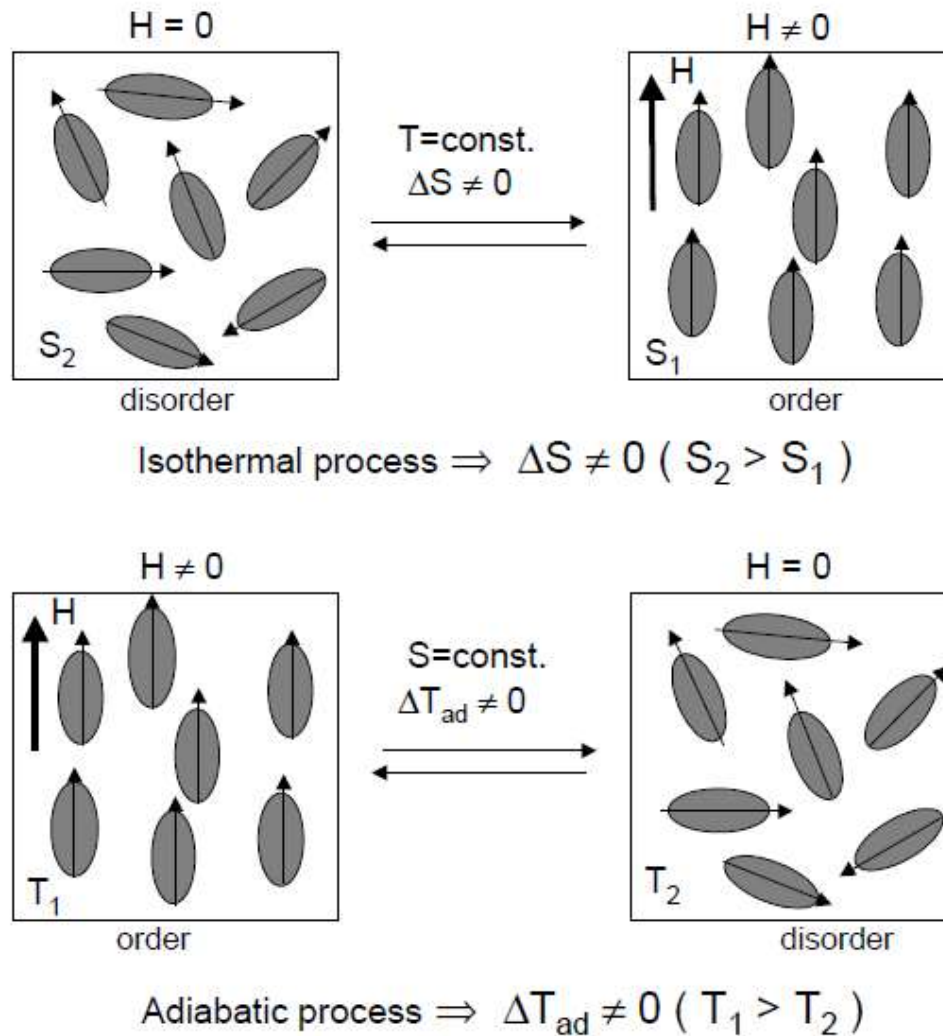
Figure 2: Magnetocaloric effect (Pecharsky and Gschneidner Jr, 1999, figure 1.1)

As seen in Figure 2, a magnetically aligned state has lower entropy level than a magnetically random state. If a material is forced into magnetic alignment with an external magnetic field in an adiabatic environment, the temperature will generally increase, although this can also work in reverse (Tishin and Spichkin, 2003; von Ranke et al., 2009). This occurs because total entropy is conserved in an adiabatic environment with a reversible process. The entropy of any magnetocaloric material (MCM) can be represented as

$$S(T,H) = S_m(T,H) + S_{lat}(T) + S_{el}(T)$$ (1)

where T is absolute temperature, H is magnetic field, S_m is magnetic entropy, S_{lat} is lattice entropy, and S_{el} is electronic entropy (Pecharsky and Gschneidner Jr, 1999). In an adiabatic environment, as magnetic entropy decreases total entropy is maintained. In FOPT materials there may also be changes in lattice entropy, which results in even larger temperature changes, more localized in temperature.
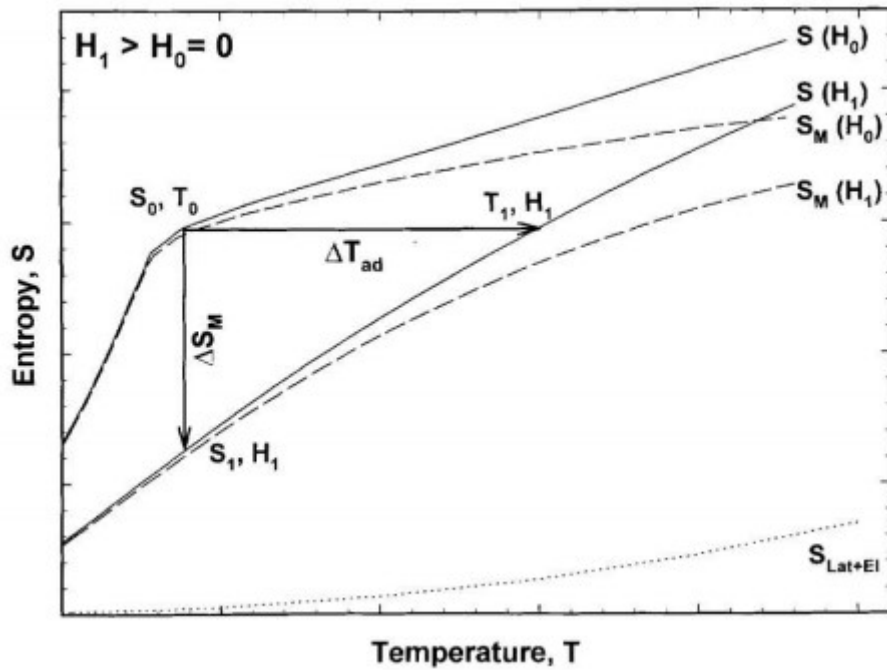
Figure 3: Entropy components as functions of temperature (Pecharsky and Gschneidner Jr, 1999, figure 1.2)

Figure 3 shows each entropy component as a function of temperature, as shown by Pecharsky and Gschneidner Jr (1999). It can be seen that the summation of all entropy components yields the total entropy at any temperature. Each particular magnetocaloric alloy is most active at what is known as Curie temperature. The magnetocaloric effect drops off as temperature deviates from this point. Materials are

5

generally characterized by either adiabatic temperature rise or isothermal entropy change by magnetic field intensity and temperature. These relationships for elemental Gadolinium, a second order material are shown in Figure 4.
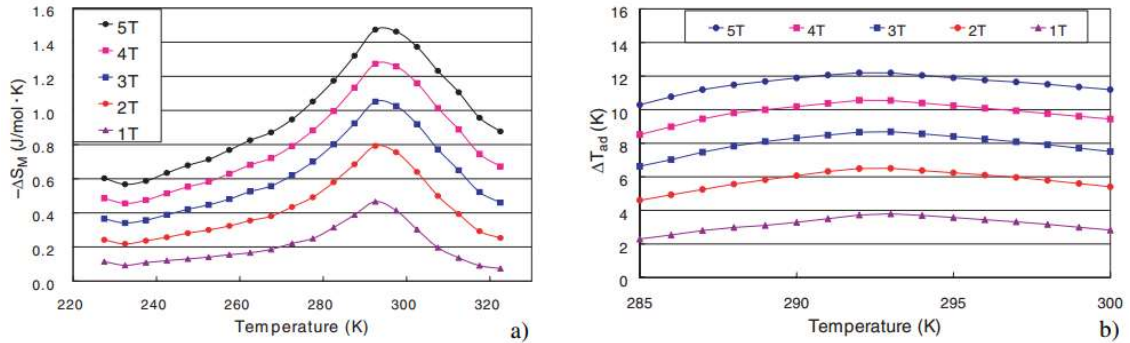
Figure 4: Isothermal entropy change (a) & adiabatic temperature change (b) for Gd (Lee, 2004, figure 2)

The wide peaks shown in Figure 4 are indicative of a SOPT. Typically, materials which exhibit a FOPT have a larger peak value and a much lower peak width than Gadolinium. Material curves vary by composition, but typically the maximum adiabatic temperature change does not exceed 3-4 K at 1 Tesla. Because of the small temperature range of each material's effectiveness, specific materials must be developed which cover the entire desired span of any heat pump device. Materials can be cascaded one after the other to create a larger span than any single material can achieve. A regenerative cycle, first proposed by Brown (1976), can be utilized to keep each section of the cascade near its Curie temperature during operation. An example of a possible five material cascade is shown in Figure 5, of the composition $LaFe_{11.74-y}Mn_ySi_{1.26}H_{1.53}$; where "y" denotes changes in chemical make-up, shown in the subscripts of chemical formula. As opposed to Gadolinium, LaFeMnSiH is a first order material.
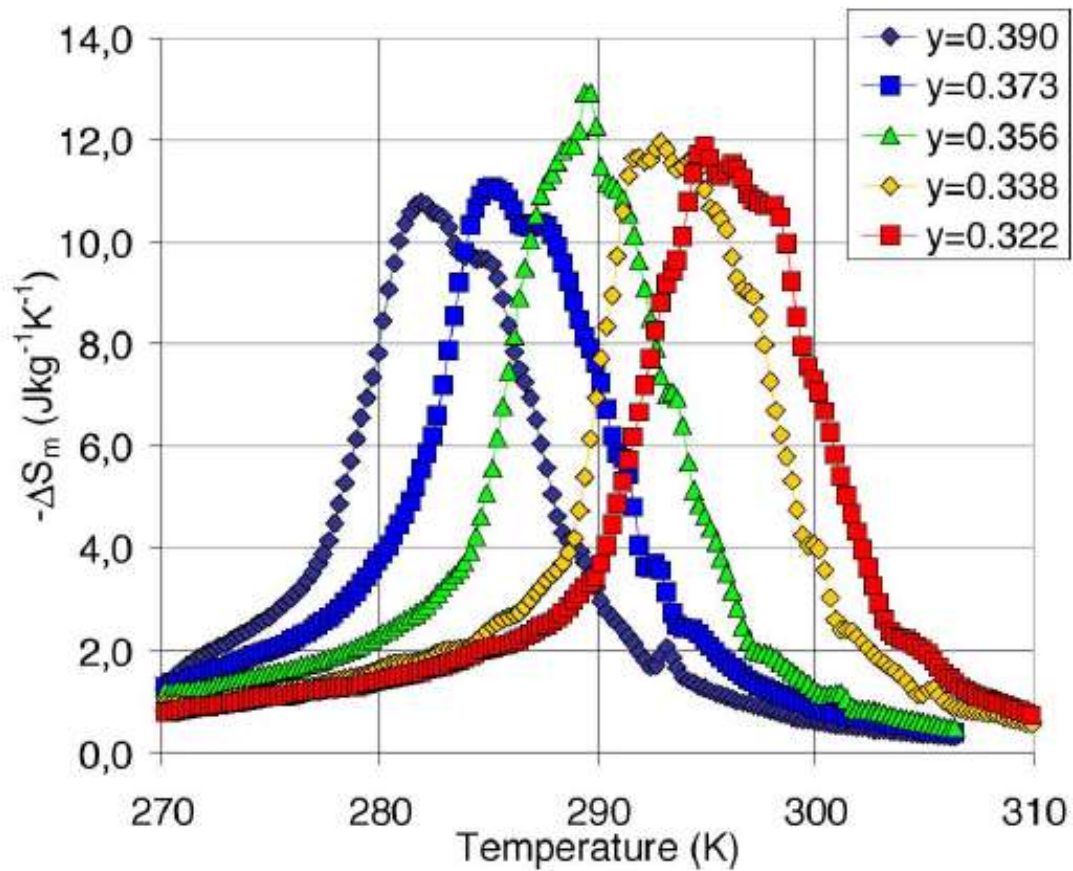
Figure 5: Isothermal entropy change vs. temperature at 1.6 Tesla (Barcza et al., 2011, figure 6)

As shown in Figure 5 each stage of a cascade is able to pump heat through a small portion of the total span of the cascade. If a regenerative cycle is used each stage can operate near its Curie temperature, and a temperature gradient will span the regenerator during steady state operation. The number of stages required is determined by the active span of each material, the total required span of the device, and the amount of overlap required between stages for stability.

1.3 – Magnetocaloric Cycles and Machine Implementation

In order to produce any cycle in a machine, MCM within a container is typically moved relative to a permanent magnetic field. Typically, a fluid is passed across the MCM within the container to affect heat transfer and exchange energy between the MCM and the hot and cold reservoirs. Such an interface between fluid and MCM is known as an active magnetocaloric regenerator (AMR) or regenerator. Two packed bed regenerators within clear tubular containers are shown in Figure 6.
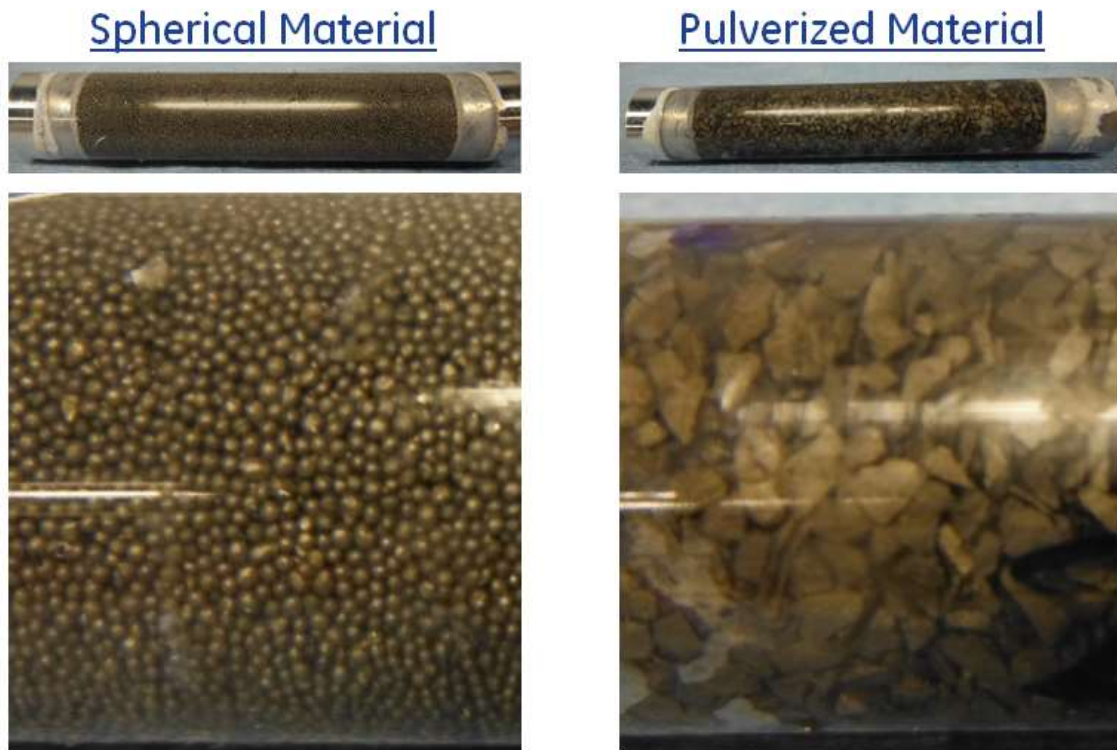
Figure 6: Left, regenerator with spherical particles. Right, regenerators with irregular particles.

Regenerators may utilize packed beds of MCM particle beds as shown in Figure 6, but can alternatively use microchannels, printed structures, or other porous media.

Figure 7: Microchannel regenerator example from Oak Ridge National Labs (Momen, 2017)**.**

An example of microchannels is shown in Figure 7. Microchannel diameter is generally below 1 mm, and typically provides highly efficient, laminar, flow through the media. Heat transfer fluid fills in any volume that is not MCM within the container. A simple example machine cross section is shown in Figure 8. Fluid flow is periodic, but an average temperature gradient exists as is shown; from cold (blue) to hot (red).
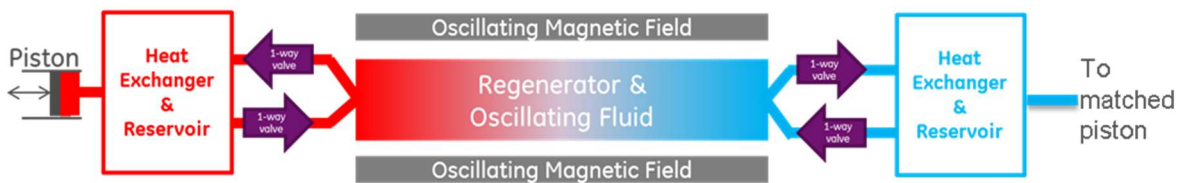
Figure 8: Magnetocaloric heat pump

One-way valves ensure that outgoing fluid must pass through a heat exchanger prior to returning the regenerator. Looking deeper, a typical cycle includes 4 segments. Material is magnetized; MCM and working fluid temperatures rise to high level, Figure 9.
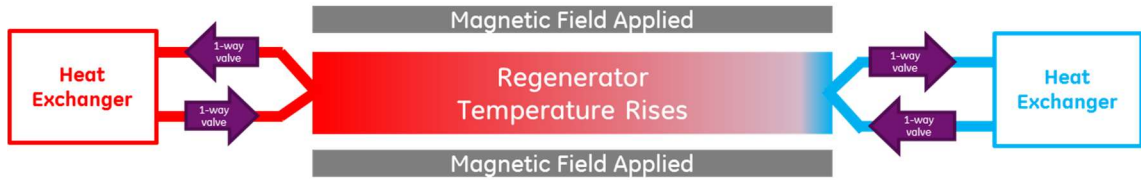
Figure 9: Magnetization, segment 1

Next, some fluid is displaced. Cold fluid enters from the cold side, and heated fluid exits the hot-side. Additionally, the MCM is providing stored heat to the flowing fluid during this period, Figure 10.
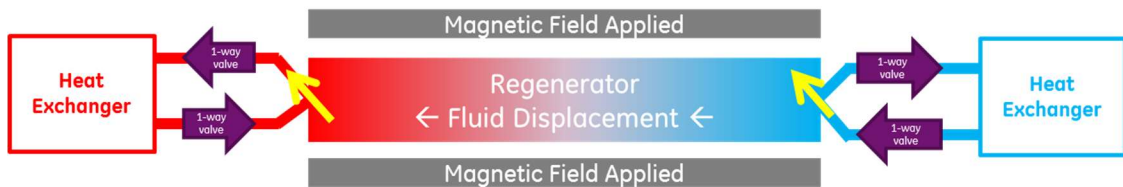
Figure 10: Warm flow, segment 2

Material is demagnetized; MCM and working fluid temperatures fall to low level, Figure 11.
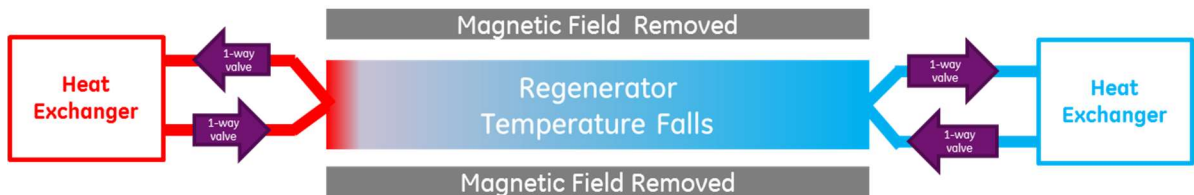
Figure 11: Demagnetization, segment 3

Fluid is displaced in the opposite direction. Warm fluid enters from the hot side, and cooled fluid exits the cold side. Additionally, the MCM is receiving and storing heat from the flowing fluid during this period, Figure 12.
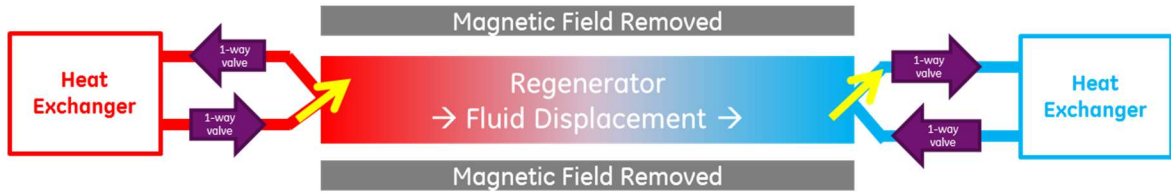
Figure 12: Cold flow, segment 4

The basic cycle shown in figures 9 through 12 was proposed by Barclay (1983) and can be summarized:

1.   Adiabatic magnetization; MCM temperature raises to high level.

2.   Constant magnetization heat transfer; fluid is displaced. Fluid enters from the cold side, and heated fluid exits the hot-side.

3.   Adiabatic demagnetization; MCM temperature falls to lower level than step 1.

4.   Constant magnetization heat transfer; fluid is displaced in the opposite direction. Ambient temperature fluid enters from the hot side, and cooled fluid exits the cold side.

Using a real material with a Curie temperature of 291 K, entropy versus temperature curves have been generated at zero magnetic field and a 1.5 Tesla magnetic field to further illustrate the cycle.
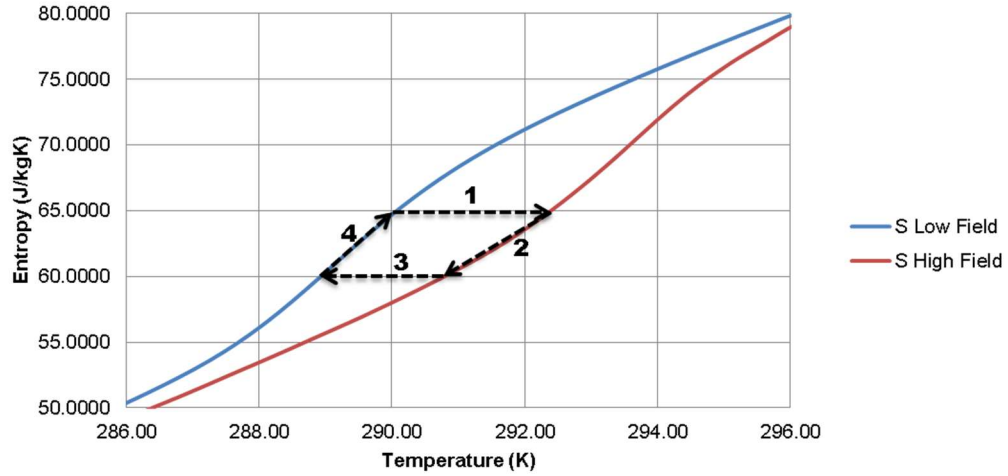
Figure 13: Thermodynamic cycle for idealized regenerative magnetocaloric cycle.

The idealized cycle in Figure 13 exhibits two constant entropy transitions and two constant magnetic field transitions. Cycle steps 1 and 3 are in reality not horizontal lines, because the process is actually not perfectly reversible. By modifying the cycle and allowing heat transfer during magnetic field changes, there is the possibility to achieve a true Carnot cycle.
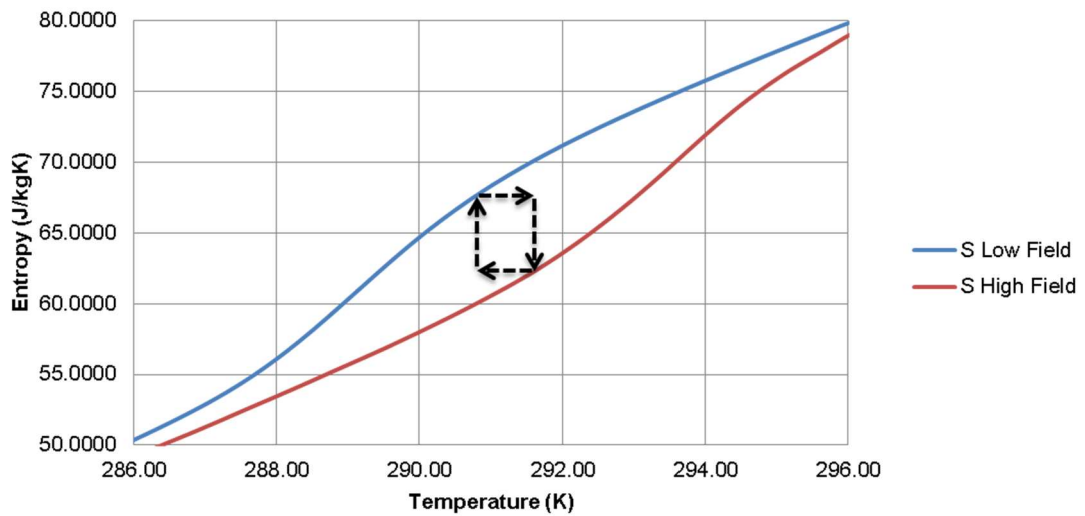
Figure 14: Carnot cycle in magnetocaloric machine

It can be deduced from Figure 14, that a Carnot cycle produces lower cooling capacity but most likely at a higher efficiency. The lengths of lines are short, meaning that less entropy and energy change are observed between steps.

1.4 –Machine Parameters

Performance of machines is often presented as cooling capacity or efficiency as a function of span. A typical performance curve is shown in Figure 15.
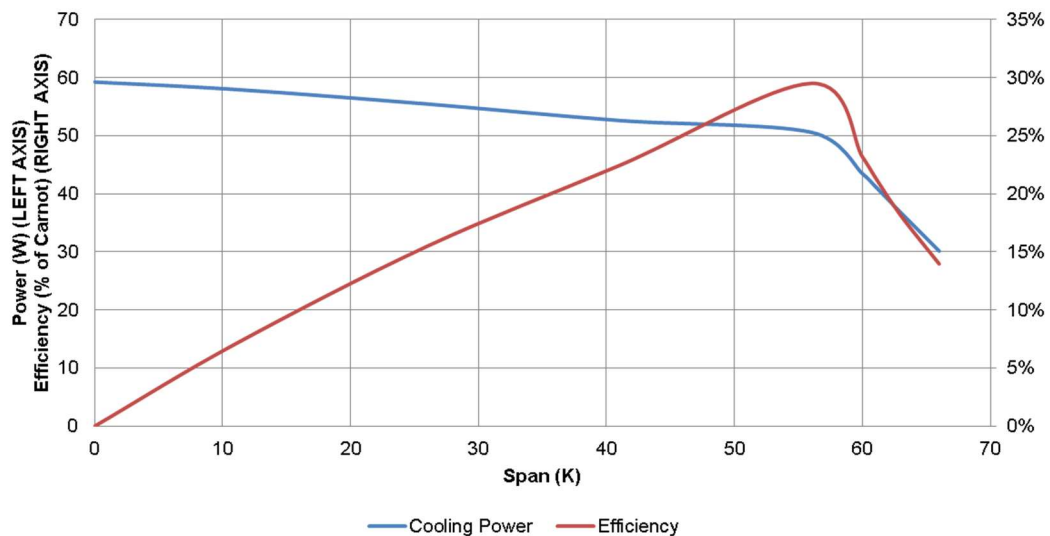
Figure 15: Cooling power and efficiency as a function of span for an arbitrary case.

As shown in Figure 15, performance curves for cooling power have a plateau section across the majority of the cascade span and a sharp drop-off as the cascade span is exceeded. Percent of Carnot efficiency peaks near the end of the cascade span, when all stages are being utilized. Changes in operating or machine parameters have a large impact on both the shape and height of performance curves. Examples of operating parameters include cycle frequency, fluid velocity profile, and magnetic field

profile. Machine parameters encompass regenerator length and cross section area,

MCM channel diameter and shape, rejection temperature, temperature span, and losses

such as heat leak. Many papers show how these various parameters effect

performance (Aprea et al., 2014; Bahl et al., 2014; M.A. Benedict et al., 2016;

Engelbrecht et al., 2011; Rowe and Tura, 2006).

1.5 – The Effect of Magnetocaloric Property Variation

1.5.1 – Causes for Variation in Magnetocaloric Material Properties

In addition to operating parameters and machine geometry, magnetocaloric

material properties effect performance. Causes for variation in material properties for

first order materials can be broken down into three primary categories: physical, purity,

and composition. Generally, manufacturers of MCM utilize all three in order to achieve

desirable properties. A unique combination of process parameters may be required for

each material of a cascade.

The first listed category effecting MCE is physical, which includes the processing

and heat treating involved in reaching the final phase and structure for the desired

material. Generally, there are specific heating and sintering procedures involved for

each composition. Katter et al. (2008) showed how changes in sintering temperature

effect Curie temperature location and maximum effect in LaFeCoSi. Higher sintering

temperature leads to a larger peak effect at a lower absolute temperature. Blázquez et

al. (2015) discussed the need for long annealing processes to achieve a desirable final

effect for the same material family, as can be seen in Figure 16.
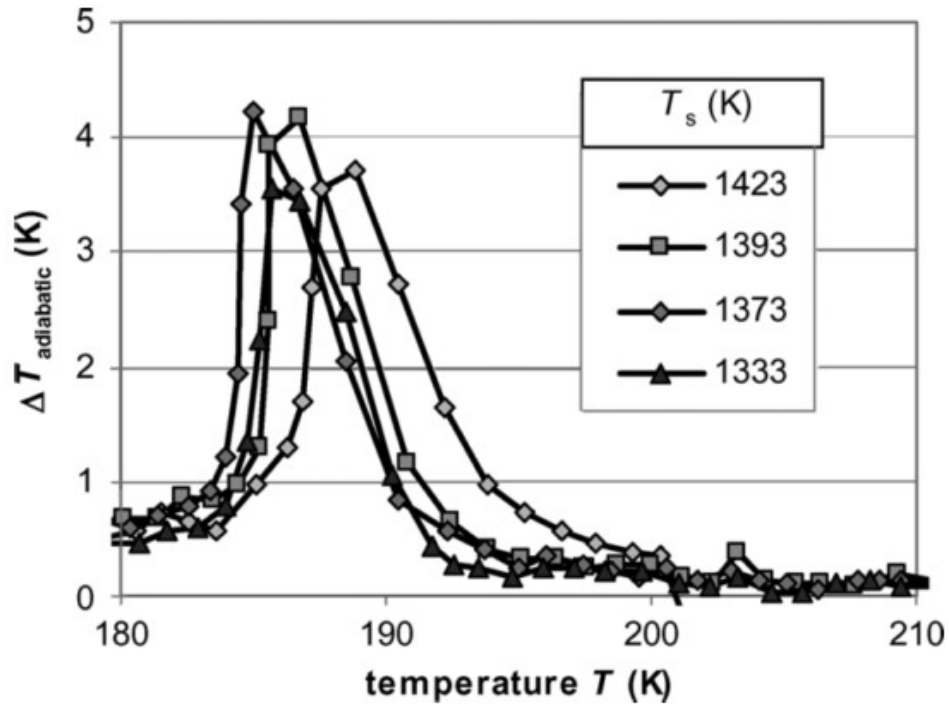
Figure 16: MCE as a function of sintering temperature for LaFeCoSi (figure 3, Katter et al., 2008)

It is clear in Figure 16 that sintering temperature has a strong effect on magnetocaloric effect, or adiabatic temperature change, with a peak effect occurring at 1373 K sintering temperature. Other magnetocaloric materials exhibit similar sensitivities to processing and heat treating as well. Pryds et al. (2011) show that sintering LaCaSrMnO dramatically changes MCE. Heat capacity drops by approximately 20% and MCE increases by about 300%.

The second listed parameter that affects MCE is purity. Impurities are trace elements which are not desired in any amount in the final product. Blázquez et al. (2015) showed how impurities in the Fe phases brought on by aging negatively affect the magnetocaloric properties of the material. If left unprotected in a reactive environment, material properties change, leading to generally less MCE. Dan'kov et al. (1998)

acquired samples of elemental Gadolinium, measured impurity levels, and correlated

various impurities to MCE. Differences in MCE are shown in Figure 17.
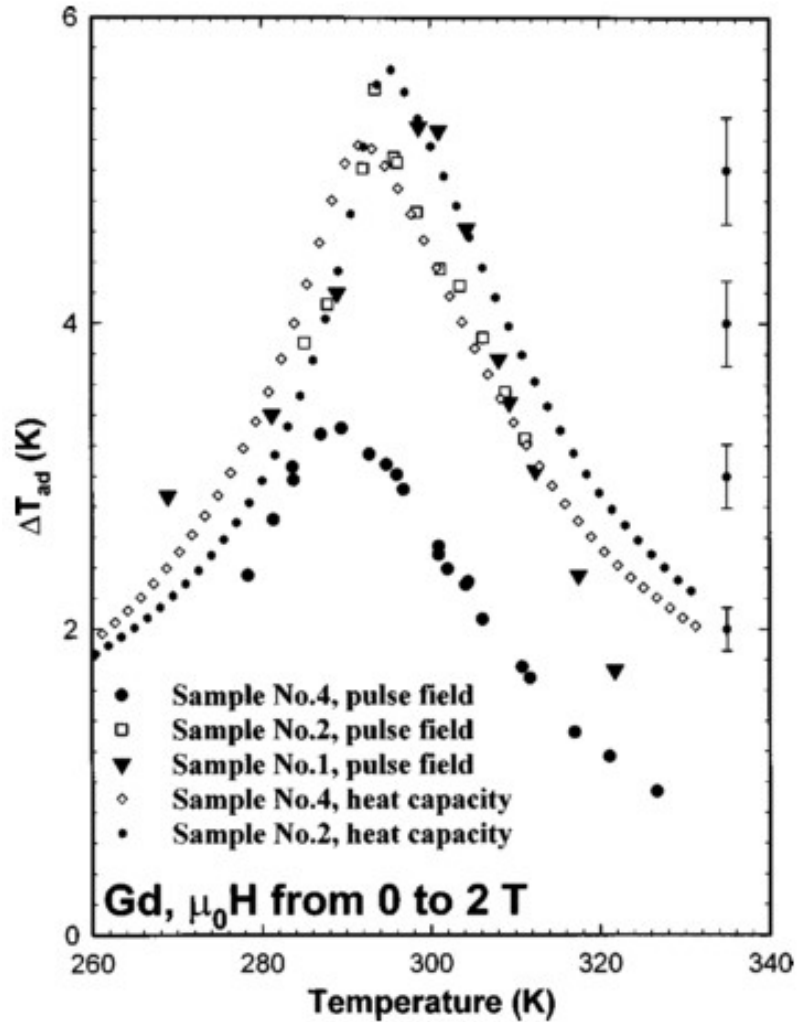
Figure 17: MCE in adiabatic temperature change as a function of temperature and sample. Shown by Dan'kov et al. (1998) as figure 11.

They showed that some impurities are more detrimental than others, and

generally smaller elements produce the largest negative impact on MCE. Hydrogen is

hypothesized to interrupt the crystalline structure and limit transitions in magnetic state,

thus reducing magnetocaloric response. It is therefore critical to limit the addition of impurities throughout the processing and useful lifetime of a magnetocaloric regenerator.

The third category is composition. Materials are composed of a distribution of compositions, and the resulting properties are also a distribution. Composition can change locally and also batch to batch, causing variation that is traceable to many well documented relationships. For instance, in LaEuSrMnO, larger relative fractions of La and smaller relative fractions of Eu provide lower Curie temperatures and wider peaks (Amaral et al., 2008).   Basso et al. (2015) showed the result of varying the amount of Manganese in LaFeMnSiH, as shown in Figure 18.
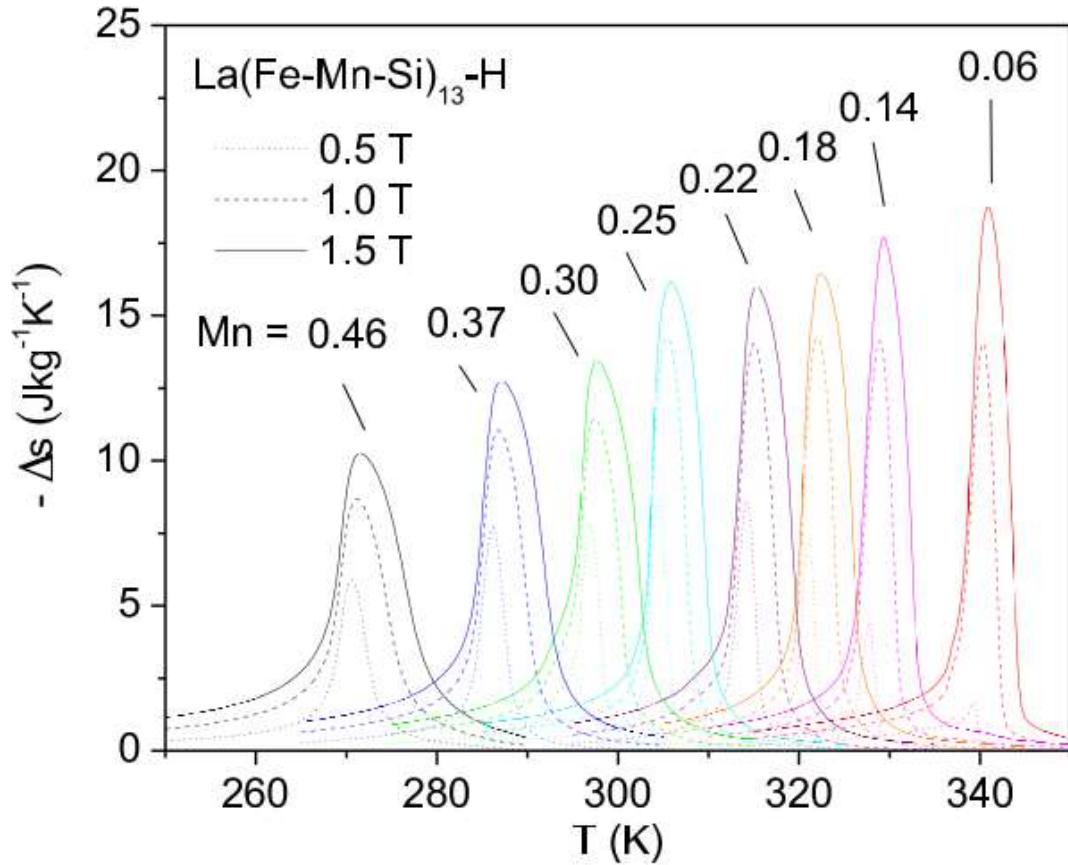
Figure 18: MCE in entropy change as a function of temperature for various compositions of LaFeMnSiH. Presented by Basso et al. (2015) as figure 7.

In Figure 18 it can be observed that changing the composition slightly results in largely differing Curie temperatures and peak MCE. For another composition, LaFeSi, adding controlled amounts of Mn or Co allows the Curie temperature to be varied (Burriel et al., 2011). Similarly, Katter et al. (2008) altered Curie temperature in LaFeCoSi by altering the relative proportion of Co. Dinesen et al. (2005) showed how Curie temperature and peak effect are changed with various quantities of Sr and Ca in LaCaSrMnO. Wang et al. (2011) used various levels of Mn in LaCeFeMnSi to produce different Curie temperatures and peak effects. Barcza et al. (2011) showed similar results with LaFeMnSiH.

All three categories contribute to the final magnetocaloric effect and heat capacity for magnetocaloric materials, and must be adequately tolerance to repeatable achieve the desired outcome. A link between machine performance and material property variation may allow meaningful material production tolerances to be established.

1.5.2 – Previous Work to Predict the Effect of Variation on Machine Performance

In one study the effect of magnetocaloric properties was looked at from a high level without random variation. Lei et al. (2016) generated data for hypothetical mixed first and second order phase transition magnetocaloric materials. A peak function was used to generate hypothetical material curves to assess the tradeoffs of peak width versus peak height. Wide, short, peaks correspond to stronger second order behavior, similar to elemental Gadolinium. Narrow, tall, peaks correspond to stronger first order behavior. Wider peaks allow for farther stage spacing, although peak performance is reduced.

Engelbrecht and Bahl (2010) performed a very similar study, examining the behavior of materials with various peak widths, shown in Figure 19.
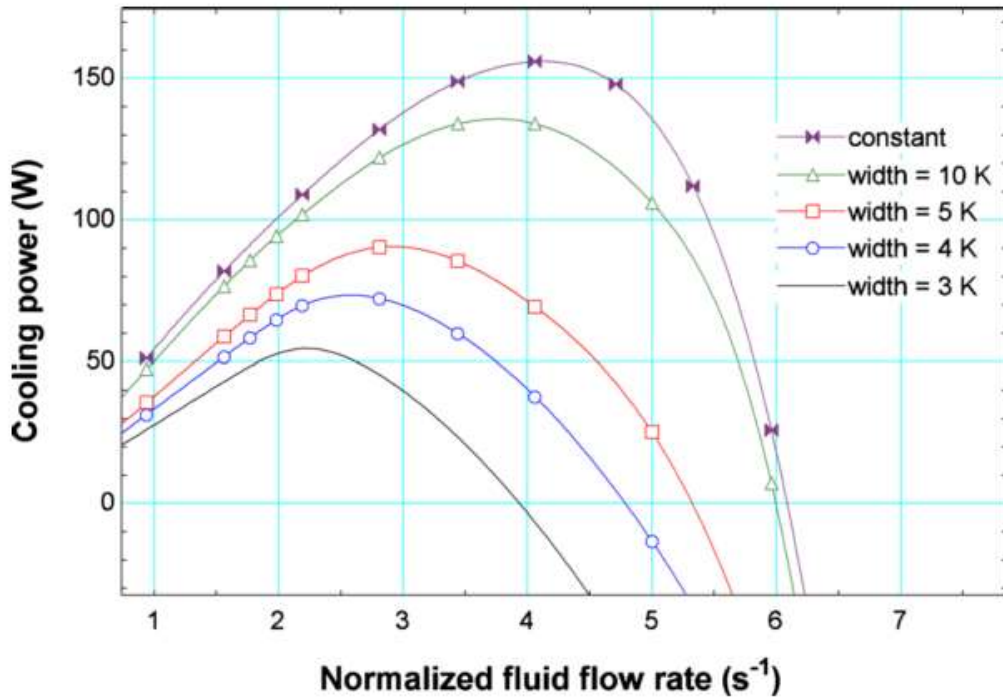
Figure 19: Figure six from (Engelbrecht and Bahl, 2010). Cooling power as a function of flow rate and cascade properties.

As can be seen in Figure 19, they came to the conclusion that wider curves are beneficial to performance so long as peak height remains constant. Wider peaks allow performance to approach that of a constant effect. Here, a constant effect means that a single stage exists that provides the same MCE across all temperatures.

By far, the most relevant previous work for the current proposal is from Lei et al. (2015), which was expanded slightly in (Lei et al., 2016). They simulated the effect of variation in Curie temperature of a 15 layer cascade with identical stages as a uniform distribution, and found nominal cooling power to reduce as standard deviation increased, as shown in Figure 20.
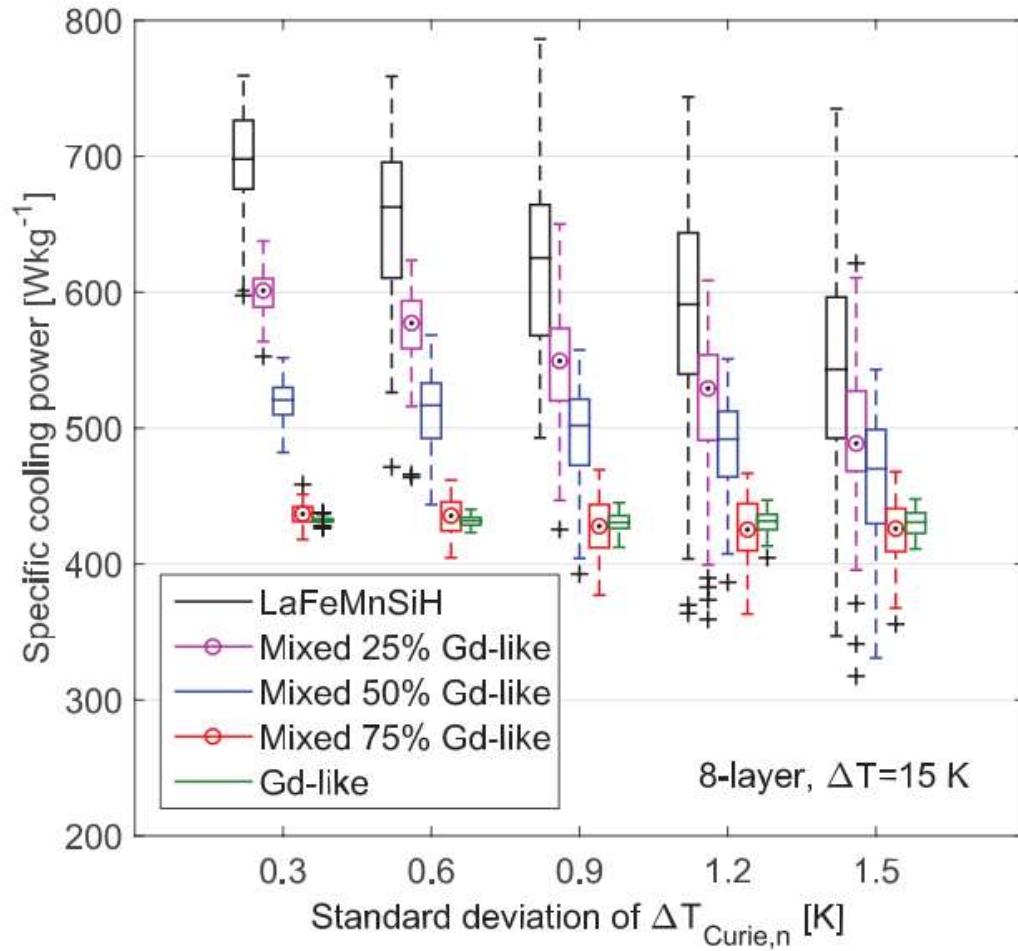
Figure 20: Specific cooling power as function of Curie temperature standard deviation and MCM curve shape (Lei et al., 2015, figure 10).

It can be seen in Figure 20 that SOPT materials such as Gadolinium are largely insensitive to variation in peak location due to the large width of peaks. Whereas a FOPT material with a narrow peak is strongly negatively impacted when stage spacing is uneven. This is due to gaps forming between stages, which force stages to operate off-peak. Also observable in Figure 20 is that output variation increases as standard deviation of Curie temperature increased.

Another observation that they made was that nominal stage spacing can be decreased in order to make the regenerator less sensitive to spacing variation, as shown in Figure 21.
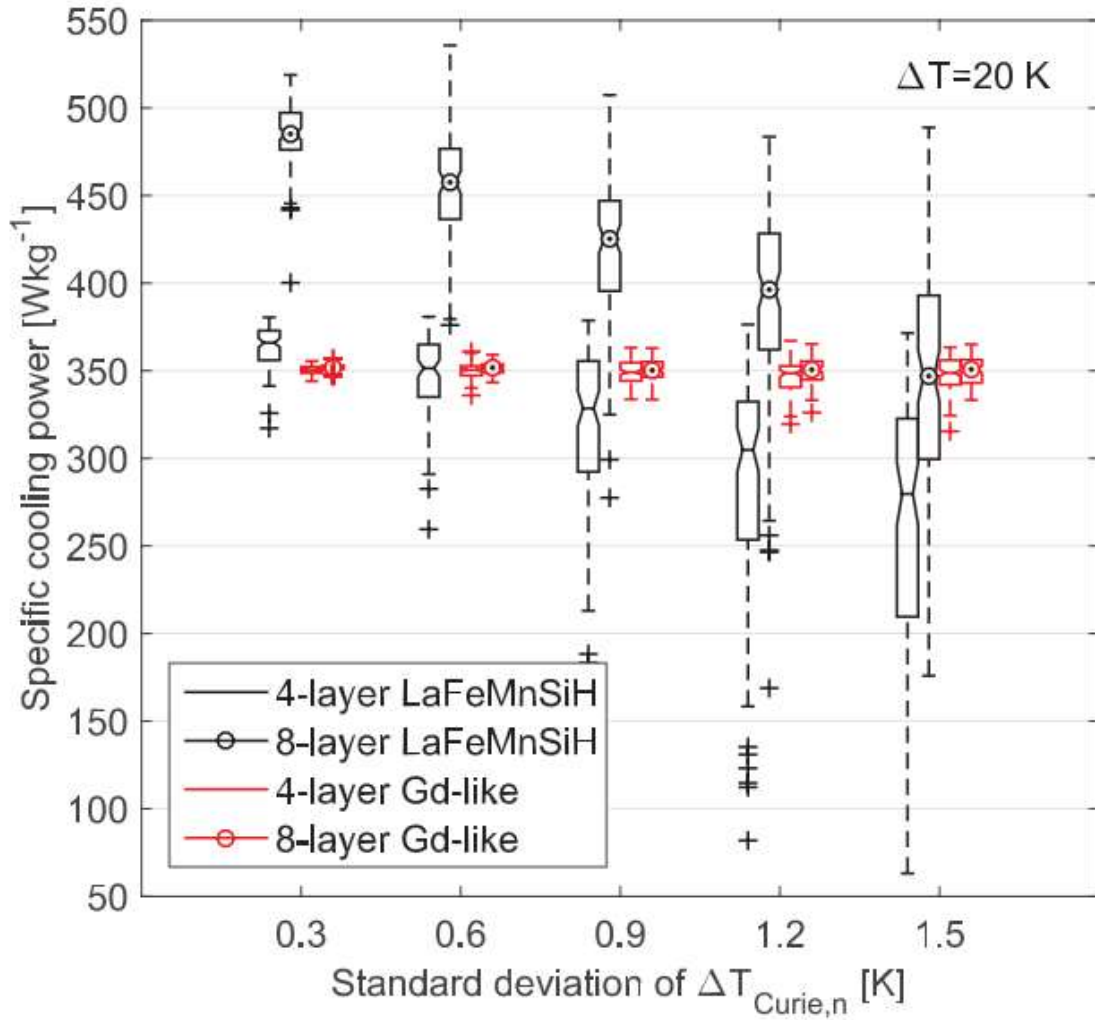
Figure 21: Specific cooling power as a function of Curie temperature standard deviation and stage count (Lei et al., 2015, figure 11).

The 8 stage cascades shown in Figure 21 cover the same span, meaning that nominal stage spacing is tighter. Tighter spacing leads to a mild decrease in sensitivity

to spacing variation. Tolerances are much more critical for FOPT materials, however specific cooling power is much greater than that of SOPT materials.

Variation in peak spacing represents one of the parameters of interest in the proposed study. An important distinction in method is that a normal distribution will be used in the proposed work, as it should better represent variation around target means. A uniform distribution is applicable if materials are generated without good process control, creating a library of existing materials. Cascades are then built using existing materials from library, resulting in a uniform distribution within each target stage.

1.6 – Research Summary and New Contributions

Sections 1.1 through 1.5 lay out current research at a high level, and serve to highlight the lack of research existing relating to material property variation. Specifically, a significant gap exists in the body of knowledge related to the effect material property variation has on machine performance. Previous studies are very limited in parameter ranges, investigating a limited number of parameters with a limited scope, as shown in section 1.5.2. There has been no previous research showing the combined effect of variation in peak location, height, and width for both MCE and heat capacity for a realistic cascaded regenerator. Real materials exhibit trends in nominal peak shape as a function of temperature, whereas previous research has assumed stages to have identical shape regardless of Curie temperature for similar studies. All material characteristics and machine design factors may interact, meaning that they must all be studied simultaneously, which is a contribution of the present work. The working hypothesis is that higher levels of material property variation will lead to a decrease in average and performance while also increasing variability of output performance. In

other words, the distribution of output will spread out and drop as a whole for cooling power density and Carnot ratio , or efficiency. A derivative analysis shows that cost should be the optimized metric in research in order to move magnetocaloric technology nearer to mass production. This broad look at system cost is also a contribution of the present work. Furthermore, the present research aims to enhance the commercial feasibility of magnetocaloric technology by providing variability targets for materials manufacturers, based on projected machine cost. This all is accomplished using measured magnetocaloric materials and a well validated model to run large numbers of simulations on dedicated server computers. No additional physical testing beyond that shown in the validation reference for the model was completed in this work. To summarize the contributions of this research:

1. Compile large cascades of previously unpublished and previously published material data using existing methods to parameterize all material curves. Existing data and parameterization methods were developed by (Benedict et al., 2016a, 2016b).

2. Create basic linear functions to relate curve parameters to material Curie temperature based on least squares regression. These linear functions define nominal material properties and a baseline to which variation can be added.

3. Modify the input method to an existing simulation tool to generate magnetocaloric material cascades based on linear functions relating material property curve parameters and Curie temperature. In addition, include standard deviations to define normally distributed random variation on top of the linear functions.

4. Using the existing simulation tool, simulate a broad design space of magnetocaloric regenerators, varying 9 input parameters across 2 or 3 levels each for a refrigerator application to establish baseline, or zero material variation, performance.

5. Simulate points within the same design space with realistic material variability, as characterized within the present work.

6. Analyze both sets of simulation data and discuss differences. Determine the impact of material variability on cooling power density and efficiency

7. Create and use a magnetic mass function, which translates regenerator size and magnetic field strength into required magnet mass. Estimate magnetic system cost and regenerator cost based on this function and a price per kilogram material cost estimate.

8. Use this cost estimation function to assess the impact of material variability on system cost, and provide high level options to reduce system cost.

2 – SIMULATION TOOL FOR PREDICTING MACHINE PERFORMANCE WITH MAGNETOCALORIC PROPERTY VARIATION

Many simulations have been created to predict performance of magnetocaloric regenerative heat pumps, many of which are based on Engelbrecht (2004). Schroeder and Brehob, (2016) describe the simulation tool that was used as the starting point this study. Various modifications to this tool are detailed in this chapter. Basic interactions include longitudinal mass and heat transfer and radial heat transfer. A regenerator is sliced into longitudinal nodes and further split into fluid and magnetocaloric material nodes radially, resulting in a 1.5-D model.

2.1 – Simulation Inputs

2.1.1 – Geometry, Cycle Definition, and Material Properties

Fluid cycles are defined in the model input file by event start times, ramp times, and peak durations and magnitudes. Magnetic profiles are defined as a square profile

with a start and stop time. An example flow profile can be observed in Figure 22.
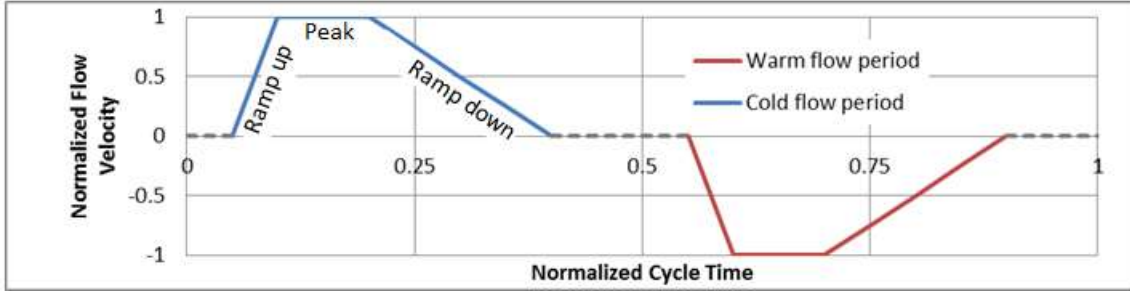
Figure 22: An example fluid velocity profile as defined by ramp start times, ramp durations, peak durations, and peak magnitudes.

For simplicity ramp up and ramp down times will always be equal in this study. Additionally, how and cold flow periods will be held equal in this study for simple parameterization. An entire flow profile is therefore defined by ramp start time, ramp elapsed time, and peak elapsed time. Magnetic profiles are also assumed to be symmetric, and are therefore the square magnetic profile is defined by peak amplitude alone. MCM thermal conductivity and density entered into the program as constants, as are fluid thermal conductivity, density, viscosity, and heat capacity. Geometry parameters such as cross sectional area, regenerator length, fluid fraction, dead volume, and characteristic length are also included in the input file as constants. MCM cascade information is also entered, which is further described in section 2.1.2.

2.1.2 – Magnetocaloric Material Cascade Definition

Material information is also read in parametrically, and additional inputs allow these parameters to vary as functions of stage temperature to emulate real data. Standard deviations for cascade inputs may also be entered to show the effect of MCM variability. As shown by Benedict et al. (2016), four parameters appropriately describe

27

material temperature response curves: peak height A, peak location T_c, half width at half max (HWHM) W, and skew S. These parameters are denoted in Figure 23.
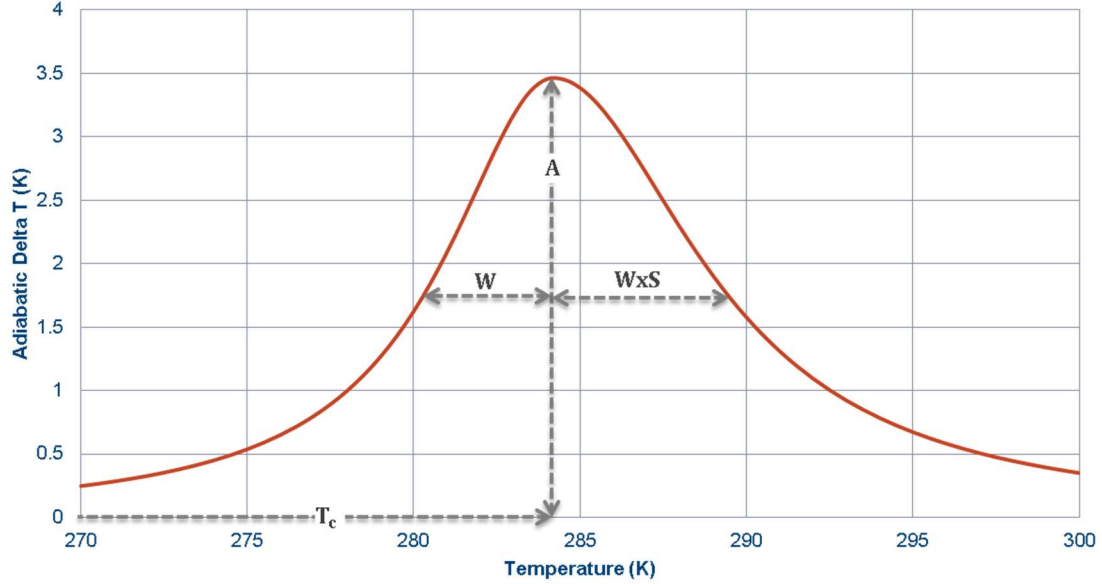
Figure 23: Magnetocaloric material characteristic curve, where W is HWHM, S is skew, A is amplitude or peak height, T_c is peak temperature.

It can be observed in Figure 23 how curve shape is defined by these parameters. Heat capacity as a function of temperature follows the same shape, with the addition of base height. Base height simply raises the tails of the function to a non-zero asymptote. These terms were chosen as they directly represent easily distinguishable characteristics of material temperature response and heat capacity curves, and they provide a good fit for first order materials (Benedict et al., 2016). Parameters in Figure 23 come from a Split Lorentz distribution, represented by

$$\textbf{Split Lorentzia} \quad \begin{cases} \left\{ \dfrac{A-B}{\left(\frac{T-Tc}{W}\right)^2+1} + B \right\} & \textbf{For T} < \textbf{Tc} \\[4mm] \left\{ \dfrac{A-B}{\left(\frac{T-Tc}{WS}\right)^2+1} + B \right\} & \textbf{For T} \geq \textbf{Tc} \end{cases} , \qquad (2)$$

28

where A is peak amplitude, B is base or minimum asymptotic level, T is temperature, T_c is Curie temperature, W is peak width at half max, and S is skew or the ratio of width left of peak to width right of peak. Beyond the description of individual temperature response and heat capacity curves, additional parameters were added to represent characteristics of full cascades of materials. Natural trends generally occur in peak height as Curie temperature is varied from warm to cool. Many of these are described in detail in referenced articles from section 1.5. In the current work these trends are created by defining each material curve parameter at both the highest and lowest Curie temperature stages. Intermediate stages are generated using basic linear interpolation of parameters.
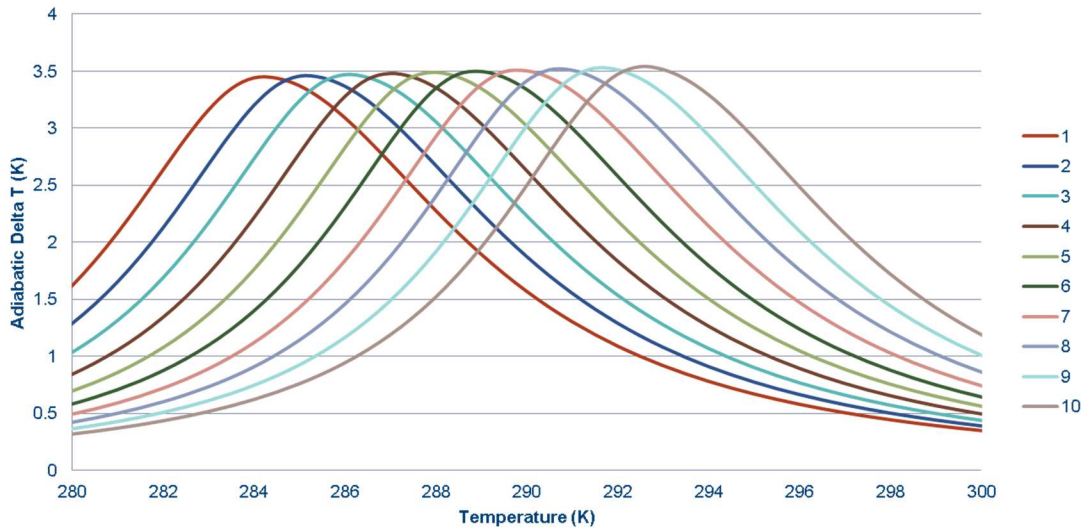
Figure 24: Cascade of magnetocaloric materials without variation

As shown in Figure 24, with zero random variation height of all curves in a cascade follow a linear gradient. The same is done with peak width and base as appropriate. This provides good nominal trends onto which random variation in properties can be superimposed.
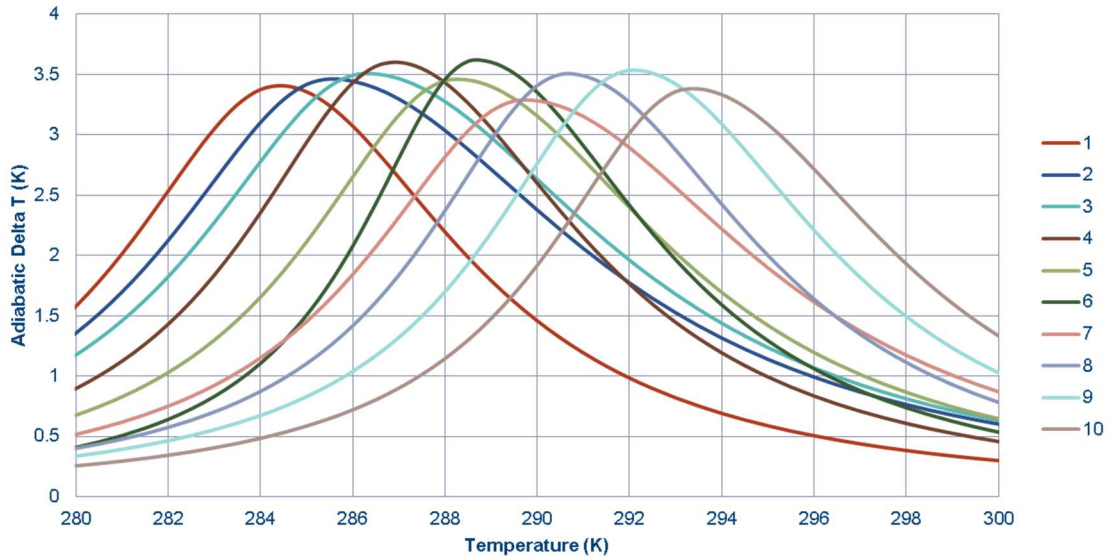
Figure 25: Cascade of magnetocaloric materials with simulated variation

In Figure 25, the same cascade parameters from Figure 24 were used with the addition of random variation in material curve parameters. With variation implemented randomly for every stage, properties are no longer well matched from stage to stage. Furthermore, stages are no longer evenly spaced, having variation around the target peak temperature T_c for each respective stage. Each parameter has the same standard deviation across all stages, but each stage will have a unique parameter value within the prescribed normal distribution defined by standard deviation and mean. Each unique parameter value is recalculated every time the program is run. To show the effectiveness of applying normally distributed randomness, Figure 26 contains the real material data that was analyzed to generate Figure 25.
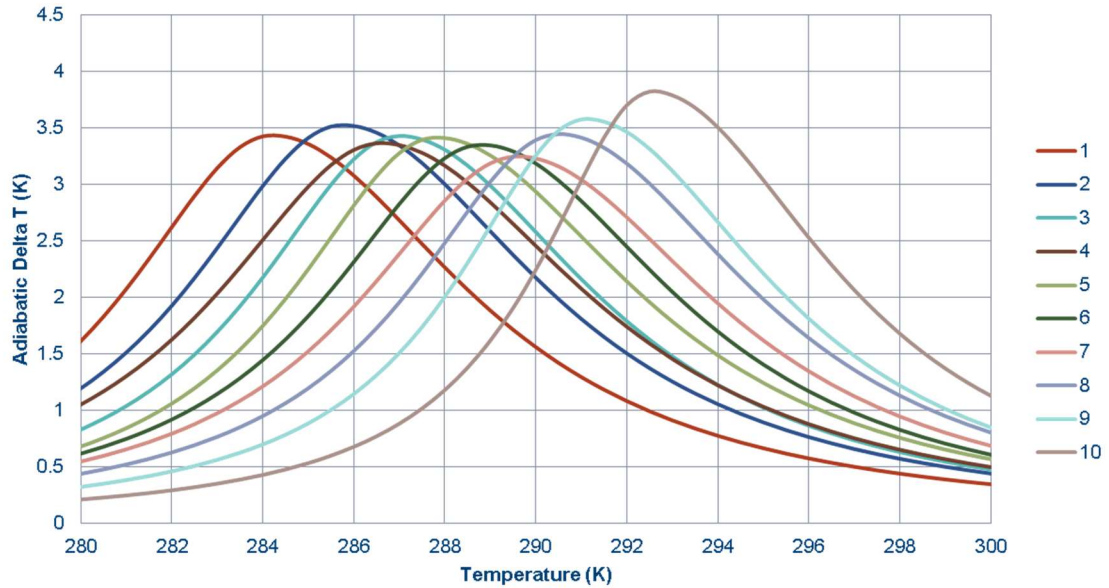
Figure 26: Real cascade of magnetocaloric materials

Figure 26 shows the original data from in M.A. Benedict et al. (2016). It can be observed that the real and randomly generated cascades are qualitatively similar in Figure 25 and Figure 26, having the same nominal values and standard deviations for all curve parameters.

In summary, a simulated cascade is defined by stage count, standard deviation of MCE peak amplitude, standard deviation of MCE peak width at half max, standard deviation of heat capacity peak amplitude, standard deviation of heat capacity peak at half max, standard deviation of Curie temperature, hottest and coldest stage nominal Curie temperature, hottest and coldest stage nominal MCE peak amplitudes, hottest and coldest stage nominal MCE peak widths at half max, hottest and coldest stage nominal heat capacity peak amplitudes, and hottest and coldest stage nominal heat capacity peak widths at half max. Heat capacity base level is constant for all stages within the cascade, and skew is neglected.

31

2.2 - Assumptions

In order to maintain model simplicity, the following assumptions are made:

1. All materials are incompressible.

2. Fluid properties are constant with temperature and pressure.

3. MCM density and thermal conductivity are constant.

4. MCE is applied as an instantaneous change in temperature, and is isentropic.

5. The ends of the regenerator are adiabatic and the only energy exchanged with the hot and cold reservoir occurs via heat carried by moving fluid across the regenerator ends.

6. There is no radial heat leak to the environment.

7. The AMR container does not interact with the AMR fluid or MCM.

2.3 - Magnetocaloric Effect Scaling and Derivation

Magnetocaloric properties are generated using a Split Lorentz function as arrays of adiabatic temperature rise on magnetization and heat capacity at zero magnetic field, both as a function of temperature. Adiabatic temperature rise is then scaled to the proper peak magnetic field strength using two thirds scaling,

$$\Delta T_{adiabatic \atop 0-H2} = \Delta T_{adiabatic \atop 0-H1} \left(\frac{H_2}{H_1}\right)^{2/3} \quad\quad\quad (3)$$

where H_2 is the simulated field strength in Tesla, H_1 is the input data field strength, $\Delta T_{adiabatic \atop 0-H1}$ is the input adiabatic temperature rise data, and $\Delta T_{adiabatic \atop 0-H2}$ is the scaled adiabatic temperature rise.

Two thirds scaling has been shown to be a good thermodynamic approximation for second order materials such as Gadolinium, and can still be used under certain conditions on first order materials with minimal error (Smith et al., 2014). Low to high field temperature change due to the magnetocaloric effect is define using a Lorentzian function as

$$\Delta T_{L \to H}(T) = \left\{ \frac{A_T}{\left(\frac{T - T_{TP}}{2W_T} \right)^2 + 1} \right\}, \tag{4}$$

$$A_T = \Delta T_{adiabatic}, \tag{5}$$
$$ _{0-H2}$$

where T_{TP} is peak temperature, and W_T is peak width at half amplitude. The assumption of reversibility can be applied to temperature change in either direction. Peak amplitude and width must be identical in either direction, and peak location must be shifted by peak amplitude. High field to low field temperature change is therefore defined using the same parameters as low to high field temperature change,

$$\Delta T_{H \to L}(T) = \left\{ \frac{-A_T}{\left(\frac{T - T_{TP} - A_T}{2W_T} \right)^2 + 1} \right\}. \tag{6}$$

Low field heat capacity function is similarly defined as

$$C_L(T) = \left\{ \frac{A_{CL} - B}{\left(\frac{T - T_{CLP}}{W_{CL}} \right)^2 + 1} + B \right\}, \tag{7}$$

where A_{CL} is low field heat capacity amplitude, B is low field heat capacity base, T_{CLP} is low field heat capacity peak temperature, and W_{CL} is low field heat capacity peak width

at half amplitude. Each stage may have unique parameters describing the Lorentzian functions.

High field heat capacity must still be calculated by assuming isentropic and adiabatic transitions between magnetic states. In order to force thermodynamic consistency, total entropy during magnetization and demagnetization is held constant, generally following a method proposed by Pecharsky et al. (2001). High field entropy is calculated by shifting the low field entropy by the adiabatic change in temperature. For example, at 300K a 3K adiabatic temperature rise is observed in a material on magnetization. The low field entropy at 300K must then match the high field entropy at 303K for the transition to be isentropic. Adiabatic temperature change on demagnetization can be found from low and high field entropy in a similar fashion. Entropy at the low field state is calculated using the definition of heat capacity,

$$dS = \frac{C_L \, dT}{T}$$
(8)

where C_L is low field heat capacity, and T is absolute temperature.

2.4 - Governing Equations

One MCM node and one fluid node are represented at each axial location. A basic schematic of interactions is shown in Figure 27. Only three node locations are shown for simplicity.
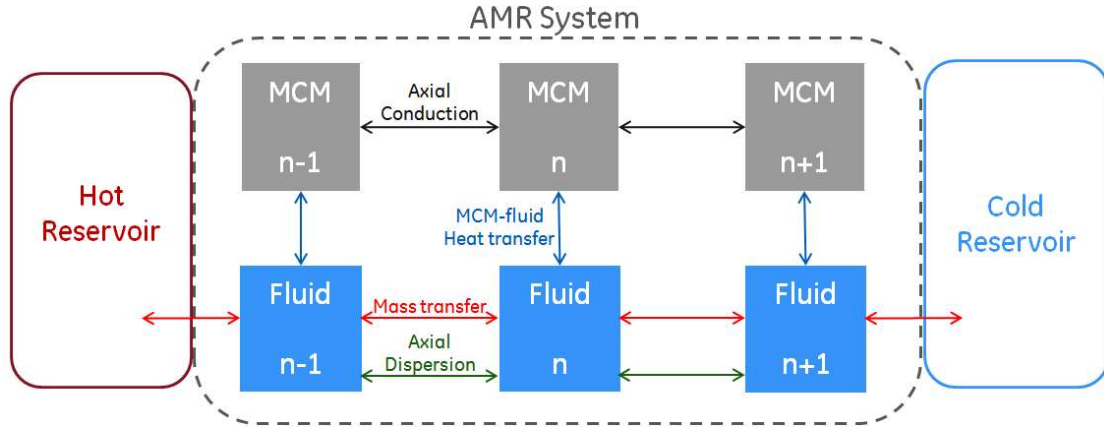
Figure 27: Modeled interactions between nodes within the AMR, as well as interactions between the AMR and the hot and cold reservoirs.

Not shown in the Figure 27 but included in the model is the application of viscous heating and the MCE. In a real machine the MCE is magnetic work coming from the magnetization system. Viscous heating is applied as a generation term in the fluid nodes during fluid flow, and corresponds in a real machine to fluid pumping power. When combined with node thermal mass a set of equations can be used to calculate rate of temperature change of each node due to all effects combined. Fluid node temperature changes are calculated using

$$\partial T_{\substack{fluid \\ node}} = \left(\left(\frac{\partial T}{\partial t}\right)_{\substack{mass \\ trans.}} + \left(\frac{\partial T}{\partial t}\right)_{\substack{fluid \\ MCM-f \\ heat \\ trans.}} + \left(\frac{\partial T}{\partial t}\right)_{\substack{fluid \\ axial \\ disp.}} + \left(\frac{\partial T}{\partial t}\right)_{\substack{viscous \\ heating}} \right) \partial t. \tag{9}$$

Solid node temperature changes are calculated using

$$\partial T_{\substack{MCM \\ node}} = \left(\left(\frac{\partial T}{\partial t}\right)_{\substack{MCM \\ axial \\ cond.}} + \left(\frac{\partial T}{\partial t}\right)_{\substack{MCM \\ MCM-f \\ heat \\ trans.}} \right) \partial t + \partial T_{MCE}, \tag{10}$$

35

where ∂T_{MCE} is temperature change due to the magnetocaloric effect and a change in magnetic field and other parameters are defined below.

2.4.1 - Fluid Nodal Temperature Change Rate Components

Next the individual components are defined. Fluid temperature change rate due to mass transfer during flow in the positive "x" direction is defined as

$$\left(\frac{\partial T}{\partial t}\right)_{\substack{mass \\ trans.}} = \frac{v_{sf}}{L_{node}\,\varepsilon}\left(T_{n_f+1} - T_{n_f}\right) \tag{11}$$

where v_{sf} is superficial fluid velocity, L_{node} is node length, ε is fluid fraction of the packed bed, T_{n_f} is current node temperature, and T_{n_f+1} is adjacent node temperature (see Figure 27). During flow in the negative "x" direction T_{n_f+1} is replaced with T_{n_f-1}.

Temperature change rate of fluid due to MCM to fluid heat transfer is defined as

$$\left(\frac{\partial T}{\partial t}\right)_{\substack{fluid \\ MCM-f \\ heat \\ trans.}} = \frac{UA_{MCM-f}}{\rho_f\,V_{node}\,C_f\,\varepsilon}\left(T_{n_{MCM}} - T_{n_f}\right) \tag{12}$$

where ρ_f is fluid density, V_{node} is total node volume, $T_{n_{MCM}}$ is temperature of the co-located MCM node, UA_{MCM-f} is thermal conductance between MCM and fluid in W/K, and C_f is fluid heat capacity. Temperature change rate of fluid due to axial dispersion is defined as

$$\left(\frac{\partial T}{\partial t}\right)_{\substack{fluid \\ axial \\ disp.}} = \frac{k_{eff}}{L_{node}^2\,\rho_f\,C_f\,\varepsilon}\left(T_{n_f+1} - 2T_{n_f} + T_{n_f-1}\right) \tag{13}$$

where k_{eff} is axial dispersion coefficient. The final fluid component is viscous heating, defined as

$$\left(\frac{\partial T}{\partial t}\right)_{\substack{viscous \\ heating}} = \frac{\Delta P_{node}\, v_{sf}}{L_{node}\, \rho_f\, C_f\, \varepsilon} \qquad (14)$$

where ΔP_{node} is pressure change across a node length.

2.4.2 - MCM Nodal Temperature Change Rate Components

Temperature change rate of MCM due to axial conduction is defined as

$$\left(\frac{\partial T}{\partial t}\right)_{\substack{MCM \\ axial \\ cond.}} = \frac{k_{MCM}}{L_{node}^2\, \rho_{MCM}\, C_{MCM}} \left(T_{n_{MCM}+1} - 2T_{n_{MCM}} + T_{n_{MCM}-1}\right) \qquad (15)$$

where k_{MCM} is MCM thermal conductivity, ρ_{MCM} is MCM density, and C_{MCM} is MCM heat capacity. Temperature change rate of MCM due to MCM to fluid heat transfer is defined as

$$\left(\frac{\partial T}{\partial t}\right)_{\substack{fluid \\ MCM-f \\ heat \\ trans.}} = \frac{UA_{MCM-f}}{\rho_{MCM}\, V_{node}\, C_{MCM}\,(1-\varepsilon)} \left(T_{n_f} - T_{n_{MCM}}\right). \qquad (16)$$

2.4.3 - Correlations and Supporting Equations

Heat transfer coefficient multiplied by area for a given AMR volume is calculated using a relationship based on the work of Hausen (1943),

$$UA_{MCM-f} = \frac{6(1-\varepsilon)}{\left[D^2\left(\frac{1}{3.66 k_f} + \frac{1}{6\,k_{MCM}}\right)\right]} \qquad (17)$$

where D is channel diameter, Re is Reynolds number, and Pe is Peclet number. Axial dispersion is also calculated assuming laminar developed flow,

$$k_{eff} = k_f \left(1 + \frac{Re^2\, Pr^2}{192}\right) \qquad (18)$$

In this case k_{eff} is the effective thermal conductivity in the axial direction of flowing fluid.

Finally, pressure drop across each node is also defined assuming laminar flow, as

$$\Delta P_{node} = \frac{64\rho L v^2}{Re\ D} \tag{19}$$

where ρ is fluid density, L is node length, v is fluid channel velocity, Re is Reynolds number, and D is channel diameter.

2.5 - Time Stepping, Single Case Convergence, and Accuracy Validation

An explicit Euler method is used for time stepping, following a trial-and-error study to determine the best numerical method. Higher order methods had minimal effect on numerical accuracy while increasing computation time. Absorbed heat, rejected heat, magnetic work input, and viscous heat generation, and coefficient of performance (COP) are all calculated each cycle. Absorbed and rejected heat are calculated by summing fluid energy as it crosses the cold-side and hot-side boundaries using heat capacity, density, volume exchange, and temperature.

$$E_{fluid\ cycle} = \sum_0^{cycle\ time} \rho V C(T - T_{res}) \tag{20}$$

where ρ is fluid density, V is fluid displacement for each time step, C is specific fluid heat capacity, T is fluid tempereature, and T_{res} is reservoir temperature. $E_{fluid\ cycle}$ can be replaced by $E_{cold\ cycle}$ or $E_{hot\ cycle}$ to represent either accepted or rejected heat respectively. Magnetic work is calculated as

$$E_{magnetic\ cycle} = E_{hot\ cycle} - E_{cold\ cycle} - E_{viscous\ cycle} \tag{21}$$

Viscous heating is simply integrated across all nodes at each time step and summed at the end of each cycle.

$$E_{viscous\ cycle} = \sum_0^{dx=L_{regen}} \sum_0^{t=cyc\ time} 128 \frac{\mu \dot{V}^2\ dx\ dt}{\pi D^4} \qquad (22)$$

where μ is dynamic fluid viscosity, $\dot{V}$ is volume rate of fluid flow, D is channel diameter, dx is node length in the flow direction, and dt is time step. Energy per cycle can be transformed into power, or energy rate, by multiplying by frequency. For instance,

$$\dot{E}_{cooling} = f\ E_{fluid\ cycle \atop cold} \qquad (23)$$

Simulation cases are considered converged when the change in cooling capacity and rejected heat per iteration are below 0.1% of respective absolute values. Convergence acceleration is applied to reduce computation time, and is described in detail in Schroeder and Brehob (2016).

This model was used by Benedict et al. (2016a, 2016b), and showed that when the machine and materials used are well understood the model predicts within 5% of actual measured values for a range of design and operational parameters. Within the referenced study, magnetic levels tested were 1.1 and 1.5 Tesla. Fluid velocity ranged from 0.05 to 0.10 m/s. Displacement ranged from 10% to 26% of total regenerator fluid. Void fraction was 0.43. Materials tested include MnFePAs and LaFeSiH, both material families used in the present work. Accuracy is expected to remain high for the remainder of the present work because input parameters are always near previously studied values. Utilizing microchannel geometry as opposed to a packed bed actually removes reliance on assumptions of particle size distribution and shape as well, which would be expected to lead to further improvement in output accuracy. Microchannel correlations

within the fully laminar flow regime are not nearly as varied as those used for packed

beds of irregular particles, which is the basis for this statement.

2.6 – Top Level Convergence

After creating a cascade with material property variation and reading in other

machine design input parameters, the program runs until convergence, representing one

iteration. $E_{hot\ cycle}$, $E_{cold\ cycle}$, $E_{magnetic\ cycle}$, $E_{viscous\ cycle}$, and COP are output from the

program for each iteration. If any cascade standard deviation parameters are non-zero

this process must be repeated to assess the effect of input variability. Each iteration a

new randomly generated Gaussian based cascade is made, resulting in each iteration

having different output. Statistics are calculated on all iterations' outputs for each design

point. For instance, cooling power for 10 iterations of a single design point can be

described by mean and standard deviation, thus providing the outcome of the simulated

material curve parameters' standard deviations and means. Figure 28 shows this

process graphically, starting with an input file with nominal design points and mean and

standard deviation values for all material properties' curve parameters.
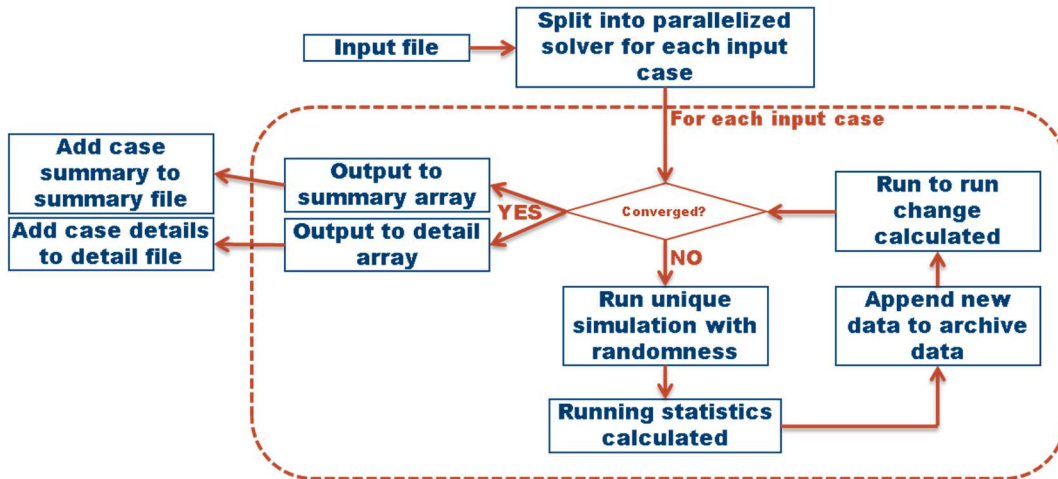
Figure 28: Flow of logic for variation program, from start to statistical output.

As shown in Figure 28, each design point with prescribed levels or material curve variation is simulated repeatedly until output standard deviation and mean stop changing. Figure 29 shows top level convergence for an example case.
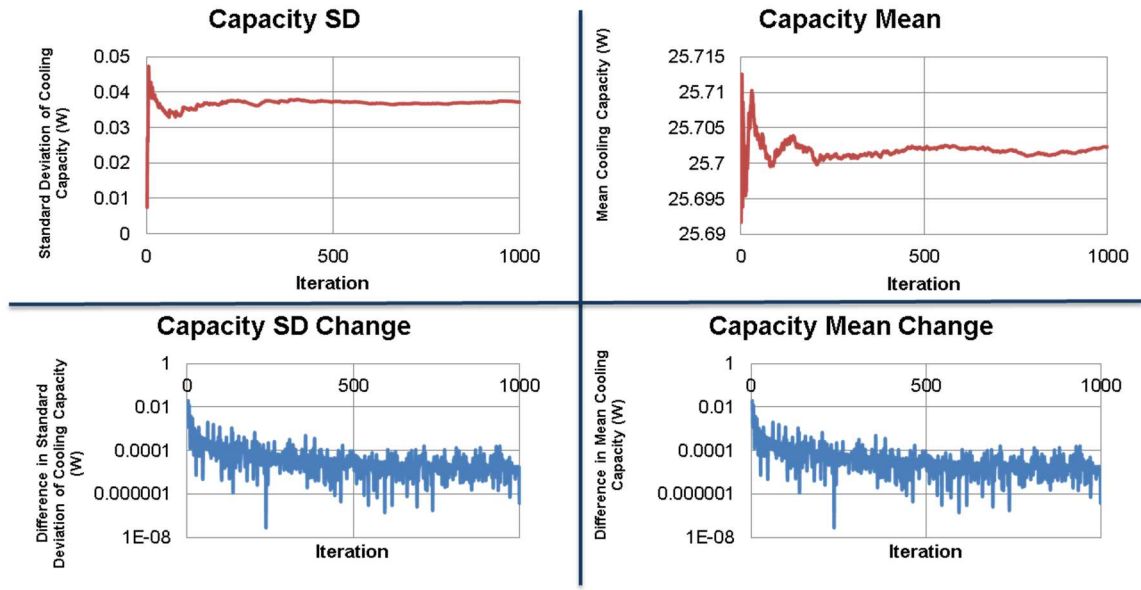
Figure 29: Convergence metrics versus iteration for an arbitrary simulation case. Top-left: Standard deviation of cooling capacity. Bottom-left: change per iteration of cooling capacity standard deviation. Top-right: cooling capacity mean. Bottom-right: change per iteration of cooling capacity mean.

Iteration to iteration change in cooling power standard deviation and mean represents less than 1% of the current value at 50 iterations, and less than 0.5% at 100 iterations. Efficiency, not shown, produces a similar trend. By another metric, after 100 iterations the current value for all parameters is with 1% of the final value (1000 iteration value). Convergence is considered complete at 50 iterations for simplicity. Considering planned statistical analysis of this generated data, less than 50 replicates per case can be used while still showing statistically significant results. A final check into the applicability of the above method is to confirm that the output is normally distributed, as shown in Figure 30.
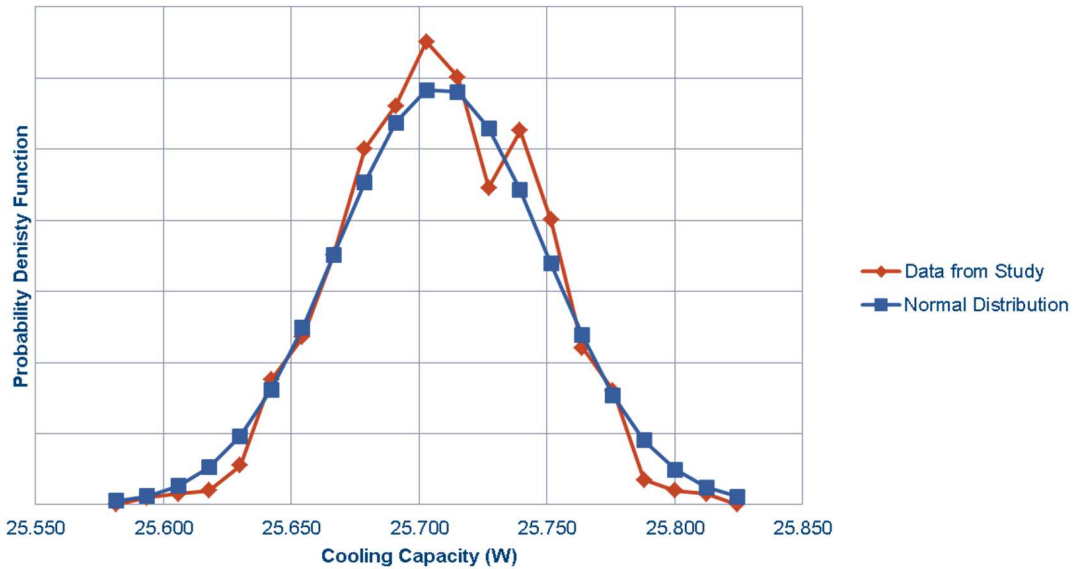
Figure 30: Histogram of 1000 iterations for cooling power and best fit normal distribution for cooling capacity of an arbitrary case.

As denoted in Figure 30, a histogram of 1000 points for output cooling power follow a normal distribution, meaning that mean and standard deviation appropriately describe output data. 1000 points are not necessary to characterize standard deviation and mean, as shown in Figure 29, although many points are needed to show the normality of the data in Figure 30. With many replicates, such as the case shown in Figure 30, P-value is approximately 1, meaning that the data is clearly aligned with the expected normal distribution probability density function, and can be considered to follow a normal distribution. As a last check, the average P-value for a Chi-Square goodness of fit test to a normal distribution is 0.27 for all simulated cases, having at least 10 replicates each, meaning that the null hypothesis of normally distributed data remains valid using a 0.05 alpha level. Figure 30 suggests that this value generally rises with addition replicates. A plot of ratio of Carnot COP data, not shown, again produces a similar result. Going forward, output distributions are assumed to be normal for analysis.

2.7 – Top Level Program Output

Output from the program includes high level information on each design point, such as mean, standard deviation, and sample count for cooling power and Carnot COP ratio, as seen in Table 1.

Parameter name in file	Description
ave Q cold (W)	Cooling power
ave Q hot (W)	Heating power
ave Q mag (W)	Magnetic power input
ave Q Visc (W)	Viscous power input
ave COP	Coefficient of performance
ave Carnot ratio	Ratio of Carnot COP
SD Q cold (W)	Cooling power
SD Q hot (W)	Heating power
SD Q mag (W)	Magnetic power input
SD Q Visc (W)	Viscous power input
SD COP	Coefficient of performance
SD Carnot ratio	Ratio of Carnot COP

Table 1: Parameters in high level output file, listed in Figure 28 as summary array.

High level output for an arbitrary performance curve shows the impact of relatively low levels of variation in material properties on cooling power, shown in Figure 31.
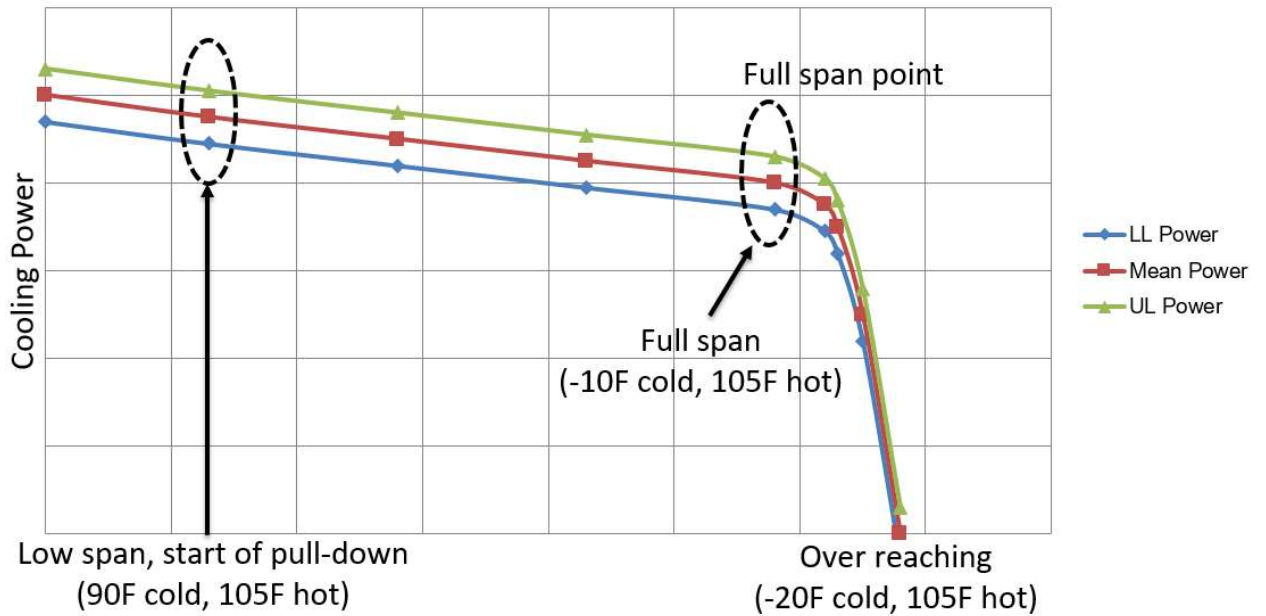
Figure 31: Output lower limit, mean, and upper limit cooling capacity as a function of span.

In Figure 31, 6-sigma lower limit indicates 6 standard deviations below average performance. For machine design purposes the lower limit of performance must be used as minimum acceptable condition. If zero variation were present for the performance curve in Figure 31 the real machine could be downsized to save cost without sacrificing statistical worst case performance.

The most critical portion of the performance curve in Figure 31 is capacity at full span, as this represents the design condition. Other sections of the curve are only utilized on off-design point operational states, such as during pull-down. Span is naturally limited by the cascade materials' Curie temperature range, and the overreaching point shows this rapid drop-off in cooling power. Because of this, a single span condition can be used for design guidance.

Detailed information for each iteration of each design point is also outputted into another file, such that any case can be recreated precisely. Low level details in the output file include all input parameters as well as the lists of randomly selected material properties for each stage of each cascade simulated. Low level data is mostly useful for debugging high level output, or determining the root cause of good or poor performance. Tabulated low level output parameters are given in

Iteration 0 to N
List of all input parameters
List of dT_A for each material
List of dT_W for each material
List of dT_T for each material
List of C_A for each material
List of C_W for each material
Q cold
Q hot
Q magnetic work
Q viscous heating
COP
Carnot Ratio

Table 2.

Iteration 0 to N
List of all input parameters
List of dT_A for each material
List of dT_W for each material
List of dT_T for each material
List of C_A for each material
List of C_W for each material
Q cold
Q hot
Q magnetic work
Q viscous heating
COP
Carnot Ratio

Table 2: Parameters in low level output file

Each column represents an iteration of the simulation on a particular design point. The design point gets an average output level for Q_cold for instance, by averaging the entire row across all iterations.

3 – ANALYSIS OF REAL MATERIAL

3.1 –Measurement Methods to Generate Material Data

Materials are typically measured using a differential scanning calorimeter (DSC) (Marcos et al., 2003) or physical property measurement system (PPMS) (Morrison et al., 2012). Measurements of interest include adiabatic temperature change on magnetization and zero-field heat capacity, both as functions of temperature. Assuming isentropic transitions, adiabatic temperature change on demagnetization and high-field heat capacity can be generated from the stated measurements of interest (Pecharsky et al., 2001). Other measurements of magnetocaloric effect are often made, but temperature change and heat capacity are directly used by the model for this study, and are therefore of primary interest for prediction of machine performance. Other information, such as entropy as a function of temperature, can be calculated from adiabatic temperature change and zero-field heat capacity, such that variation can be assessed using any translatable information.

When well calibrated, DSC and PPMS are in good agreement (Jeppesen et al., 2008), but poor calibration can lead to large errors (Morrison et al., 2012). Uncertainty levels for this measurement have been assessed at 1.5% for heat capacity and heat of fusion and 0.1 - 0.2 K for temperature change, all at 95% confidence (Nieto de Castro et al., 2000). Direct measurements of various magnetocaloric materials contain measurement uncertainty and real material variation. It will be assumed in this study

that measurement devices utilized were all well calibrated and data can be compared directly across different studies. These levels of measurement variation represent a minimum expected variation in directly measured magnetocaloric effect. Any additional variation will be considered real material variation.

3.2 – Origin and Analysis of Available Data

Various studies have presented measured data for first order magnetocaloric materials. Data was measured by Yibole et al. (2014) for MnFePSi. Benedict et al. (2016) published fitted values for 14 real materials, within the MnFePAs family of materials, from 280.9 – 310.9 Kelvin. Engelbrecht et al. (2013) also presented measured data for MnFePAs, although only as a single stage. Kaeswurm et al. (2016) and Katter et al. (2008) showed data for adiabatic temperature change for LaFeCoSi. Barcza et al. (2011) published a cascade of LaFeMnSiH composed of 5 materials. M.A. Benedict et al. (2016) published fitted values for 10 materials, also of the LaFeMnSiH family of materials.   Jacobs et al. (2014) presented heat capacity data for a six stage regenerator composed of LaFeSiH.

In order to study variation in material properties, large cascades are desirable. For large cascades, with many stages, trends between material parameters and Curie temperature can be easily accounted for. Because larger cascades are more ideal for analysis, data from Benedict et al. (2016a) and M.A. Benedict et al. (2016b) was utilized, and is hereto referred to as Benedict-LaFeSiH and Benedict-MnFePAs respectively. Along with this data, some newly presented data is included in the study. The new data is for LaFeSiH, will be referred to as Schroder-LaFeSiH-1 and Schroeder-LaFeSiH2, and can be found in the appendix. All four cascades were measured at 1.5 T. Shape of

material curves are quite similar between most first order material families (Basso et al., 2015; Engelbrecht et al., 2013), suggesting that other material families should behave similarly with regard to variation.

3.3 – Summary of Analyzed Data

In order to parameterize material data for variation assessment a split-Lorentzian function was fitted, as such a function very closely matches real data and provides useful fit parameters (Benedict et al., 2016, 2016). Curve parameters can at most include amplitude (A), width at half amplitude (W), skew (S), peak temperature (T), and Base. Although skew can provide a slightly better correlation to real data, it was excluded from this study. This decision was made because it simplifies the study and does not alter curve shape dramatically.

All of the material data represent lab-scale production, and aren't ideal for projecting mass production variation. However, the available data does represent a benchmark, from which improvements can be made.

Analysis Data								
Data set	Curve	Var	SS	SD	P	P < 0.05	Int	Slope
Benedict-MnFePAs (14 Stages)	MCE	A	0.18	0.118	0.234	NO	3.6	-0.021
		W	1.05	0.284	0.097	NO	6.6	0.150
		Tc	1.27	0.312	0.000	YES	295.6	-0.849
	Heat Capacity	A	Not Available					
		W	0.00	0.123	0.003	YES	6.1	-0.005
		Tc	1.10	0.657	0.000	YES	295.2	-0.924
		Base	Not Available					
Benedict-LaFeSiH (10 Stages)	MCE	A	0.65	0.590	0.088	NO	3.1	-0.029
		W	3.08	0.807	0.723	NO	6.7	0.024
		Tc	3.21	0.814	0.000	YES	313.2	-2.324
	Heat Capacity	A	257947	140.9	0.507	NO	1330.0	6.644
		W	3.67	0.532	0.333	NO	5.8	-0.074
		Tc	3.95	0.551	0.000	YES	312.7	-2.279
		Base	8229.5	25.2	0.012	YES	536.2	-5.136
Schroeder-LaFeSiH-1 (33 Stages)	MCE	A	0.66	0.144	0.000	YES	3.5	-0.027
		W	2.36	0.271	0.000	YES	7.8	0.113
		Tc	12.61	0.628	0.000	YES	311.4	-1.486
	Heat Capacity	A	Not Available					
		W						
		Tc						
		Base						
Schroeder-LaFeSiH-2 (56 Stages)	MCE	A	1.61	0.171	0.000	YES	4.6	-0.034
		W	18.04	0.573	0.000	YES	5.3	0.112
		Tc	6.80	0.352	0.000	YES	311.6	-1.006
	Heat Capacity	A	Not Available					
		W						
		Tc						
		Base						

Table 3: Regression output for four cascades, including MCE and heat capacity parameters.

Table 3 provides analysis of variance (ANOVA) linear regression data utilizing cascade stage number (cold to hot), and shows that some parameters have statistically significant trends while others do not. To generate Table 3, sum of squares (SS) for error is first calculated as,

$$SS_{error} = \Sigma_i(Y_i - \hat{Y}_i)^2 \qquad (24)$$

where $\hat{Y}_i$ is the prediction of the least squares linear regression equation at each

particular stage, and Y_i is the actual data point at the same stage. Sum of squares in

this case is the sum of error, or residuals, when comparing the regression equation to

the actual data. Sum of squares for the model is similarly calculated as

$$SS_{model} = \Sigma_i(\hat{Y}_i - \bar{Y})^2 \qquad (25)$$

where $\bar{Y}$ is the average of all predicted responses (all stages) using the linear model.

Standard deviation (SD), further is calculated as

$$SD = \left(\frac{SS}{n-1}\right)^{1/2} \qquad (26)$$

where n is number of observations and $n-1$ is degrees of freedom. Because there is

only one linear model for each independent output parameter (A, W, T_c, B), mean square

of each linear model is

$$MS_{model} = SS_{model}. \qquad (27)$$

Mean square error is

$$MS_{error} = \frac{SS_{error}}{n-1}, \qquad (28)$$

where n is number of stages for which there is data. P-value for an input parameter is

less than alpha, the null hypothesis is rejected, and the data or model is significantly

dependent on the input parameter in question. For these studies alpha is 0.05.

Regression intercept (Int) and slope define the best fit linear regression equation for

each parameter (A, 2W, etc.) as a function of cascade stage number. For instance, nominal amplitude (A) of stage 1 in Benedict-MnFePAs is

$$A = -0.021\,(1) + 3.3 = 3.279\,K. \tag{29}$$

Any given parameter can be multiplied by Curie temperature slope to translate units into slope per degree K from slope per stage. This is useful for direct comparisons independent of stage temperature spacing.

It is observable in Table 3 that significant trends in MCE amplitude and width are only found in Schroeder-LaFeSiH-1 and Schroeder-LaFeSiH-2. Being the longest cascades, Schroeder-LaFeSiH-1 and Schroeder-LaFeSiH-2 have the most potential to show subtle trends. Not surprisingly, Curie temperature is significant in all cases because it is varied to create these cascades. Figure 32 shows peak amplitude and half width at half max (HWHM) for Schroeder-LaFeSiH-1, which are both significant statistically in Table 3.
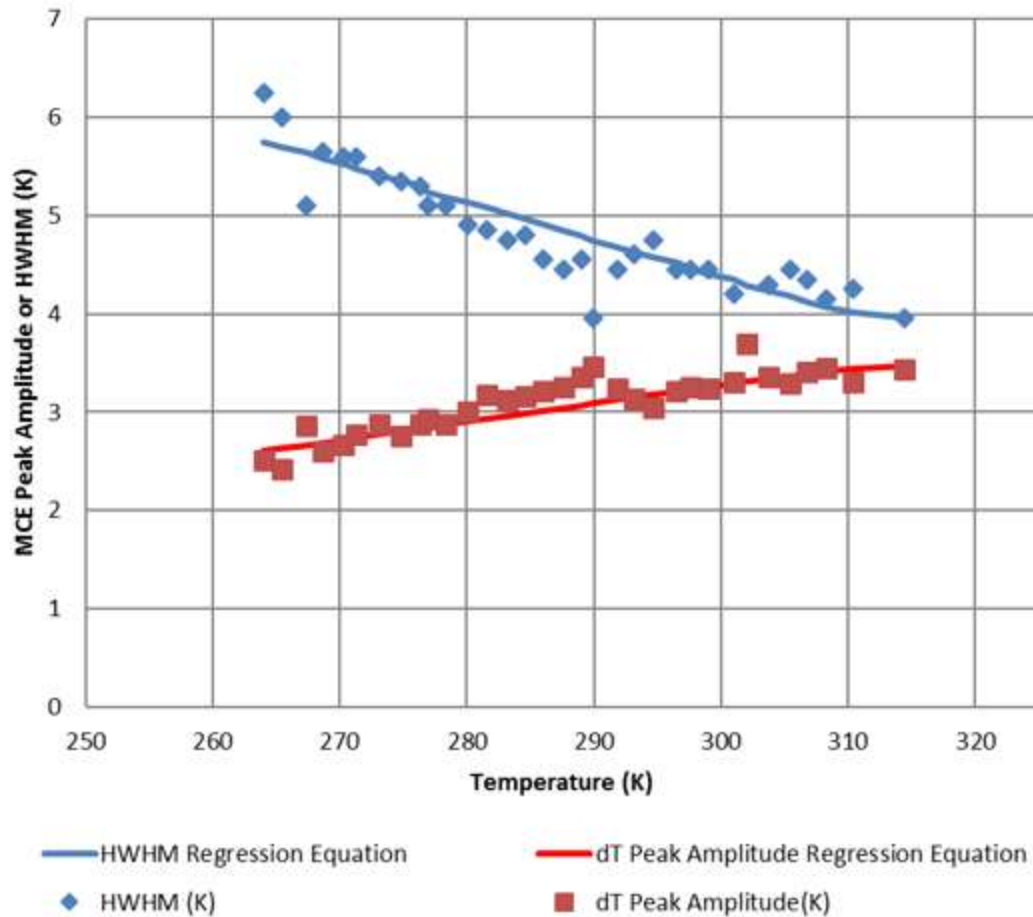
Figure 32: Schroeder-LaFeSiH-1 MCE peak amplitude and HWHM versus Curie temperature and regression equation output as a function of stage number.

It is observable in Figure 32 that trends may have a slight curvature, but linear regression provides a satisfactory fit for all cases. Adding additional terms would add complexity without dramatically improving correlation. Also note that the regression equations are not perfectly linear on the scale shown due to the least squares regression equation being based on stage number rather than temperature. This allows variation data to uniformly encompass peak height, width, and location using the same predictor, stage number. Figure 33 shows the same data for Schroeder-LaFeSiH-2.
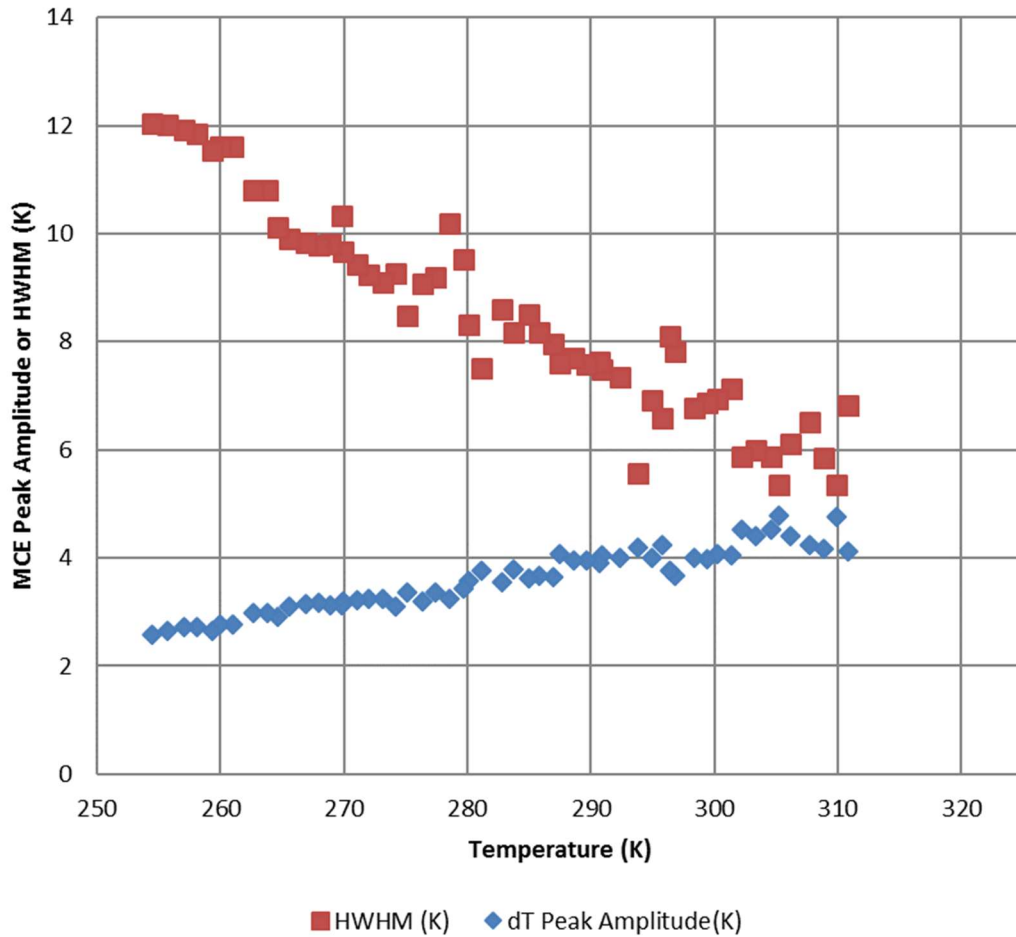
Figure 33: Schroeder-LaFeSiH-2 MCE peak amplitude and half width at half max versus temperature.

In this data set the data appears to be even more strongly linear than that shown in Figure 32. Very clear linear trends can be fitted, which are parameterized in Table 3. Also note that peaks are stronger in Schroeder-LaFeSiH-2 than in Schroeder-LaFeSiH-1, meaning that peak amplitudes are higher and peak widths are narrower, demonstrating qualitatively how changes in processing and batch can lead to major changes in curve shape. Table 4 provides a summary of standard deviation data from three cascades of FOPT materials. Standard deviation describes variation from the

linear regression lines described in Table 3, and is the metric used as input to the

regenerator performance simulation program in chapter 2.

Standard Deviations								
		MCE (K)			Heat Capacity (J/kgK)			
Data set	Stages	Tc	A	W	Tc	A	W	B
Benedict-MnFePAs	14	0.312	0.118	0.284	0.657	NA	0.123	NA
Benedict-LaFeSiH	10	0.814	0.590	0.807	0.551	141	0.532	25.2
Schroeder-LaFeSiH-1	33	0.628	0.144	0.271	Not Available			
Schroeder-LaFeSiH-2	56	0.352	0.171	0.286	Not Available			
Combined	113	0.845	0.494	0.677	0.615	141	0.356	25.2

Table 4: Standard deviation of fit parameters for Lorentzian function for three cascades.

Summarized and combined standard deviations are shown in Table 4, calculated

by combining variances for each set of observations (cascades).

$$S_{abc} = \left(\frac{(N_a S_a^2 + N_b S_b^2 + N_c S_c^2)}{N_a + N_b + N_c} \right)^{0.5}$$
(30)

S_{abc} is the combined standard deviation of arbitrary factors a, b, and c, N is sample

count for groups a, b, or c, and S is standard deviation for groups a, b, or c. These

measured cascades are used as the baseline variation level in the simulation study of

chapter 4. Average values for each parameter are shown in Table 5.

Averages								
		MCE (K)			Heat Capacity (J/kgK)			
						A	W	B
Data set	Stages	Tc	A	W	Tc			
Benedict-MnFePAs	14	289.644	3.496	3.830	288.766	NA	3.031	497.6
Benedict-LaFeSiH	10	296.932	2.933	3.427	296.747	1270.438	2.623	500.2
Schroeder-LaFeSiH-1	33	301.036	3.346	4.275	Not Available			
Schroeder-LaFeSiH-2	56	283.421	3.613	4.223	Not Available			

Table 5: Average material parameters from benchmark study.

Average amplitudes and widths are quite similar for these materials, and they represent a good sampling of available material data. As stated previously, peak amplitude tends to be higher at equivalent temperature in Schroeder-LaFeSiH-2 than in Schroeder-LaFeSiH-1 even though the base material is identical. Average Curie temperature represents the center of each cascade, which is similar for all datasets, representing a good sampling of materials for household refrigeration applications near room temperature. Analysis has also revealed that spacing between stages is currently about 1-1.5 K.

4 – PERFORMANCE AS A FUNCTION OF MATERIAL PROPERTY VARIATION

4.1 – Design Point Study

4.1.1 – Design Point Study Application

Household refrigeration is the application of interest for this study. For such an application it is common for the refrigeration system to operate near 105 F (313.7 K), which is held constant for this study. Designs can operate at higher or lower temperatures, but 105 F is assumed to be a reasonable temperature for most applications (Langebach et al., 2014). Cold side heat exchanger temperature is also held constant at -10 F (249.8 K), a typical application value as well (Langebach et al., 2014). 105 F and -10 F are therefore the rejection and absorption temperatures of the heat pumps evaluated in this study.

Heat exchangers reject and absorb heat at 90 F and 0 F respectively in this application, allowing for 10-15 F in temperature differential between heat transfer fluid and air. Improvements in heat exchanger technology reduce the operating span of a refrigerator, and provide efficiency benefits that can be calculated. Carnot COP,

$$COP_{Carnot} = \frac{T_{cold}}{T_{warm} - T_{cold}} \tag{31}$$

increases when span decreases. Heat exchanger performance is ignored in this study.

Heat leak and regenerator container interactions are also ignored. Motor efficiencies are

highly dependent on many factors outside the scope of this study, such as the loading

profile, number of poles, drive method, among others, and is considered to be 100%

efficient. Pump efficiency is similarly dependent on many outside factors, such as pump

type, frequency, backpressure profile, etc., and is similarly assumed to be 100% efficient

for this study. A specific assumed efficiency below 100% would be arbitrary without a

specific system design, which is the reasoning behind this assumption. However, a

hypothetical case with a non-perfect pump and motor is shown later in the present work

to show the relative impact on system efficiency, found in Chapter 6, Figure 68.

4.1.2 – Design Point Study Control Parameters

In order to assess the effect of material property variation on machine

performance, a range of design points were selected for simulation. Machine

parameters include applied magnetic field strength, fluid profile, channel diameter,

regenerator length, and void fraction. Fluid profile parameters are defined in Figure 22,

and include maximum fluid superficial velocity, ramp start time (magnetization time),

ramp elapsed time, and peak elapsed time. Void fraction is fluid volume contained in the

regenerator divided by total volume of the regenerator. Lei et al. (2015) showed that

tighter stage spacing results in a cascade slightly less sensitive to variation, and stage

count was included at 2 levels. Maximum stage spacing is set to 1.5 K per stage, the

measured average value in Chapter 3 on real cascades of materials. Minimum stage

spacing was set to 1.25 K per stage.

Center points are used for parameters with a relatively large change between low

and high levels due to the highly nonlinear nature of regenerator physics. For instance,

fluid velocity goes from a low level value of 0.01 m/s to a high level value of 0.05 m/s, an increase of 500%. In this case a center point is well justified. Lower and upper levels were set based on past experience, and are well aligned with the validated design space of the simulation tool.

Variables	Min	Max	Levels	Units
Magnetic field strength	1	1.5	2	tesla
Max fluid velocity	0.01	0.05	3	m/s
Magnetization time	0.05	0.5	3	s
Fluid ramp time	0.05	0.5	3	s
Fluid peak time	0.05	0.5	3	s
Channel diameter	0.1	0.5	3	mm
Regenerator length	0.05	0.15	3	m
Void Fraction	0.4	0.5	2	m
Stage spacing	1.25	1.5	2	K/stage

Table 6: Design of experiments matrix for design point study, having 9 main effects.

Table 6 shows ranges and levels simulated for the proposed design point study, which takes the form of a full factorial matrix with 5832 different cases. Analysis only assesses main effects and 2-way interactions, including interactions with curvature terms. For 9 main effects and 6 curvature terms, output parameter count is

$$N_{out} = 9 + 6 + (14 + 13 ... + 1) = 120 \qquad (32)$$

All 120 terms are included in the initial stages of analysis, to be reduced based on effect and significance. By neglecting to include higher level interactions, there effectively are multiple replicates for each output term for analysis. There are about 48 points for every parameter included in analysis, and every parameter is evenly distributed across all levels. For instance, there are 1944 points using 0.01 m/s fluid velocity, or 1/3 of the total points simulated. Higher level interactions in the background act to provide variability within the design space. Using a sparse method to fill the design space works

well for simulation based studies that are not based on random variation, because direct replicates of exact design parameter combinations result in identical output. When material variability is added in chapter 5 replicates can be used to generate variable output.

4.1.3 – Design Point Study Constants

All other simulation parameters remain constant for the design point study. Working fluid is 45% ethylene glycol, 55% water, which has a sufficiently low freezing point for the application minimum temperature. Fluid properties are summarized in Table 7.

Parameter	Value	Units
Thermal Conductivity	0.447	W/mK
Specific Heat Capacity	3357	J/kgK
Density	1063	kg/m^3
Viscosity at 275K	5.59E-03	$Pa\,s$
Viscosity at 300K	2.42E-03	$Pa\,s$
Viscosity at 325K	1.31E-03	$Pa\,s$

Table 7: Fluid properties for study, 45% ethylene glycol and 55% water mix.

Viscosity is treated as a polynomial, fitted through the three temperatures in Table 7. Thermal conductivity, specific heat capacity, and density are considered constant. Justifications are that these properties change by less than 10% across the regenerator temperature span, and have negligible impact on the material property variation study. Round straight microchannel geometry is assumed for regenerator structure. When cascade span is exceeded by application span performance logically suffers. Ends of the regenerator would be operating away from their respective Curie temperatures, where the maximum transition energy is available. To avoid this condition regardless of cycle parameters magnetocaloric material cascade Curie temperatures

span from 112 F (317.5 K) to -17 F (246 K), providing 7 F on both regenerator ends as a buffer.

4.1.4 –Design Point Study Output

Output from the design study includes cooling power per regenerator volume,

$$\boldsymbol{Cooling\ power\ density} = \frac{\dot{E}_{cooling}}{A_{regen}L_{regen}}$$

(33)

where $\dot{E}_{cooling}$ is cooling power, A_{regen} is regenerator cross sectional area, and L_{regen} is regenerator length. Cooling power density is used rather than cooling power to make the output more broadly useful. If a particular regenerator generates a very low cooling power but is very small in size it can be scaled up directly via cross sectional area in order to generate a larger cooling power. This hypothetical regenerator design may still be a good design point and should not be viewed as a bad design option. This also allows output to be less strongly tied to the specific application. A good design can be scaled to work well for large and small refrigerators directly.

Carnot ratio is the second primary output parameter,

$$\boldsymbol{R_{Carnot}} = \frac{COP}{COP_{Carnot}}.$$

(34)

COP, or coefficient of performance, is defined as

$$\boldsymbol{COP} = \frac{\dot{E}_{cooling}}{\dot{E}_{rejected} - \dot{E}_{cooling}}$$

(35)

Ratio of simulated COP to Carnot COP is implied when the word efficiency is used within this study. Carnot ratio is another metric that is more useful than non-normalized terms such as COP. Carnot ratio can be compared across different applications with different

temperature spans, and in this way is the most useful metric for comparing different technologies as well. In the case of this type of simulation, largely negative cooling power results from exceptionally poor combinations of input parameters. Numerically, when this happens the model becomes divergent and must exit prematurely. For analysis these cases would skew the statistics if left as-is, but to remove them entirely would inversely skew the statistical model. Essentially a negative impact must still be observed in these poor cases, but the magnitude of that impact must be clipped. It was deemed reasonable to limit highly negative cases by the maximum positive value observed on the best case, such that the best positive cases enact an equivalent positive impact to the worst case's negative impact. For Carnot ratio the same method is employed, limiting negative Carnot ratio to the inverse of maximum observed Carnot ratio in the best case.

For analysis, a general linear model was utilized. There are two outputs and many inputs, including 9 main effects, 6 curvature terms, and 105 2-way order interactions. This yields a total of 120 terms within the study. Total variance,

$$SS_{total} = \sum_i \sum_j \sum_k (Y_{ijk} - \bar{Y}_{***})^2 \tag{36}$$

is partitioned and different sources of variance are compared to attain P-values. Here, i,j, and k represent arbitrary input parameter sets, such that every input parameter combination is summed. Again, there are actually 120 input parameters for this analysis. $\bar{Y}_{***}$ signifies the average output of all input combinations, and Y_{ijk} represents output from each individual input parameter combination. Variance induced by each of the 84 input parameters is found by

$$SS_i = \sum_i n_i (\bar{Y}_{i**} - \bar{Y}_{***})^2, \tag{37}$$

63

where $\bar{Y}_{i**}$ is the average output from each level of parameter i, and n_i is sample count within each level i. Variation from interactions follows a similar form,

$$SS_{ij} = \sum_i n_{ij}(\bar{Y}_{ij*} - \bar{Y}_{***})^2 - SS_i - SS_j,$$

(38)

Finally, unaccounted for variability is the difference,

$$SS_{error} = SS_{total} - SS_i - SS_j - SS_k$$

(39)

Mean square is next calculated using sum of squares for each factor, which for factor i is

$$MS_i = \frac{SS_i}{a-1},$$

(40)

where a is the number of levels for factor i, and $a - 1$ is the degrees of freedom for factor i. Mean square error for factor i is

$$MS_{error} = \frac{SS_{error}}{N - \sum(df \; all \; sig. \; cases)},$$

(41)

where N is the total number of input cases. Mean squares are used to find the ratio used for an F test, which for factor i is

$$F_0 = \frac{MS_i}{MS_{error}}$$

(42)

P-value is the probability of obtaining each F_0 or larger if the null hypothesis is true. In other words, if P-value for an input parameter is less than alpha, the null hypothesis is rejected, and the data is significantly dependent on the input parameter in question. An alpha value of 0.05 is assumed for the presented study. Insignificant effects and interactions ($P > 0.05$) in both Carnot ratio and cooling power density outputs are omitted from further analysis. The zero variation study output covers a wide range of design options, as is indicated by the points cloud in Figure 34.
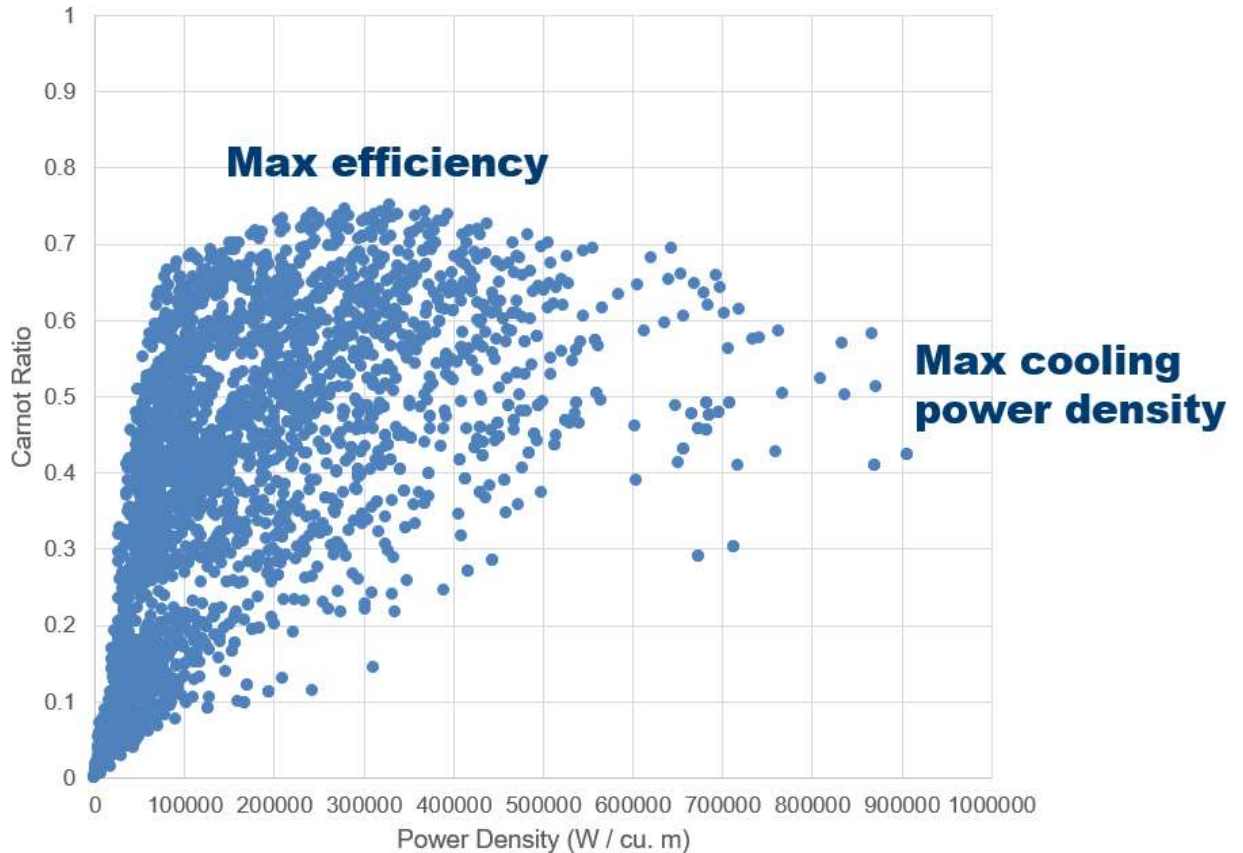
Figure 34: Points cloud, showing power density and Carnot ratio for the design point, or zero variation, study. Only positive cooling power cases are shown.

Maximum efficiency observed is about 75% of Carnot COP. It would be expected that maximum efficiency could not be achieved at maximum power density, which is also observable in Figure 34. Figure 34 shows an excellent points spread, suggesting that it is representative of a general design space, although additional levels of input parameters would be expected to expand it somewhat farther in all directions. The addition of material variation terms, coming in chapter 5 would also be expected to more completely fill in this points cloud. Designs with negative cooling power are omitted from the graph, but are included in the analysis. Short-hand for parameter names are shown in Table 8.

Short-hand	Definition
dT_A	Standard deviation of peak amplitude for magnetocaloric effect
dT_W	Standard deviation of peak width for magnetocaloric effect
dT_T	Standard deviation of peak location for magnetocaloric effect
C_A	Standard deviation of amplitude for magnetocaloric heat capacity
C_W	Standard deviation of peak width for magnetocaloric heat capacity
S	Number of stages, indirectly sets stage spacing
M	Magnetic field strength
V	Peak velocity
t_f	Peak flow time for velocity profile
t_r	Ramp time for velocity profile
t_m	Magnetization time or dwell time for velocity profile
D	Channel diameter
L	Regenerator length
VF	Void fraction

Table 8: Short-hand for parameter names in analysis.

Material variation terms are included in the first 5 rows of Table 8, although they are not yet utilized until chapter 5. Names are shortened to make results more readable. For interaction terms "&" is placed between interacting terms, and "**2" indicates that it is a curvature term. Curvature terms are squared in coded units, which allows the center point to be differentiated from end points.

In order to compare effects on cooling power density and Carnot ratio side-by-side, normalized parameter effects are calculated. For arbitrary factor i, normalized effect is defined as

$$\tau_i = \overline{Y}_{i**_1} - \overline{Y}_{i**_{-1}},$$

(43)

where $\bar{Y}_{i**_1}$ is the average of all output data with high level of factor i and $\bar{Y}_{i**_{-1}}$ is the average of all output data with low level of factor i. Furthermore, normalized effect is defined as

$$\tau_{i\_norm} = \frac{\tau_i}{\tau_{max}}$$
(44)

where τ_{max} is the largest effect shown by any combination of input parameters.

Normalized parametric output for the zero variation study is shown in Figure 35, with only the top 50 effects shown out of 120 total analyzed output terms.
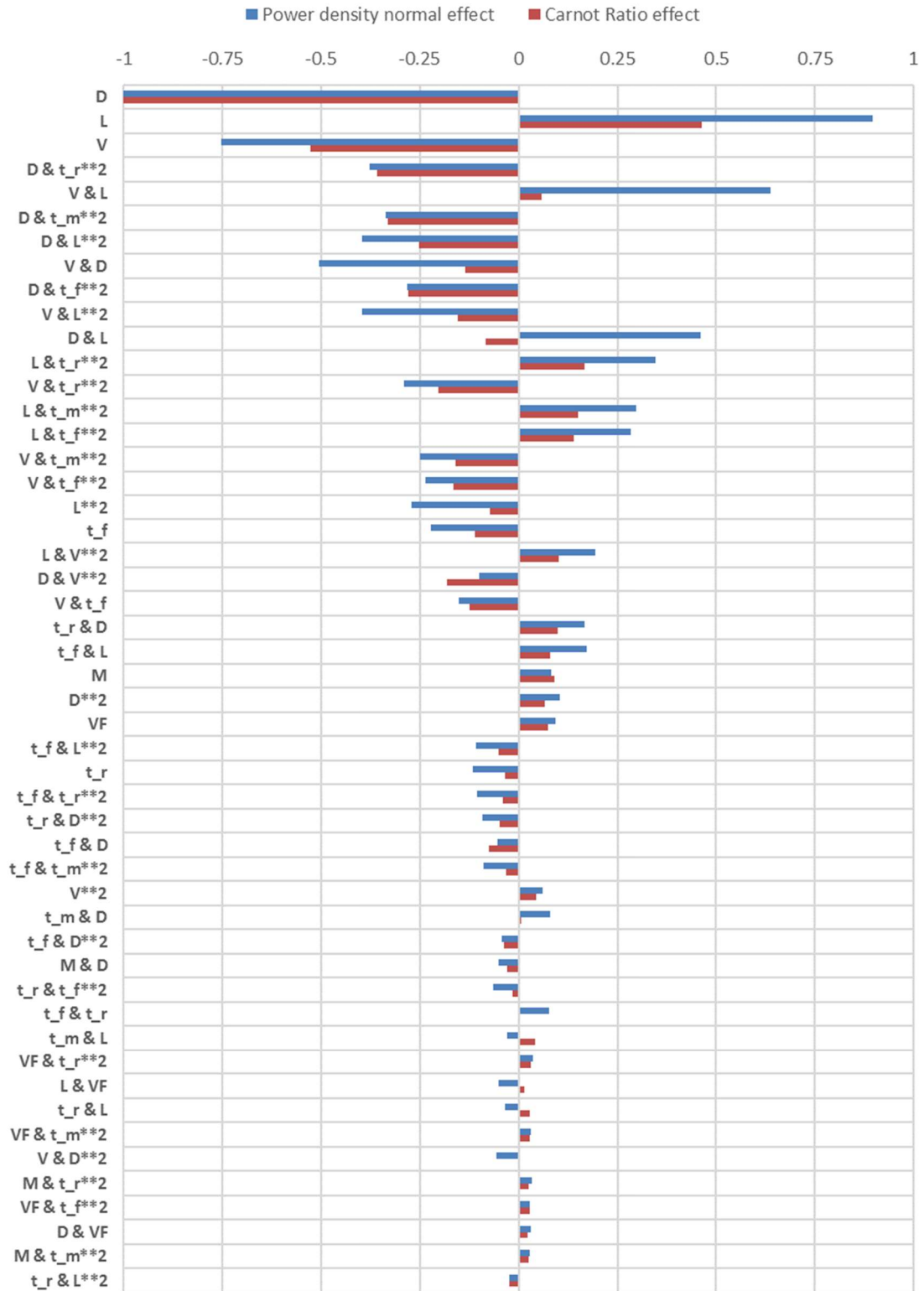
Figure 35: Main effects and interactions as fractions of maximum output of all cases for cooling power density and Carnot Ratio

In Figure 35, parameters are ranked in descending order by the sum of effects of Carnot ratio and normalized cooling power density. Effect has both magnitude and direction, either negative or positive. Direction shows whether the output parameter, Carnot ratio or normalized cooling power density, is negatively or positively impacted by a positive change in the input parameter. For example, higher length values (L) are associated with an increased Carnot ratio and cooling power density. Larger channel diameter (D) is associated with lower Carnot ratio and cooling power density. These are both expected due to the physics of the system. The direction of all effects are summarized in Figure 36.
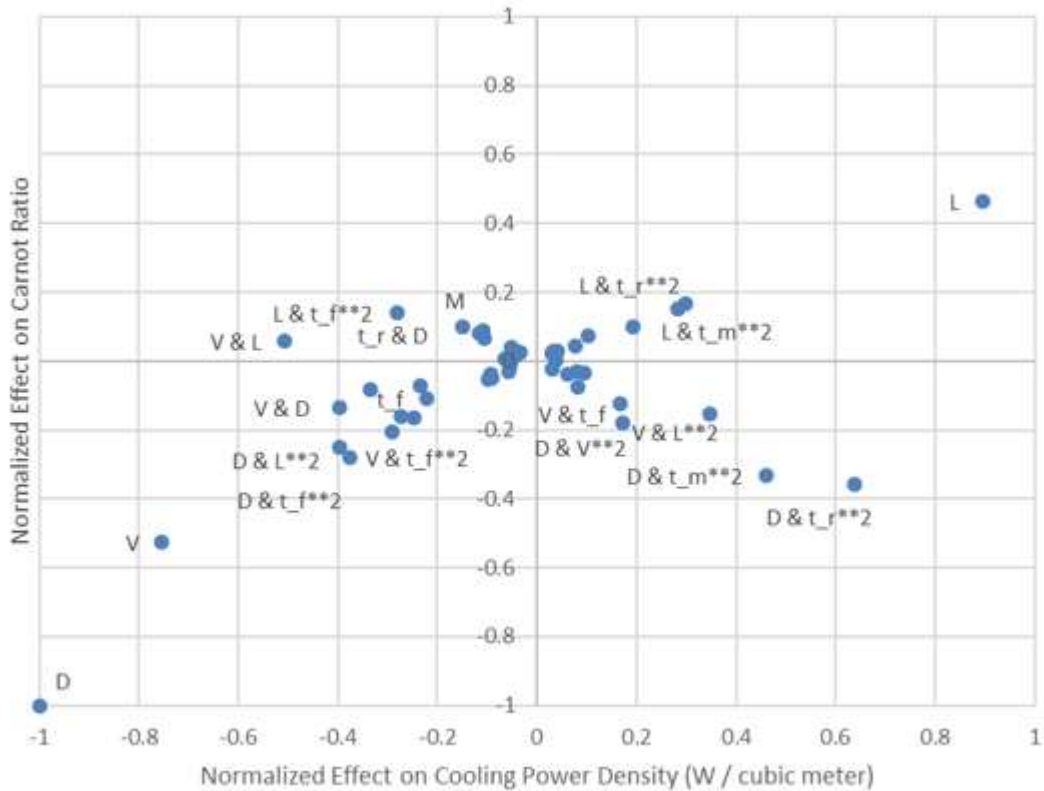
Figure 36: Scatter plot of effect magnitudes for Carnot ratio and normalized cooling power density in the zero variation study.

Labels have been omitted near the origin on the graph for readability. Generally, effects that fall within the upper right or lower left quadrants are the most straightforward to consider in the design process. Effects in these 2 zones affect both efficiency and cooling power in the same direction. For example, smaller channel diameters produce higher efficiency and higher cooling power density. Low velocity leads to higher efficiency and cooling power density within this study. Effects in the upper left and lower right quadrants of Figure 36 require a more delicate balance. Another interesting outcome is that an "X" is readily observed when viewing effects in this format, suggesting that parameters affecting performance generally impact both efficiency and cooling power density simultaneously. This also indicates that some parameters affect efficiency and cooling power density inversely, while others effect efficiency and cooling power density in the same direction. Very few terms have a large effect on one output without having an effect on the other. Further analysis of various effects in the zero variation study follow, categorized by main effects, interactions, and curvature.

4.1.3.1 – Main Effects in Design Point Study

In Figure 35, channel diameter, length, and fluid velocity have the largest effects, and represent the most critical design parameters. Lower in magnitude, again in descending order, are flow time, magnetic field strength, void fraction, and flow ramp time. It is observable in Figure 35 and Figure 36 that channel diameter shows the largest impact on both efficiency and power density. This is visualized in Figure 37.
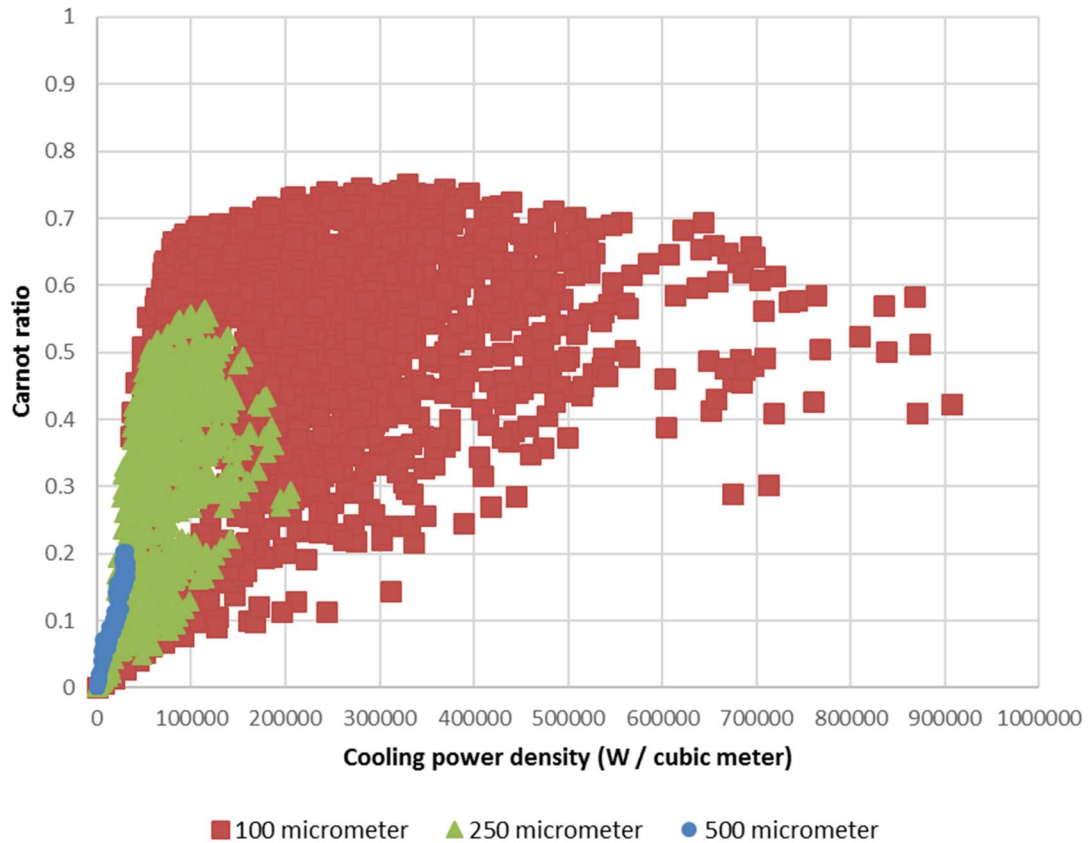
Figure 37: Carnot ratio versus cooling power density, broken up by channel diameter.

Very small fluid channels provide vastly different performance as compared with larger channels. Large fluid diameter channels lead to lower power density and lower efficiency, most likely due to the drop in heat transfer area and increase in Peclet number and dispersive losses. Smaller channels are much more numerous in order to maintain the specified void fraction, which in turn leads to high heat transfer area per unit volume. Regenerator length also shows a large effect on both COP and cooling power, both of which are positive. However, the effect is much smaller than channel diameter, as is shown in Figure 38.
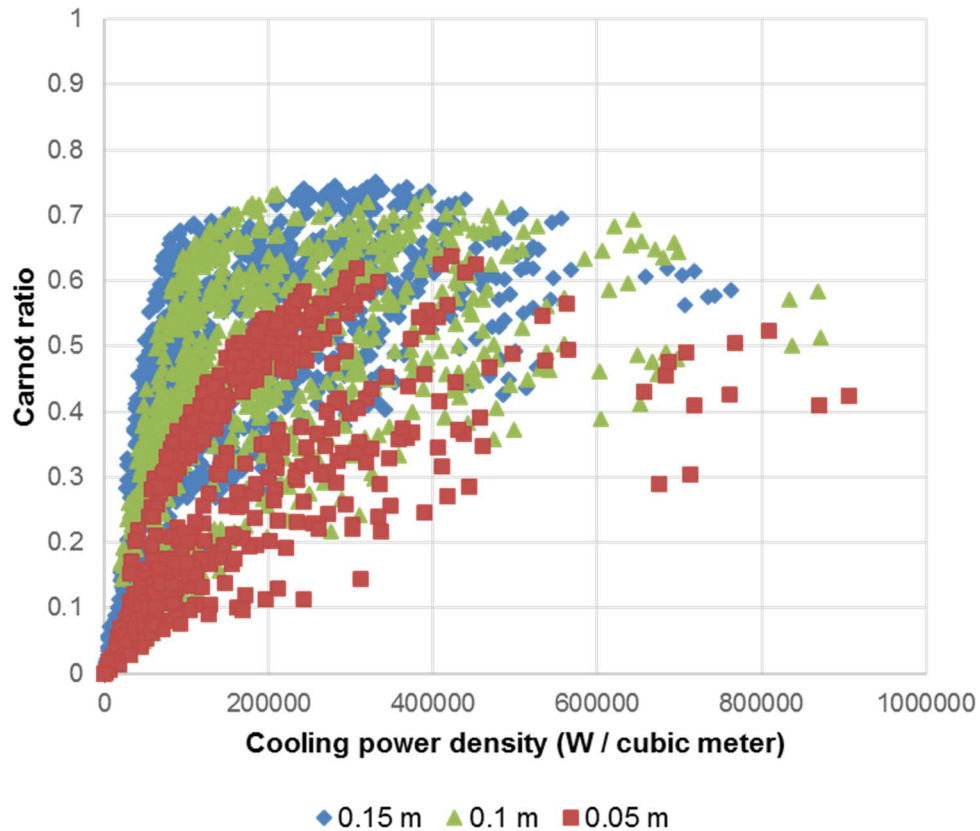
Figure 38: Carnot ratio versus cooling power density, broken up by regenerator length.

Comparing Figure 37 and Figure 38, it is observable that regenerator length has a much smaller effect than channel diameter, even though length is still a significant effect. Fundamentally, the effect of length is explainable by looking at the driving differential equations relating to dispersion and mass transfer in section 2.4.1. Useful movement of energy is performed via bulk fluid motion, which is linearly related to regenerator length. Energy transfer during bulk motion portions of the cycle is reduced via dispersion, which is quadratically related to length. Above a certain length dispersive losses are far outweighed by mass transfer. A simpler perspective for this is that the hot and cold ends of the regenerator are farther separated, which reduces heat transfer from hot to cold, in the opposite direction to heat pumping action.

The next largest effect following length is fluid velocity, which shows a negative effect on both output parameters over the range tested in the study. Higher velocities increase dispersive and viscous losses in the channels, which hurt efficiency and cooling power density in this case as well. To an extent, a higher fluid velocity can increase mass transfer at a faster rate than associated losses for smaller design ranges, but for the present work this is not the case.

Flow time directly effects cycle frequency, and therefore negatively affects efficiency and cooling power density. An ideal system with a small flow time would generally have a lower fluid displacement per cycle than a system with a large flow time. Very small amounts of fluid are difficult to extract efficiently in practice, and such a system would rely on a very low dead volume. Some amount of dead volume, or expansion space is always necessary on the regenerator ends to transition between hydraulic lines and the regenerator. When the total displaced fluid volume per cycle is similar to dead volume, the actual performance will not match a simulation study well.

Other main effects such as magnetic field strength also have logical explanations for their respective effects. Magnetic field strength shows a positive effect for Carnot ratio and a slightly negative effect on cooling power density. This outcome is partially in conflict with Benedict et al. (2017b) and Benedict et al. (2017a), which showed a positive impact on cooling power density for a specific design range. This would be expected to shift as material variation is introduced, where a larger magnetic fields allow gaps between stages to be less detrimental to performance. Magnetocaloric materials typically increase in effect (adiabatic temperature change) with magnetic field strength. In addition, peak width increases with field strength, which improves cases with large stage spacing and larger material variability the most.

Much smaller, but still significant, are ramp time, void fraction, and magnetization time. Ramp time negatively affects efficiency and positively affects cooling power density. This suggests that an ideal fluid flow velocity profile for efficiency may be nearly square, with minimal time for transition between levels. Magnetization time should also be minimized as much as possible, but again there are practical limits on how quickly a magnetic field can be applied and withdrawn within a physical system with moving parts. Finally, void fraction shows positive effects, suggesting that sparser structures with less MCM allow for easier transferring of energy within the range of the present work.

4.1.3.2 – Interactions in Design Point Study

Most effects fall into the category of interactions. Looking at the number of interactions containing each input term is suggestive to the term's importance in the design process.
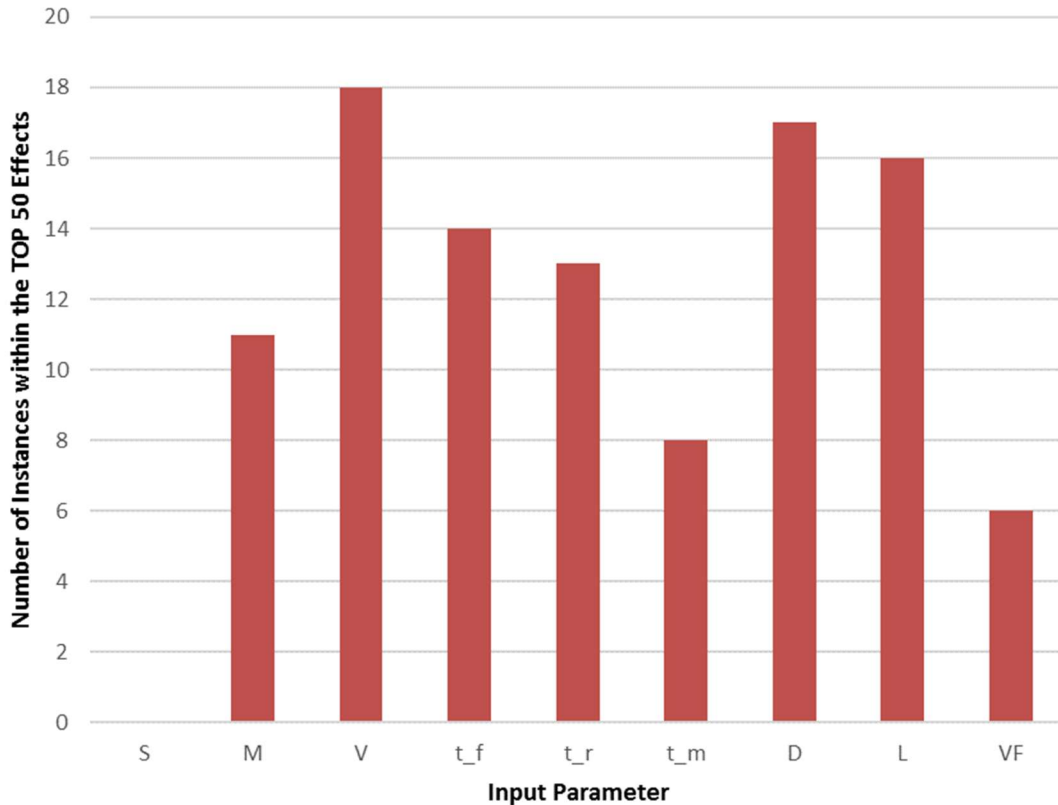
Figure 39: Occurrence counts for all input parameters found in interaction terms within the top 50 effects, measured by magnitude.

In descending order in Figure 39: Velocity (V), diameter (D), length (L), flow time (t_f), ramp time (t_r), magnetic field (M), magnetization time (t_m), void fraction (VF), and stage spacing (S). Stage spacing (S) does not fall within the top 50 terms, although it is still significant statistically. This sequence of prevalence closely matches the order of main effects found in Figure 35. Diameter and ramp time curvature interact most strongly, although relevance of the interaction is somewhat difficult to determine, as is shown in Figure 40.
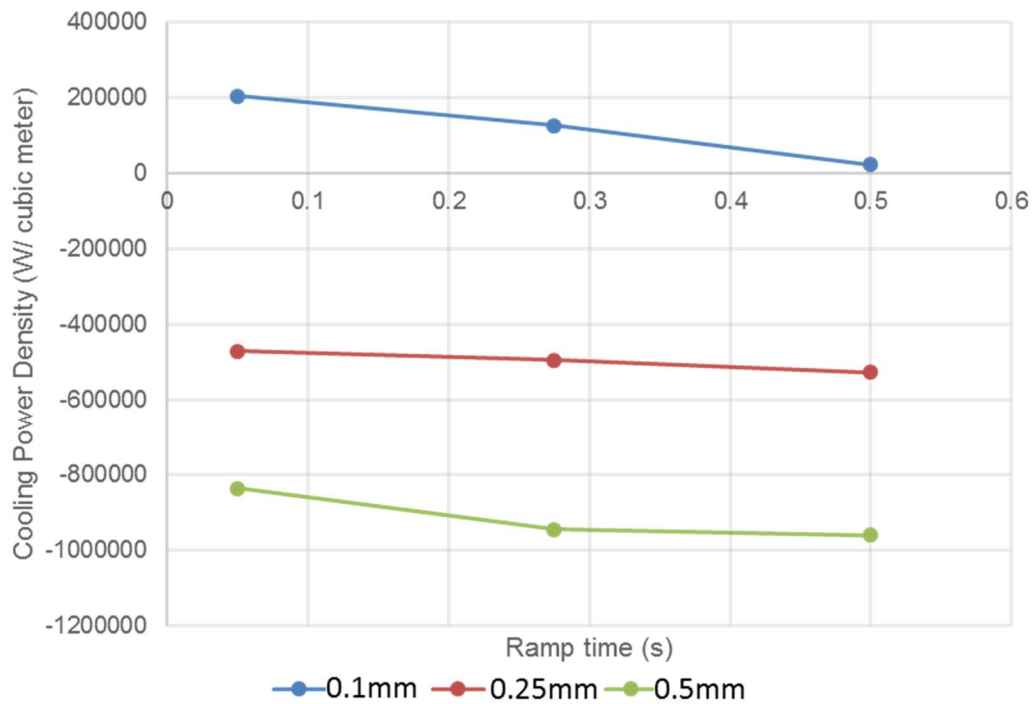
Figure 40: Cooling power density as a function of ramp time and channel diameter.

Figure 40 shows average cooling power density as a function of ramp time and channel diameter. Although the interaction is significant, many of the points for the 0.00025 m and 0.0005 m channel diameters have negative cooling power based on Figure 40, leading to negative average cooling power densities. This is the case for every interaction between diameter and other parameters. These cases with negative cooling power do not break physical laws, but simply do not provide a useful capability for cooling.

In contrast, velocity and length interact strongly in a meaningful way, where higher velocities should be paired with longer regenerators for optimal performance. Essentially, velocity and length should be scaled up or down together while designing a regenerator. In a similar way velocity interacts with diameter, suggesting that higher

velocities should be paired with larger diameters. In this case viscous heat generation

and losses due to fluid flow need to be balanced by matching high velocities with large

channels. Many other interactions are highly relevant in Figure 35, but as shown in

these several examples, interactions are quite complex overall.

4.1.3.3 – Curvature in Design Point Study

Curvature terms' occurrence counts are shown in Figure 41.
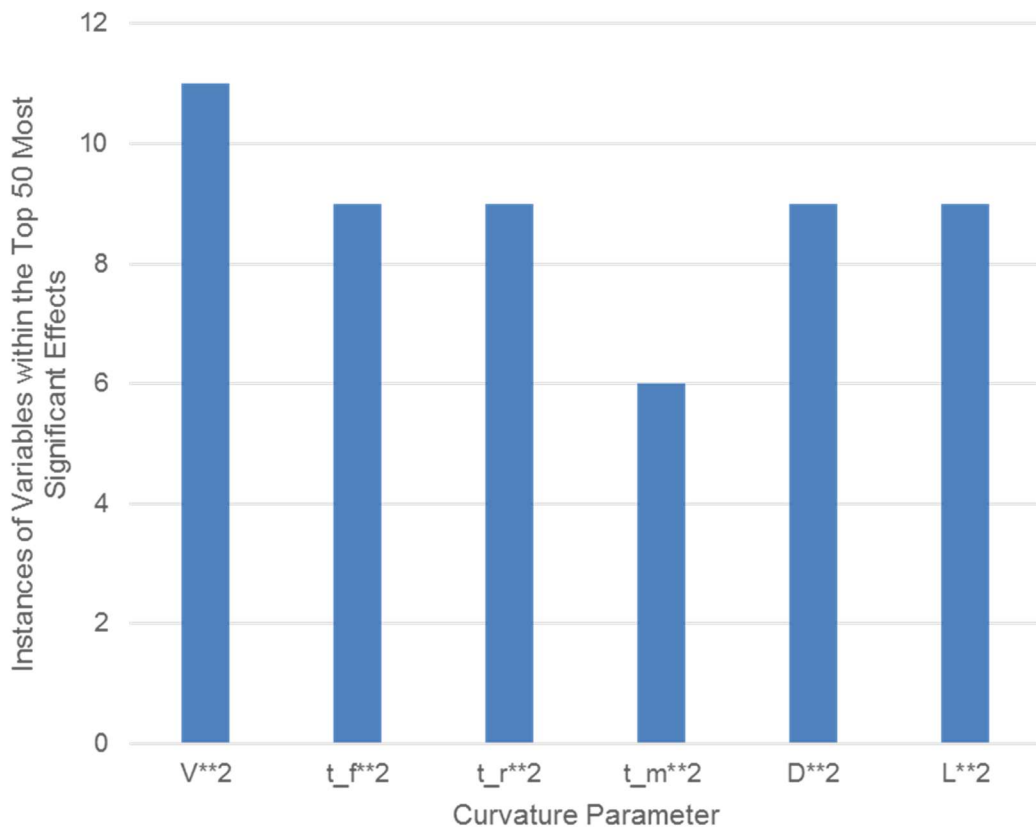
Figure 41: Occurrences of curvature terms in the top 50 effects for the zero variation study.

Relative levels in Figure 41 closely follow those observed in Figure 39 for main

effects. All terms show significant curvature, and again illustrate the complexity of such

a heat pump design. Velocity curvature appears most often in the top 50 terms, but flow

time, ramp time, magnetization time, diameter, and length all appear in at least 6 of the top 50 terms.

Curvature is most significant with length (L). Next is diameter (D**2), followed by velocity (V). Causes of curvature can be taken from nonlinear physical relationships being simulated. Heat transfer between MCM and heat transfer fluid,

$$UA_{MCM-f} = \frac{6(1-\varepsilon)}{\left[D^2\left(\frac{1}{3.66 k_f}+\frac{1}{6\,k_{MCM}}\right)\right]}$$
(**17**)

provides one such example. Heat transfer between MCM is the primary means for harvesting the magnetocaloric effect, and is therefore a significant contributor to overall system performance. Another nonlinear effect is axial dispersion,

$$k_{eff} = k_f\left(1+\frac{Re^2\,Pr^2}{192}\right)$$
(**18**)

Axial dispersion is an indirect loss mechanism for oscillating flow systems, conducting heat between the hot and cold reservoirs through the regenerator solid-fluid matrix. Both are strongly tied to length, velocity, and diameter.

4.1.3.4 – Summary of Design Point Study Findings

Because only cases with positive cooling power were analyzed, this study identified what variables are most critical to control for a given successful design. All parameters produce a statistically significant effect on Carnot ratio and cooling power density, but channel diameter, length, and fluid velocity must be most closely controlled.

Even with such a complicated system there are excellent optimization schemes to be implemented which are capable of finding optima as directed. Where research is lacking is not in simple predictions of performance, but in determining performance with

realistic material property variation. At a high level this data represents a baseline, to which magnetocaloric property variation can be added, shown in section 4.2 for comparison.

4.2 – Material Property Variation Study

For this portion of the study it is of greatest interest to know the impact of magnetocaloric material property variation on good designs. Cases with positive cooling power from the design point study represent zero property variation, or the lowest level of variation. It is most important to know the effect of material variation on designs that actually produce cooling power, which is the reason for ignoring cases with negative cooling power, which do not actually work in a practical sense. About 25% of the zero variation points yielded positive cooling power, or 1485 of the 5832 points. Two additional levels of material variation were simulated at these design points, utilizing center points to assess curvature in material variation parameters.

		dT_A (K)	dT_W (K)	dT_T (K)	C_A (J/kgK)	C_W (K)
Levels	1	0.494	0.677	0.845	141	0.356
	0	0.247	0.339	0.423	70	0.178
	-1	0	0	0	0	0

Table 9: Levels for each standard deviation of material property parameters.

Maximum variation levels (coded unit, level 1) are based on the analysis of real material variation in Chapter 3. Standard deviation values being provided to the simulation tool are summarized in Table 9. The center point (coded unit, level 0) is 50% of the maximum variation value for each variation parameter in Table 9. Zero is the lowest level for each parameter (coded unit, level -1).

For this portion of the study replicates were not directly used, and 100,000 combinations were simulated. For each design of interest, a random designation for each material property variation parameter was assigned, -1, 0, or 1. By allowing the five material property variation parameters to vary relative to each other, interactions can be assessed. If these 5 additional parameters describing material variability were varied in every possible combination, 360,855 designs would have to be simulated for a single replicate. Due to the computational limitations this was limited to 100,000 simulations. Using the same principle applied in section 4.1 to generate replicates by ignoring higher level interactions, this allows main effects and 2-way interactions to be assessed using a limited dataset. For 13 main effects, 11 curvature effects, and 276 2-way interactions, a total of 300 effects are used in the analysis. For 100,000 points in the output dataset, there are about 333 output cases per analyzed term. Input parameters are evenly distributed across all levels, providing approximately 333 replicates per analyzed effect. Results qualitatively fall within a similar performance envelope, as is shown in Figure 42.
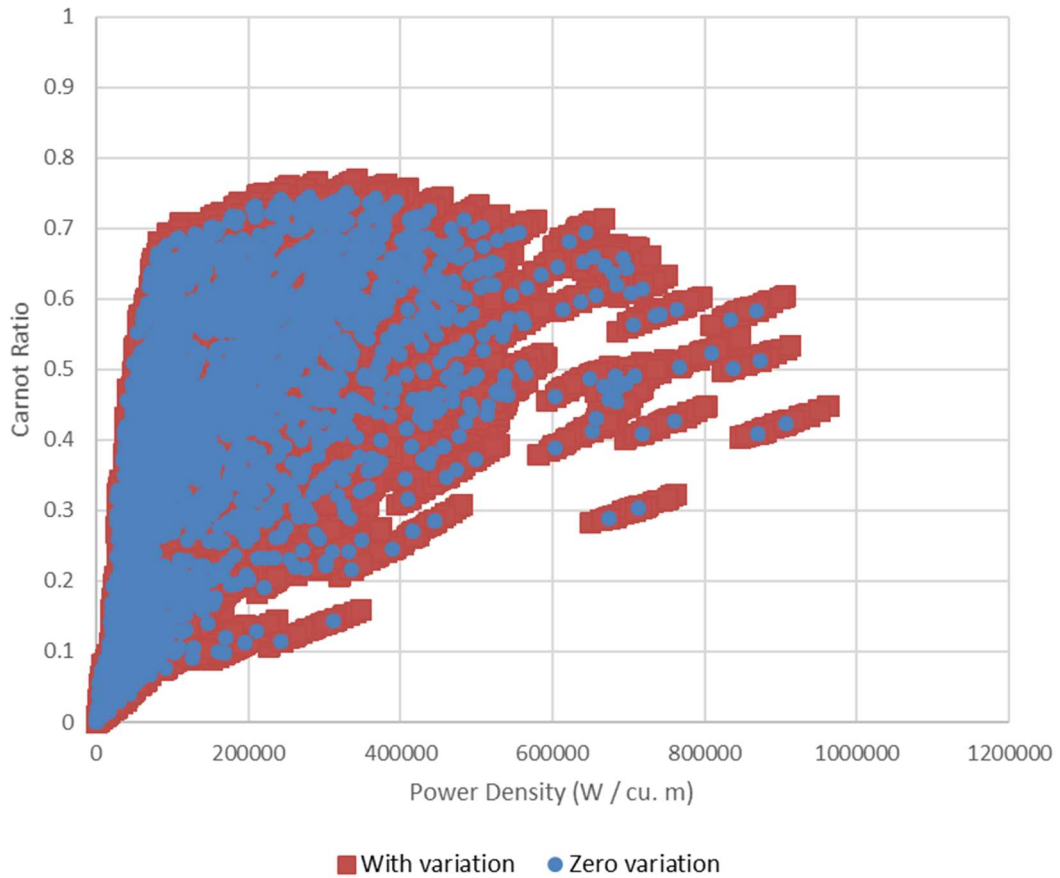
Figure 42: Power density versus Carnot COP ratio for all points having high or low variation levels (1 or -1 in coded units).

Figure 42 shows the cloud of points simulated for both portions of the presented study, which all qualitatively appear to be part of the same dataset. Maximum efficiency is slightly higher, at about 78% of Carnot COP, and maximum cooling power density is similarly slightly higher. This matches well with observations by Lei et al. (2015), where some cascades showed modest gains in performance due to randomness of material properties. Although average performance suffers with variation, a few cases outperform zero variation case. Looking deeper, difference can be observed in the effect of individual parameters on performance.

4.2.1 – Average Cooling Power Density and COP

Figure 43 shows primary effects, curvature terms, and 2-way interactions that are directly comparable to the design point study in section 4.1, corresponding to average performance predictions. This is simply a direct analysis of the points cloud using ANOVA.
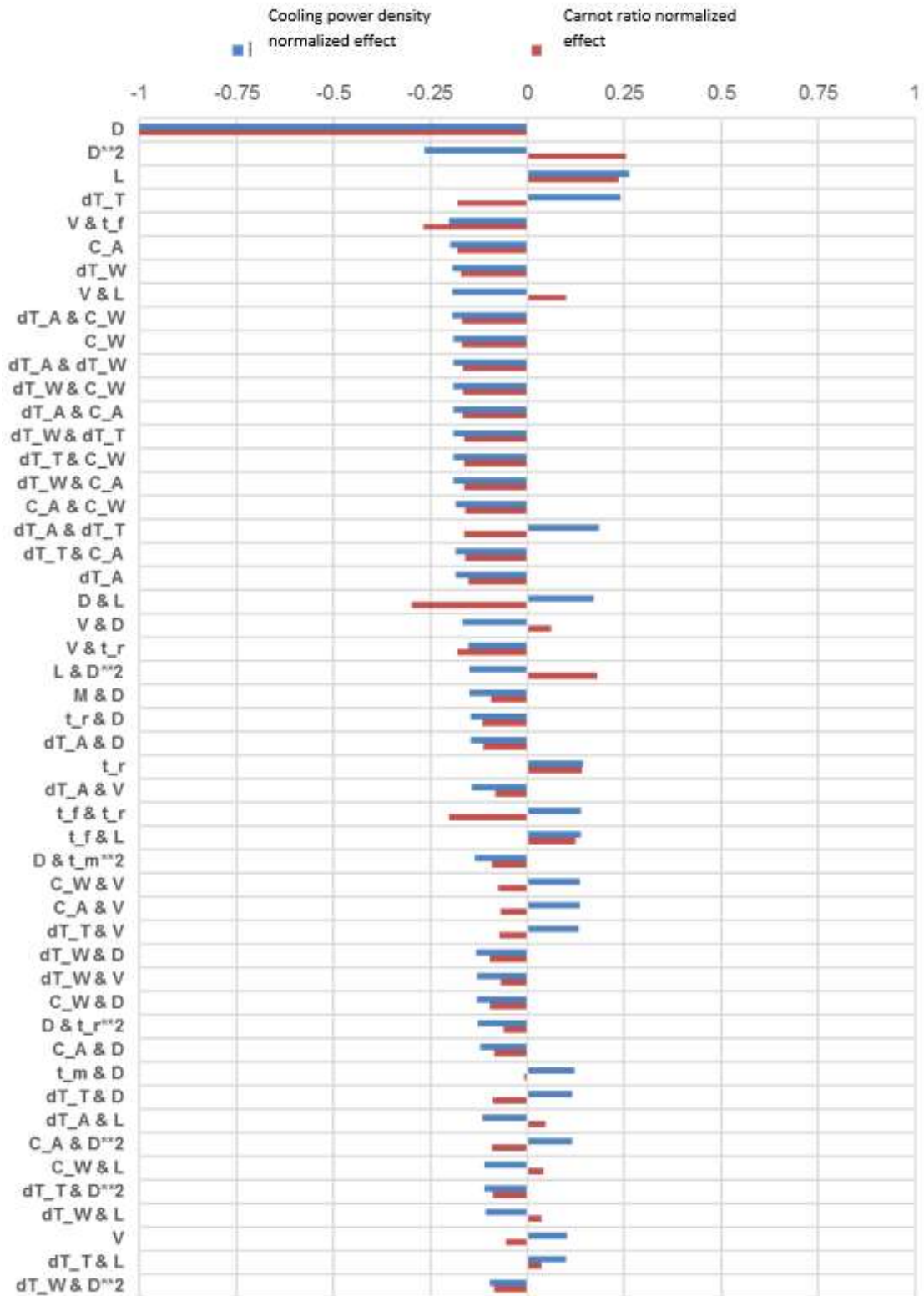
Figure 43: Main effects and interactions as fractions of maximum output of all cases for average cooling power density and average COP with material property variability.

Within Figure 43 it is observed that the largest effect on average COP and cooling power density is channel diameter (D), closely followed by length, which is similar to the zero variation study. However, this is where the similarities end. Of the top 50 significant terms shown, nearly every interaction involves material variation parameters. Figure 44 shows the number of instances of each primary input parameter in Figure 43.
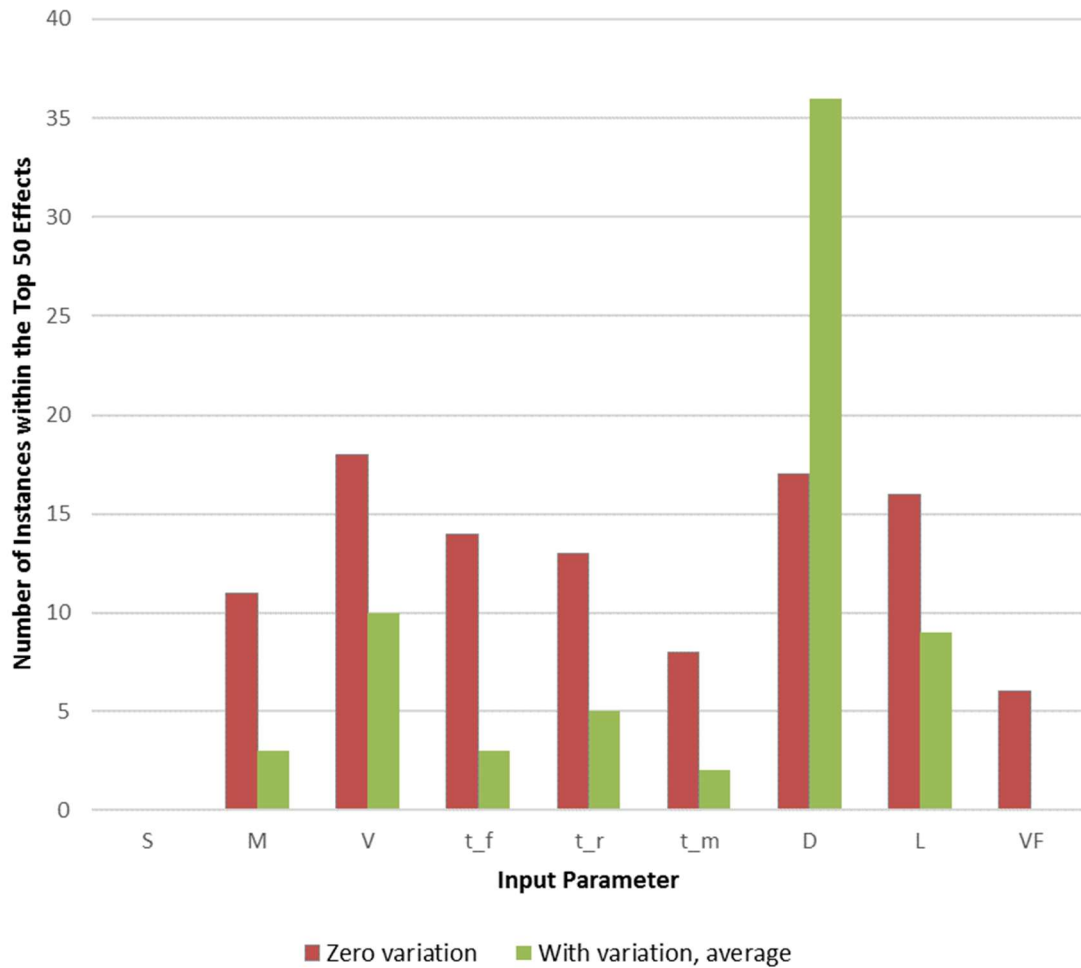
Figure 44: Number of instances of each primary input parameter within the top 50 significant terms in the material variation study, using average output parameters, side by side with zero material variation data.

It is observable that diameter (D) is incredibly critical with variable material properties. Velocity, magnetic field strength and regenerator length are relevant, but an order of magnitude less so than diameter. With the exception of diameter, all design parameters are observed less in the top 50 effects than in the zero variation study. Curvature terms show a similar change in Figure 45.
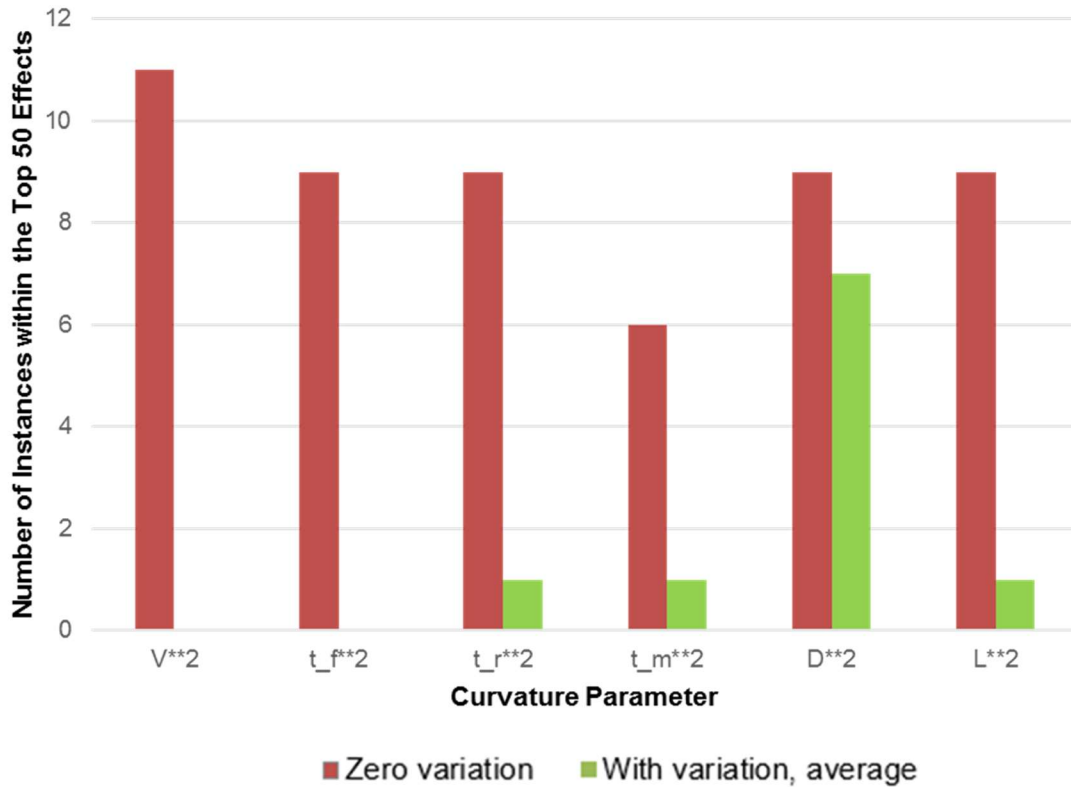
Figure 45: Number of instances of curvature terms within the top 50 significant terms in the material variation study, using average output parameters

Less occurrences of all curvature parameters are observed as compared with the zero variation study. Diameter shows the least reduction in prevalence between zero variation and with variation, average. Velocity, which was the most numerous term in

the zero variation study, has declined to zero in the variation study. Figure 46 shows the

number of instances of each material variation input parameter in Figure 43.
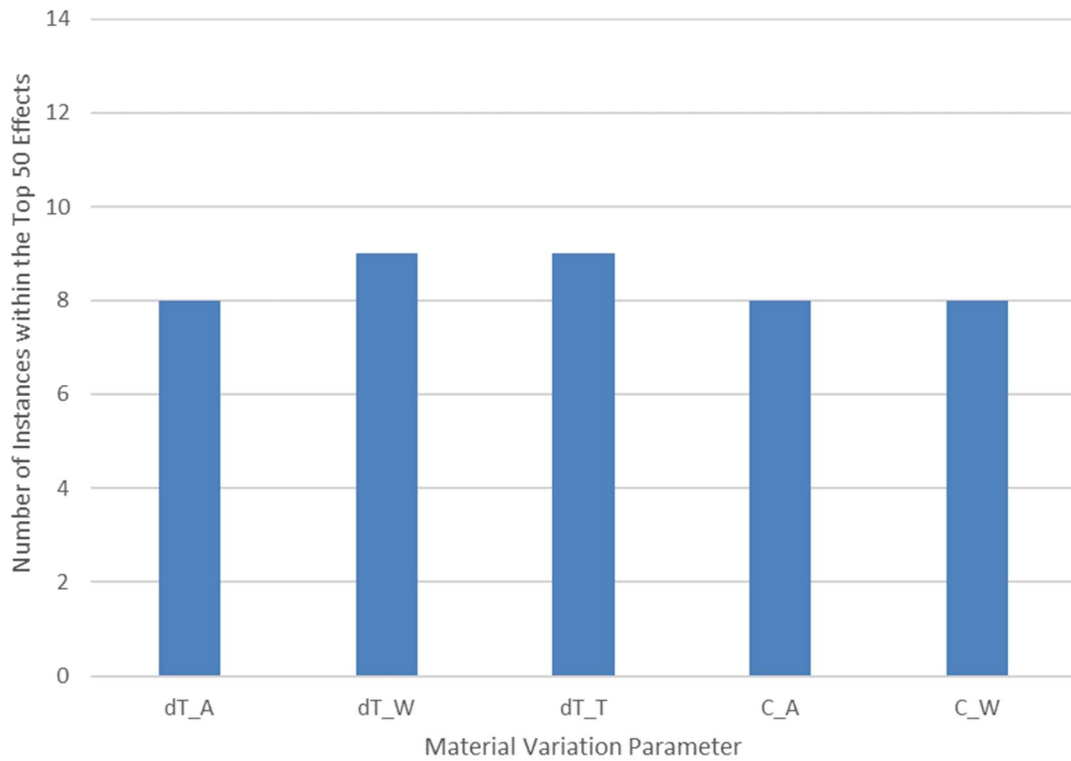
Figure 46: Number of instances of each material variation input parameter within the top 50

significant terms in the material variation study, using average output parameters.

In great contrast to primary design parameters in Figure 44, material variation

parameters are evenly observed as significant effects on performance, dwarfed only by

channel diameter in overall occurrences within the top 50 effects.   These material

variation parameters have replaced a large portion of the top 50 effects from the zero

variation study.

4.2.2 – Lower Limit Cooling Power and COP

Lower limit cooling power is more useful for a machine designer than average cooling power, because worst-case performance typically must still reach a predetermined threshold. A heat pump must be over-built in order to reach targeted limits on performance with a level of statistical confidence. For instance, if a designer determines that at least 150 W of cooling are required to cooling a space, the heat pump would be designed to a higher cooling power, perhaps 160W to account for variation during production.

Lower limit performance contains more information than average performance, as it requires an average and a standard deviation of data taken at each design point. Each time a design is simulated, a new magnetocaloric cascade is generated, which produces a different efficiency and cooling power density output. Standard deviation is calculated as

$$SD = \left(\frac{\sum Y^2}{N} - \overline{Y}^2\right)^{0.5} \tag{45}$$

where $\overline{Y}$ is the average output at a particular design point, N is number of iterations at a design point, and Y is the output of each iteration at a particular design point. A 6-sigma lower limit is used in this study, indicating that the design point lower limit is 6 standard deviations below the average output for the design point. In terms of machine design, this suggests that a heat pump would be "over-designed" to achieve a much higher cooling power density and efficiency on average, such that a particularly weak magnetocaloric cascade will still reach the minimum required cooling power density and efficiency.

For this portion of the study additional replicates are required because of the need for a mean and standard deviation for each parameter combination. Material variations parameters were consolidated into a 3 overall variation levels by summing the normalized levels across all 5 variation parameters shown in

		dT_A (K)	dT_W (K)	dT_T (K)	C_A (J/kgK)	C_W (K)
Levels	**1**	0.494	0.677	0.845	141	0.356
	0	0.247	0.339	0.423	70	0.178
	-1	0	0	0	0	0

Table 9 for each of the 100,000 simulation points. For instance, a simulation with all variation parameters at the highest levels sums to the maximum value of 5 using coded units. The average value of this summation across all simulated design points is 0 because the study is evenly distributed across all variation levels. Low, medium, and high levels of overall variation were broken up as follows based on the summation of normalized variation parameters: -5 to -2 for low, -1 to 2 for medium, and 3 to 5 for high. An assumption of equivalent effect for the 5 variation parameters is necessary to take this step in consolidating the data. It is shown in section 4.2.1 that all material variation parameters do show similar effect.

Because of this agglomeration of points, additional replicates now exist for each design point, and lower limit cooling power and lower limit Carnot ratio can be calculated for input parameter combination. Interestingly, this means that there is now overlap between material variation parameters in the analysis, although an effect can still be calculated for each. Lower limit output can be observed with previously presented data in Figure 47.
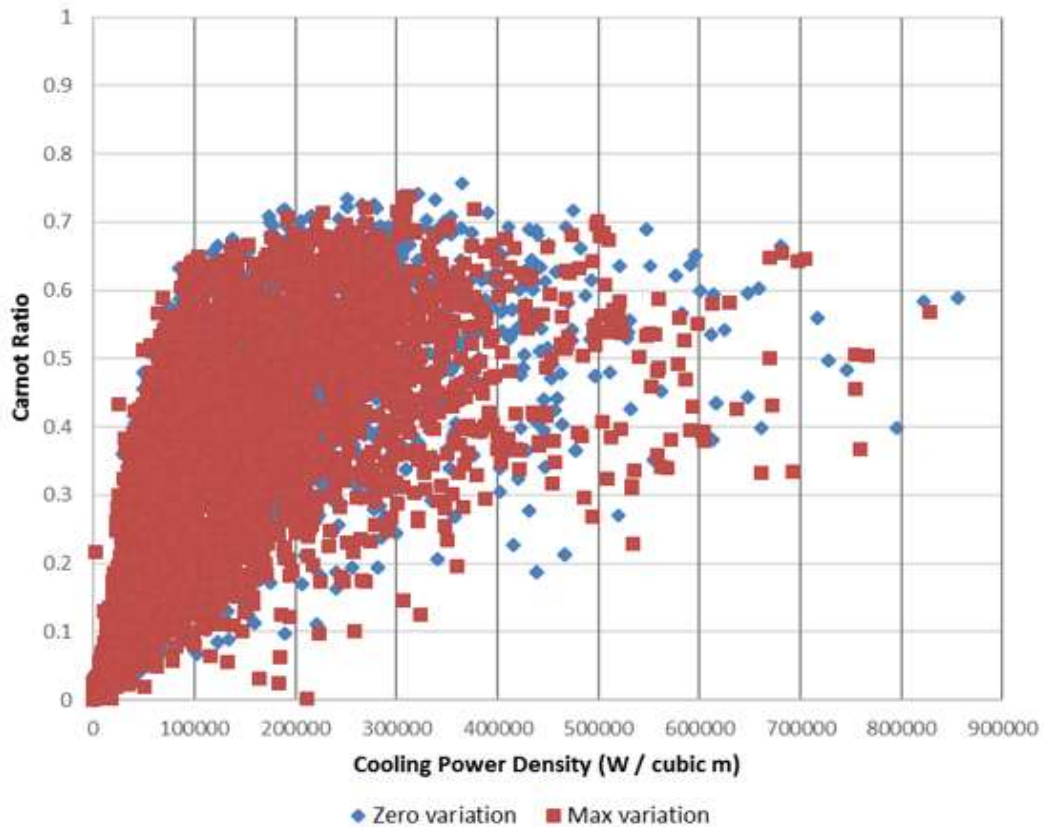
Figure 47: Cooling power density versus ratio of Carnot COP for lower limit data points; separated by zero variation and max variation levels.

Lower limit output generally appears nearer to the origin of Figure 47 than zero variation output, having both a lower Carnot ratio and a lower cooling power density. Maximum efficiency drops from 75% of Carnot COP in the zero variation study to 73% in the lower limit variation study using maximum variation levels, a drop of about 3%. It is critical to note that many design points dropped by more than 3%. Average Carnot ratio dropped from 36% to 32%. Maximum cooling power density maximum dropped by 3.5%, and average cooling power density dropped by 10%. Again, the top 50 effects are seen in Figure 48.
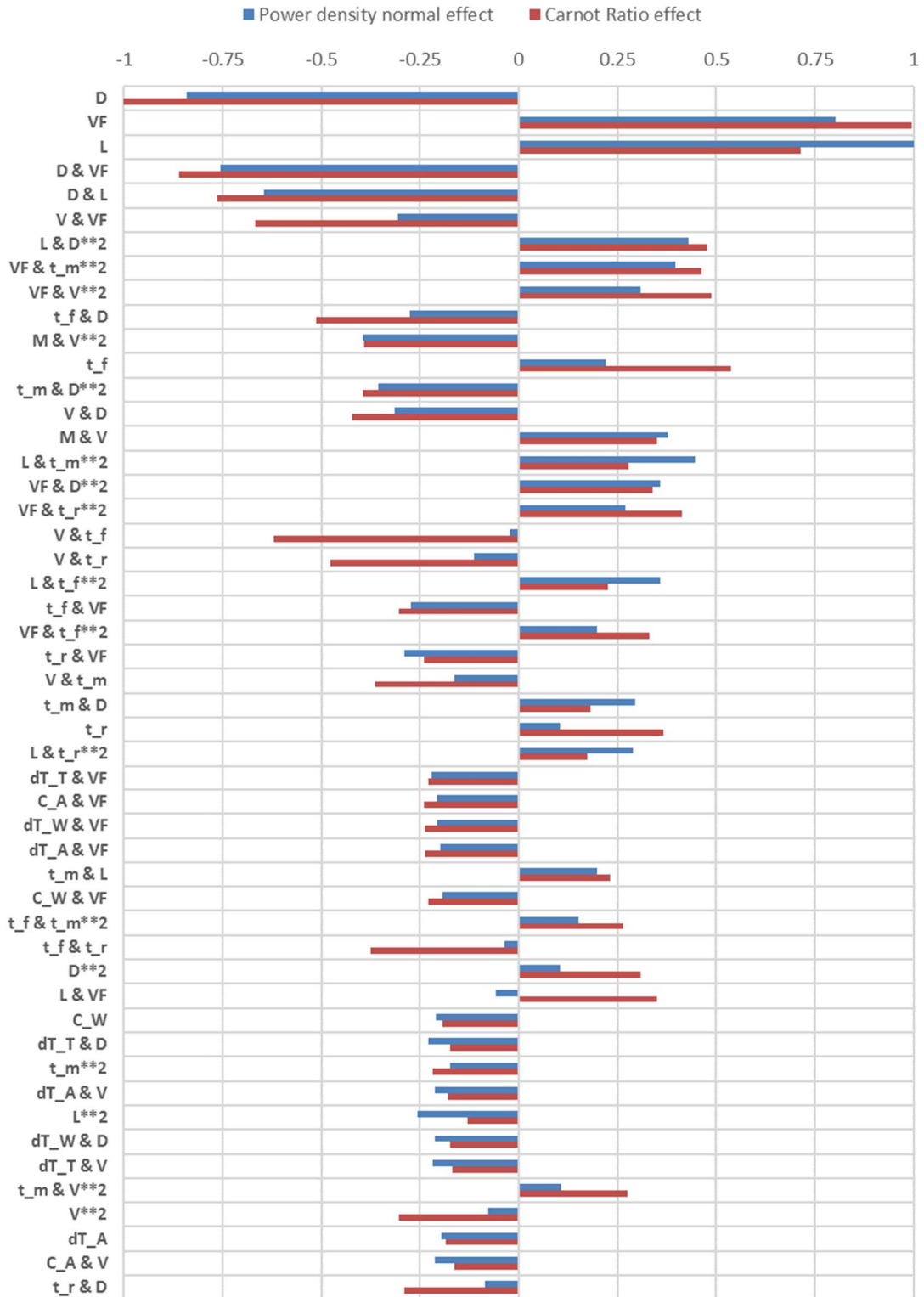
Figure 48: Main effects and interactions as fractions of maximum output of all cases for lower limit cooling power density and average COP with material property variability.

Diameter remains the largest effect by far and length remains near the top of the list, although other parameters have substantially shifted in importance. Void fraction is now quite high on the list, and also interacting strongly with various material parameters. Larger void fractions lead to higher efficiency and lower cooling power. Standard deviation of peak location has dropped in importance as compared the average performance study of section 4.2.1, suggesting that it produces a consistent detriment to performance. In this way it reduces average performance and lower limit performance by a similar amount. In contrast, several design parameter interactions have risen back towards the top of Figure 48, suggesting that they affect average performance in a less consistent way. This is easier to see in occurrence counts for design parameters.
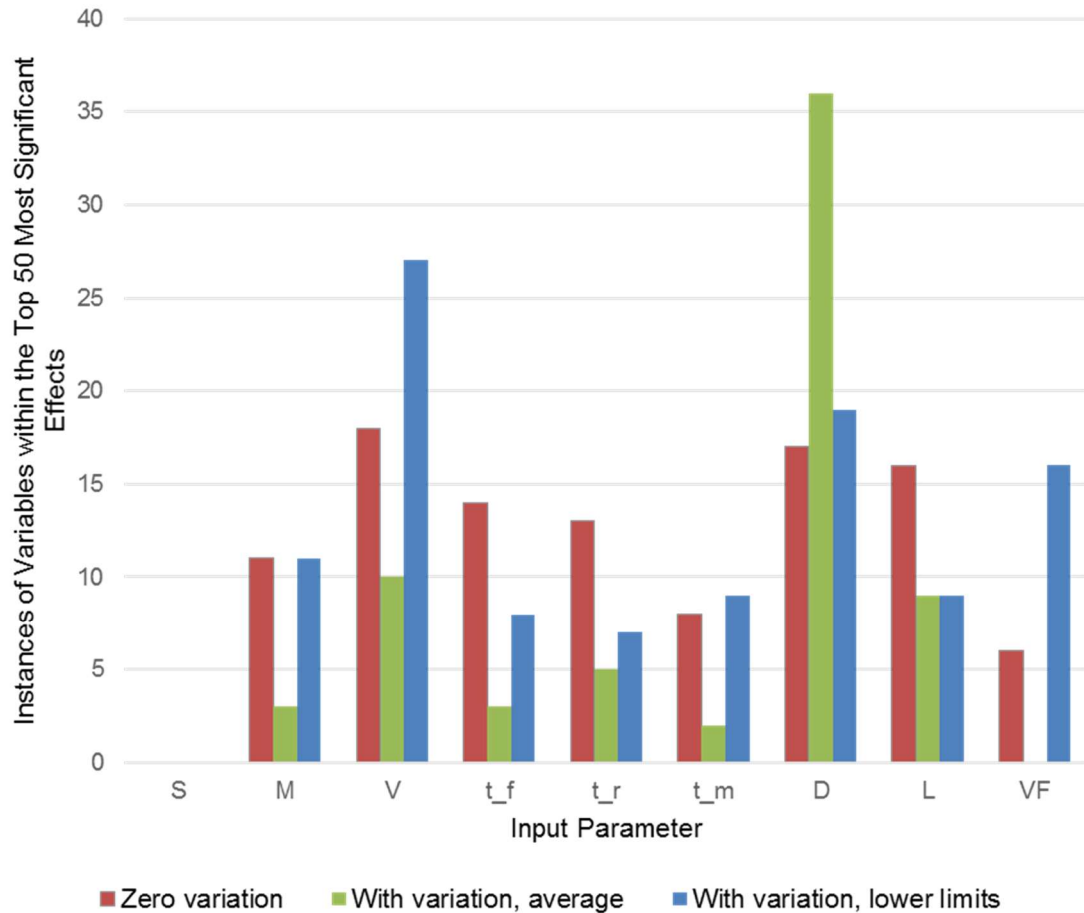
Figure 49: Number of instances of each primary input parameter within the top 50 significant terms using zero variation data and variation inclusive data, analyzed using average and lower limit methods.

Within Figure 49 it is observable that "zero variation" and "with variation, lower limit" are much more similar to each other than to "with variation, average", which utilizes averages rather than lower limits. In looking for realistic lower limit performance, fluid velocity is a more critical design parameter than it would be if designing without accounting for variation in material properties. Flow time, ramp time, and length are somewhat lower in importance, and other parameters are quite flat between the studies.
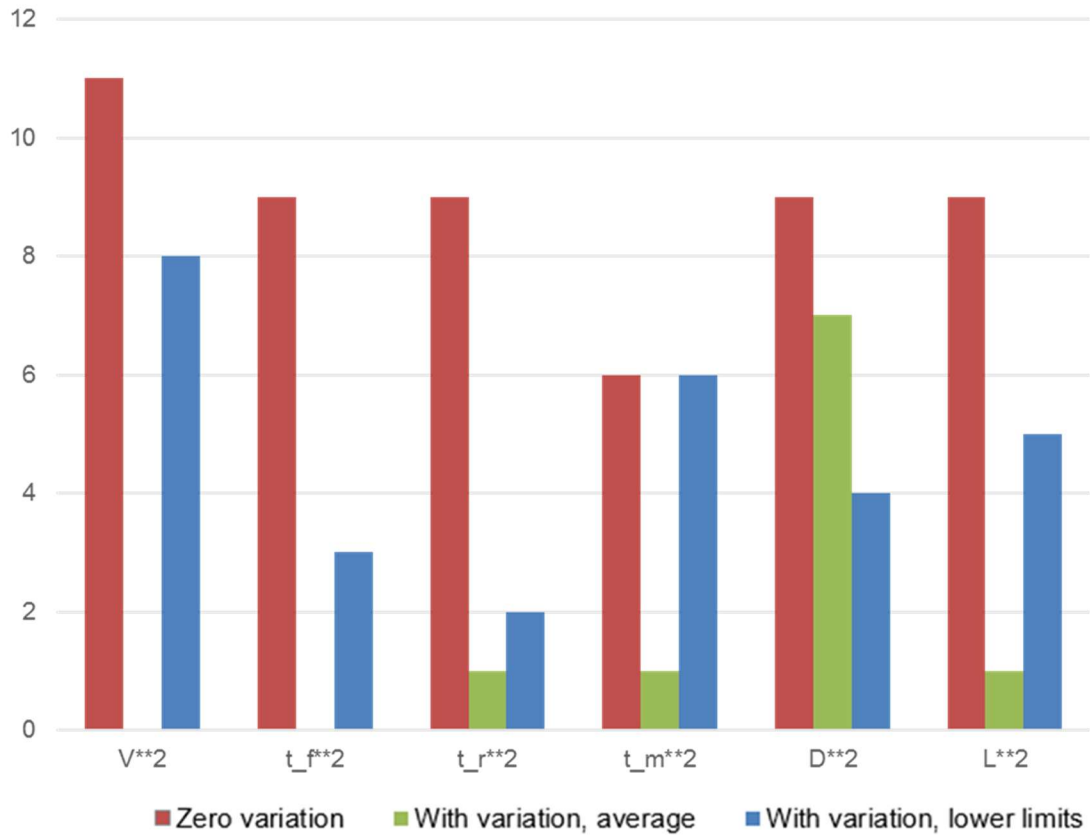
Figure 50: Number of instances of each curvature input parameter within the top 50 significant terms using zero variation data and variation inclusive data, analyzed using average and lower limit methods.

Within Figure 50 it can be seen that curvature terms become less relevant in the lower limit study than in the zero variation study. These terms were nearer to the end of the top 50 rankings in the zero variation study, and some were displaced by material variation terms.
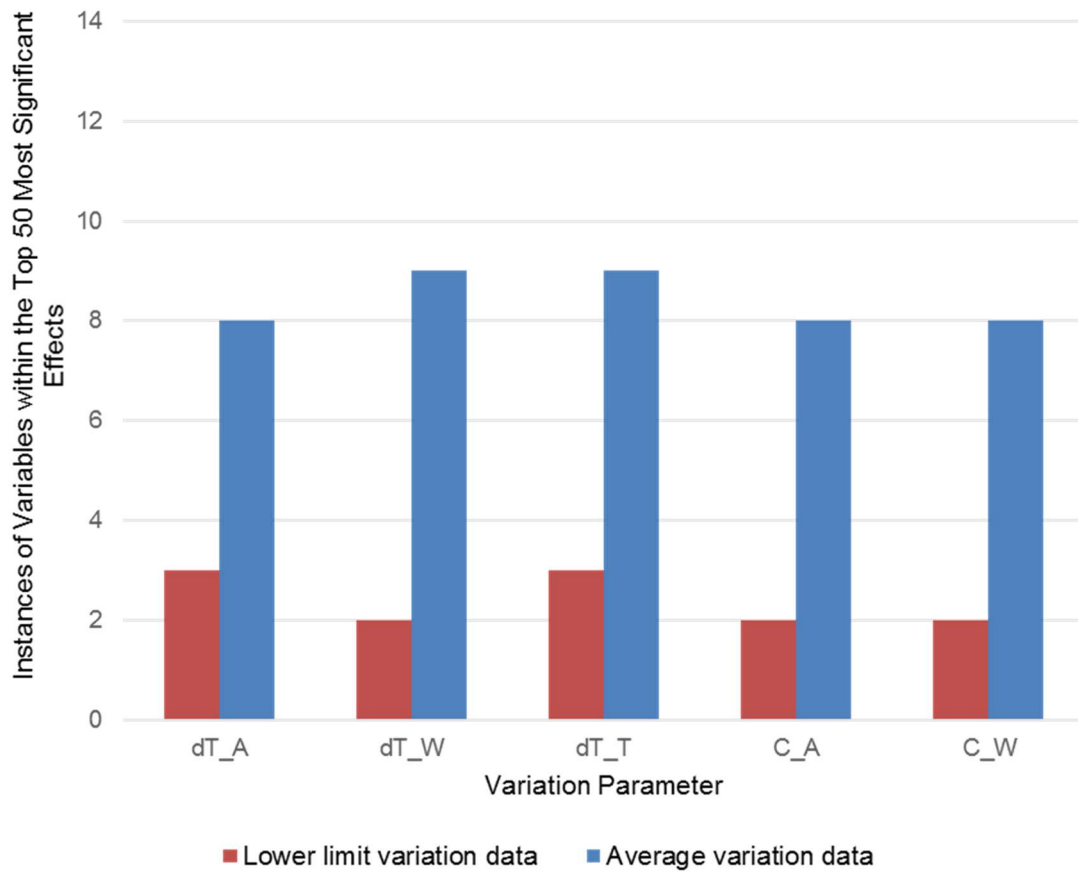
Figure 51: Number of instances of each material variation input parameter within the top 50 significant terms using variation inclusive data, analyzed using average and lower limit methods.

Figure 51 shows that, again, material variation terms displaced other parameters which dropped off of the top 50 list. Material variation terms do appear much less frequently in the lower limit study than in the average study, as expected. Material variation terms are expected to have less effect on the output due to the agglomeration of similar levels needed to produce replicates for the lower limit study. There is overlap between material variation parameters in the analysis, which would be expected to reduce the effect of individual material variation parameters in analysis.

5 – HIGH LEVEL INTERPRETATION AND DISCUSSION OF RESULTS

5.1 – High Level Study Interpretation

At a high level, effects from the lower limit analysis match the zero variation study more closely than effects from the average-based analysis study. In industry it is much more relevant to take a lower limit approach on the design process, which makes lower limit results most relevant. Simulations performed without material variation are still highly relevant to our understanding of magnetocaloric technology. This is a major conclusion of the present work. High performing designs saw a reduction in lower limit performance due to material property variation of 2.5% to 5% in Carnot ratio, although many cases saw much more, as shown in Figure 52.
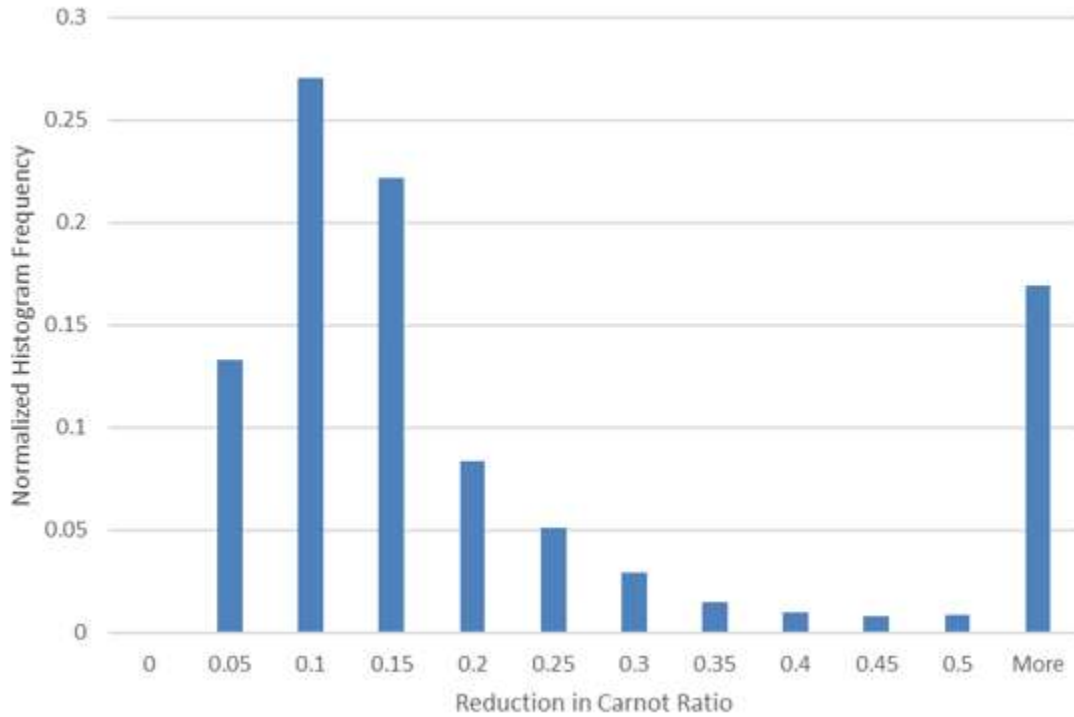
Figure 52: Histogram of reductions in Carnot ratio due to material property variation.

Figure 52 is based on the performance change of each individual input parameter combination in the zero variation and lower limit studies, containing 5832 unique cases. Median reductions in performance are in the 0.05 to 0.10 range and data skews strongly toward higher values. When looking at simulations studies with zero variation in material parameters, it would be useful to assume such a degradation to simulated efficiency unless better data exists. Reduction in cooling power is nearly identical, as seen in Figure 53.
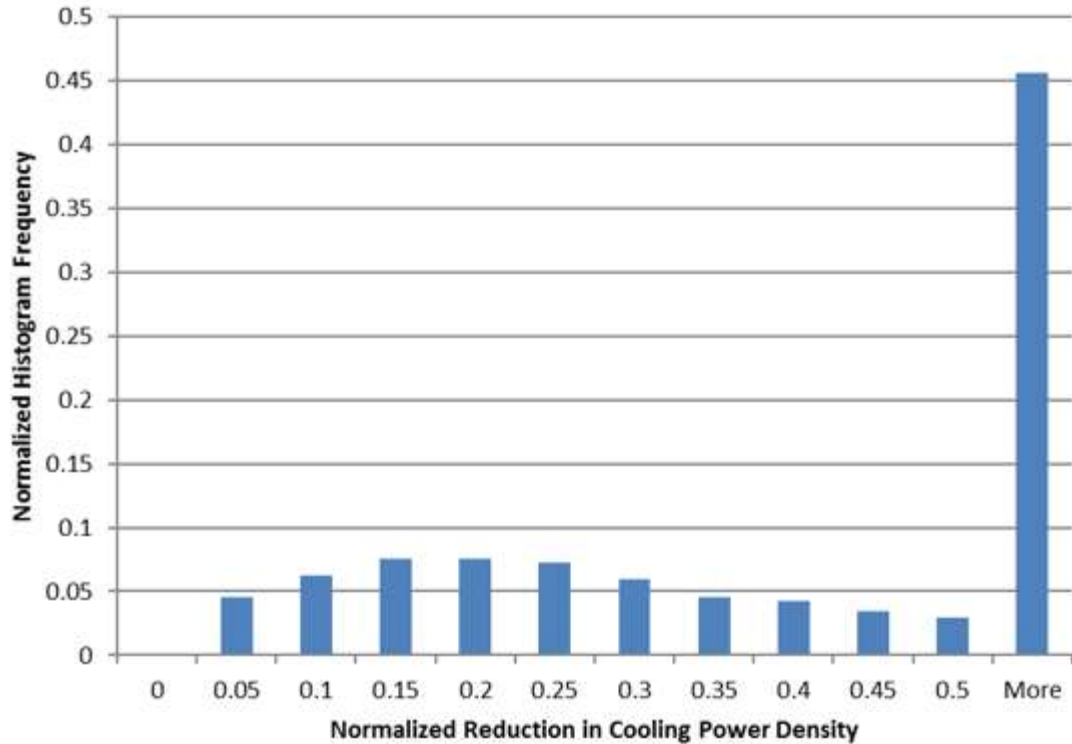
Figure 53: Histogram of normalized reductions in cooling power density due to material property variation.

For cooling power density, the histogram peak reduction in performance occurs at 15 to 25 percent of zero variation cooling power density. Again, the highest cooling power density cases do see 5 to 10 percent reduction in performance. When looking at simulation studies with zero variation in material parameters, it would be useful to assume such a degradation to simulated cooling power unless better data exists. In this way, an uncontrolled "noise" factor effect can be approximated.

Taking a deeper look at individual design parameters and their relative importance, channel diameter is vastly more important to the design process than any other parameter, as seen in Figure 48. Figure 49 shows that fluid velocity has become more critical than it was when assuming zero variation of material properties, although

still less important than diameter. When looking for occurrences of velocity in Figure 48

it becomes apparent that all occurrences are interaction terms, which makes a design

process less straightforward. Velocity must be optimized with all other parameters

simultaneously. Diameter and velocity are also the terms that most often interact with

material property variation parameters, which again illustrates their importance in a

design process that includes material property variation.

Considering the materials themselves, it has been shown that there are some

parameters that are more import to control than others, although only marginally so.

Practically, all five material property variation parameters need to be controlled to a

similar degree. Peak amplitudes and widths need to be maximized as well to maximize

performance. This may be a positive consequence of better process control that is not

captured in this study.

5.2 – Detrimental Effect of Variability in Material Properties on Performance

5.2.1 – Entropy Generation due to Fluctuations in Temperature Gradients

Main effects and most interactions with material variability parameters are

significant for lower limit Carnot ratio output, as shown in section 4.2.2. This suggests

that stage-to-stage variability leads to entropy generation and a reduction in efficiency.

In addition to local irregularities within the temperature profile following a magnetic

transition, average temperatures across the span of the regenerator will be more

irregular with inconsistent material properties. As a case study, a high performing

regenerator will be looked at in more detail. Input parameters for the design points are

found in Table 10.

Stages	45	
Velocity	0.03	m/s
Magnetic strength	1.50	Tesla
Channel diameter	0.0001	m
Void fraction	0.50	
Flow time	0.275	s
Ramp time	0.5	s
Magnetization time	0.05	s
Regenerator length	0.15	m

Table 10: Input values defining a regenerator design for a case study.

This case achieved just over 75% of Carnot COP and 25 Watts of cooling,

equating to 33,333 W/m^3 cooling power density based on regenerator length (0.15m)

and area (0.005m). Parameters match up well with main effects in the analysis, having

a large length, smallest diameter channels, and a high void fraction.
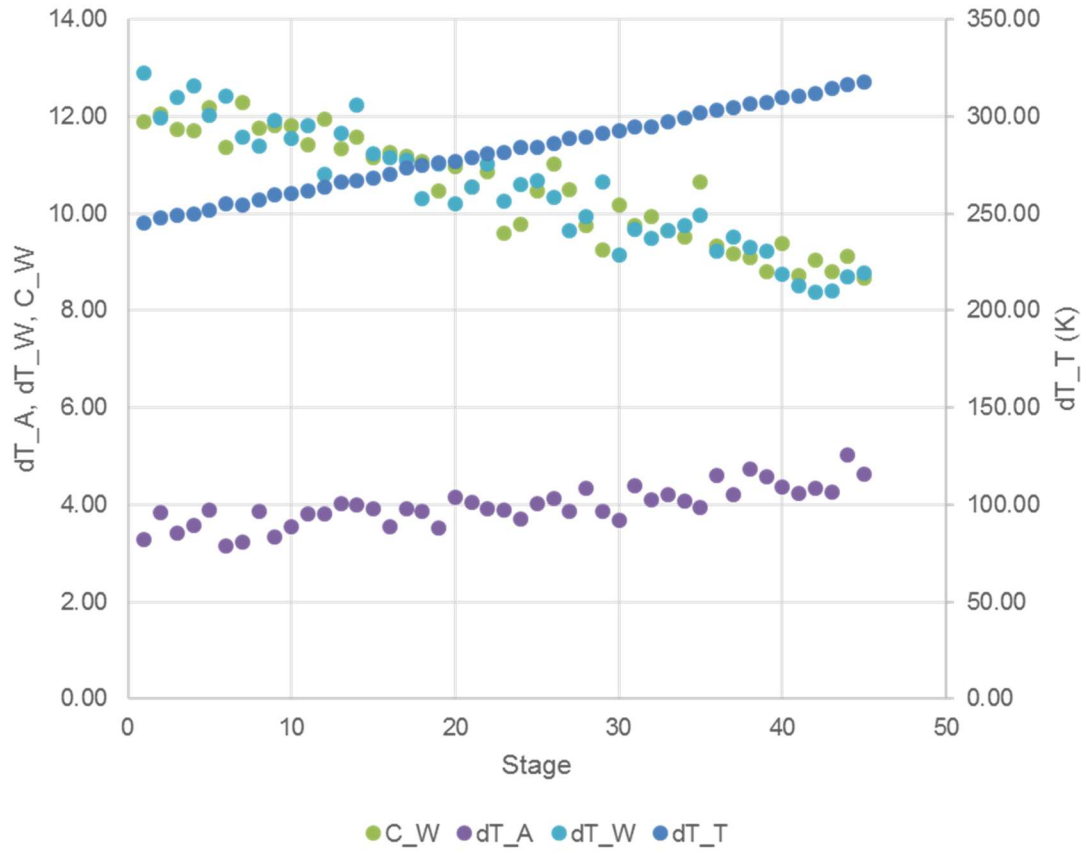
Figure 54: Stage values for magnetocaloric effect (dT_A), peak width (dT_W and C_W), and peak location (dT_T) for a high performing regenerator with high material property variation.

This particular simulation utilized high levels of material property variability, yielding cascade parameters depicted in Figure 54. Such variation across the temperature span of the regenerator produces the temperature profiles shown in Figure 55.
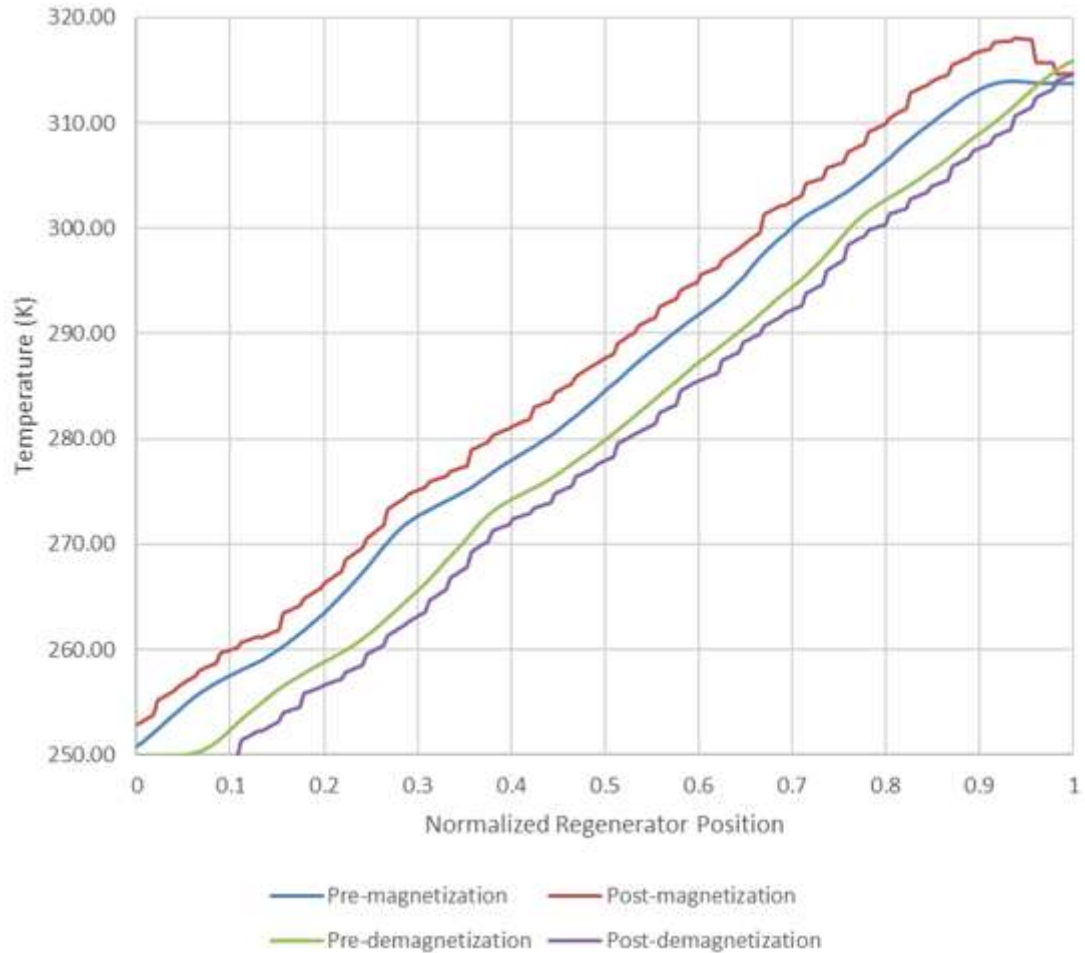
Figure 55: Temperature profiles before and after each magnetic transition in the highest efficiency regenerator design with high material property variation.

Within Figure 55 the jagged post-transition profiles can be observed. An ideal temperature gradient thermodynamically is linear, as it creates the least amount of entropy generation due to heat transfer. Figure 55 shows that material variation not only leads to entropy generation immediately following magnetic transitions, but also throughout the entire cycle. Due to variations in Curie temperature many curves do not reach peak MCE amplitude. Creating local temperature gradients that differ substantially from the average regenerator temperature gradient will have a negative

impact on efficiency, as it qualitatively represents entropy generation. Entropy that goes into the cycle magnetically in order to generate the magnetocaloric effect is partially wasted in forming temporary gradients, which are dispersed as the cycle moves on. For reference, the same design point without material property variation contains linear cascade properties, shown in Figure 56.
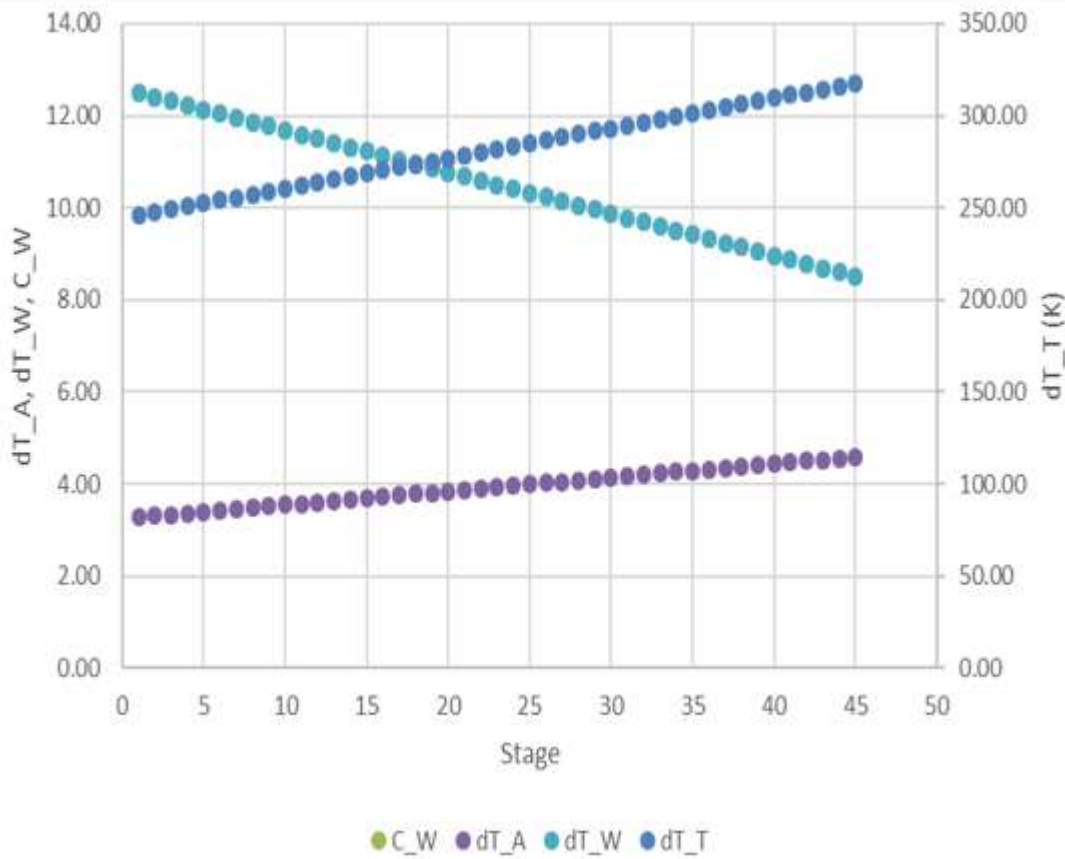
Figure 56: Stage values for magnetocaloric effect (dT_A), peak width (dT_W and C_W), and peak location (dT_T) for a high performing regenerator with zero material property variation.

The regenerator described in Figure 56 produces a much smoother and more linear effect, shown in Figure 57. There are no neighboring stages with large differences in magnetocaloric effect or peak width, and a much smoother temperature profile results.
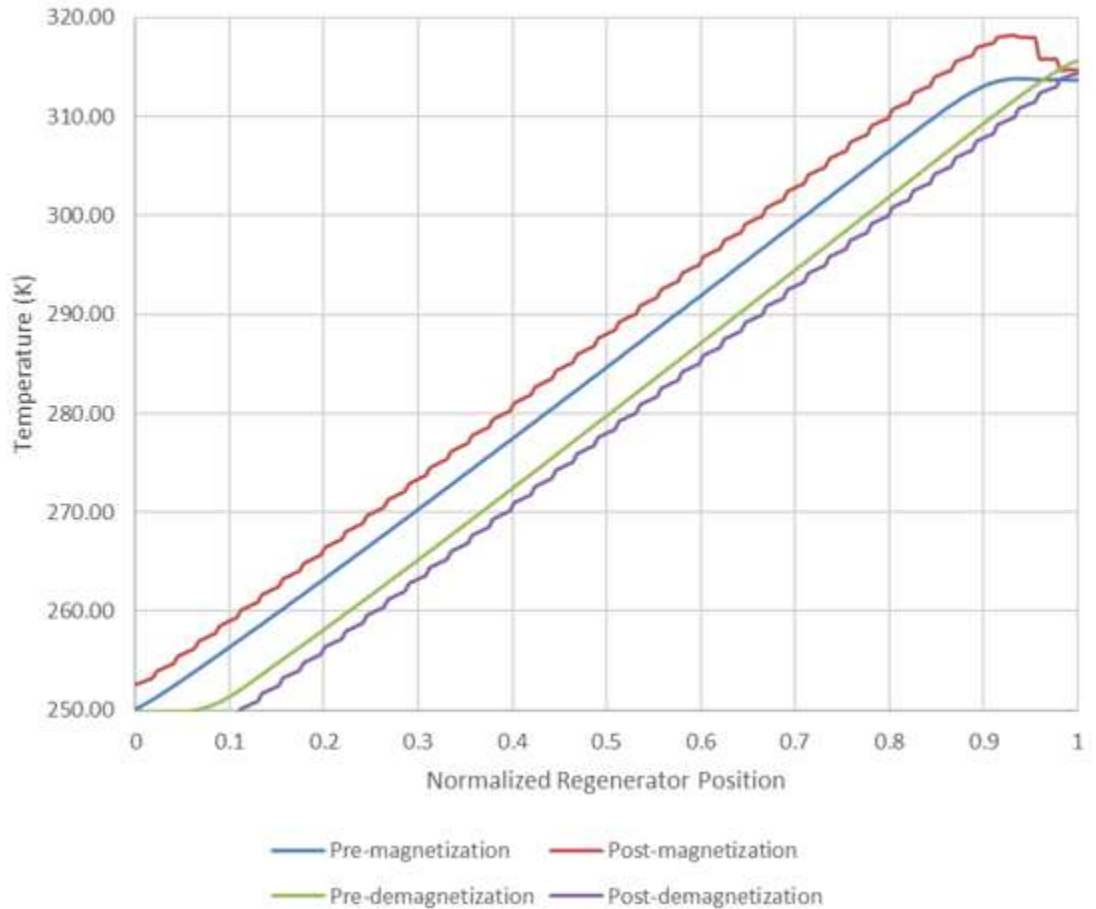
Figure 57: Temperature profiles before and after each magnetic transition in the highest efficiency regenerator design with zero material variation.

Figure 57 shows a much smoother and more linear temperature profile than Figure 55, which illustrates again the effect of variation in magnetocaloric material properties. In fact, much of the profile is perfectly linear, with a slight flattening near the ends.

5.2.2 - Mismatch of Design Parameters with Cascade

A second mode of entropy generation due to material property variation is the mismatch of design parameters, which creates imbalances in the system. Every input parameter effects this balance, and each design must be looked at holistically to negate

the detriment of material variability on performance. A highly efficient cycle is well balanced thermodynamically, and in a cascaded regenerative system, this means that the weakest or farthest spaced stage will limit the entire cascade. Logically this suggests that a cascade with too few stages for a given temperature span will be less robust to material variation. A fairly small effect was observed in this study related to stage spacing, meaning that this limit on minimum stage spacing may be outside the envelope of study. In a similar way, materials having a wider peak effect as a function of temperature are more robust to variation. Both of the effects were observed in simulation studies referenced in section 1.5.2, with Lei et al. (2015) specifically showing both effects.

Another input parameter which helps reduce the effect of material property variation is fluid displacement ratio,

$$FDR = \frac{v_{sf}(t_{flow} + t_{ramp})}{\varepsilon \, L_{regen}} \tag{46}$$

where v_{sf} is superficial peak velocity, ε is void fraction, L_{regen} is regenerator length, t_{flow} is peak flow time, and t_{ramp} is ramping flow time. Practically, this is the amount of fluid contained within the regenerator that is exchanged during each flow period, which occurs twice per cycle.
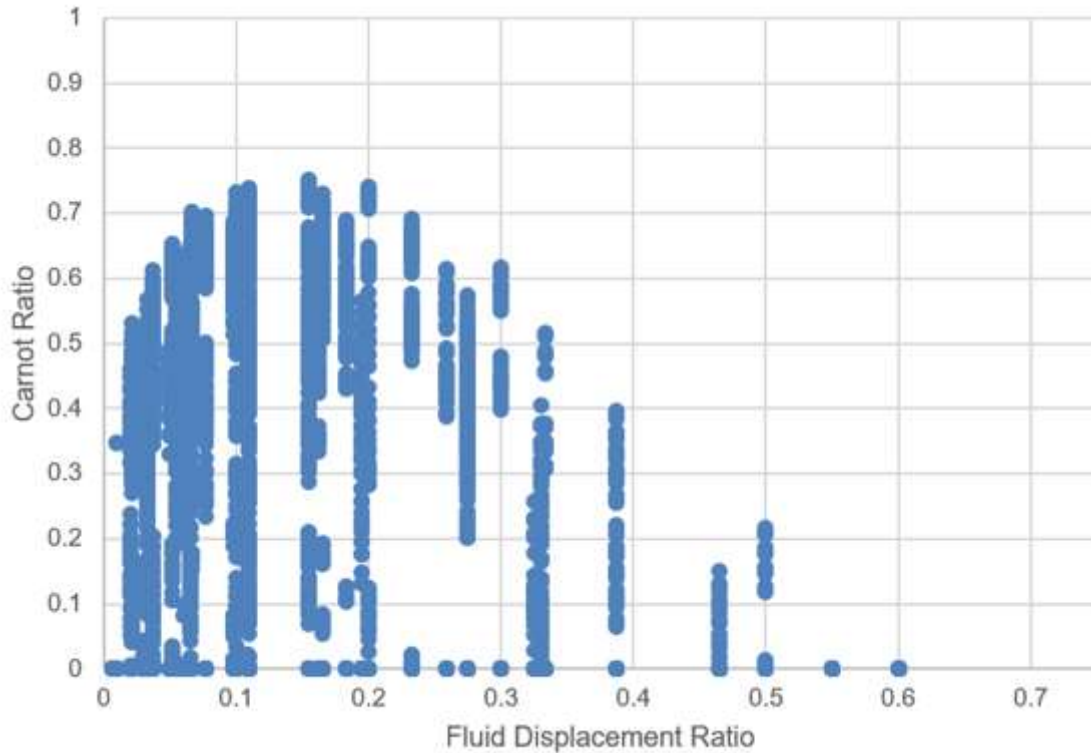
Figure 58: Carnot ratio as a function of fluid displacement ratio in the zero variation study.

As seen in Figure 58, an extremely low fluid displacement ratio leads to poor performance related to dead volume, where most of the rejected heat is stored in un-exchanged fluid volume at the regenerator ends. In a theoretical machine with zero dead volume, this is neglected. A very large fluid displacement ratio leads to wash-out, a phenomenon in which the moving thermal mass of fluid exchanges too much heat with magnetocaloric material, and drives MCM temperature away from Curie temperature. As an extreme example, flowing fluid through a regenerator steadily will bring the entire regenerator to the same temperature as the fluid, bringing nearly all stages' temperatures far away from peak magnetocaloric effect temperature. Magnetic transitions occurring while MCM temperature is not near Curie result in minimal temperature change. Having a moderate fluid displacement ratio per cycle, 15-25% for

example, helps negate the detrimental effect of singular bad stages or "weak links" in the cascade by exchanging heat beyond nearest neighboring stages. In this sense, it would be reasonable to ensure that fluid displacement ratio per stage is much larger than 1. Fluid displacement ratio per stage would be calculated as

$$FDR_{stage} = \frac{v_{sf}(t_{flow}+t_{ramp})}{\varepsilon\, L_{regen} N_{stages}}$$ (47)

where v_{sf} is superficial (empty channel) velocity, t_{flow} is peak flow time, t_{ramp} is ramping flow time, ε is fluid fraction or void fraction, L_{regen} is regenerator length, and N_{stages} is the number of stages. Stage count is either 45 or 55 for all designs in the present work, and 20% FDR translates into 9-11 for stage FDR. This means that about 10 stages are directly interacting through fluid displacement in a good cycle.

Looking only at second order interactions, the effect of fluid displacement ratio relates to interactions between velocity, flow time, ramp time, length, void fraction, and magnetocaloric property variation parameters. High order interactions such as these make magnetocaloric system quite difficult to study.

5.2.3 – Thermodynamically Pairing Cascades to Regenerator Designs

If a material existed that could provide constant MCE as a function of temperature, it would be represented by a horizontal line in MCE as a function of temperature. An ideal material cascade may actually provide slightly greater MCE on the hot side as compared to the cold side. In this way each stage can pump the same amount of heat at the same temperature gradient for perfect stage-to-stage matching. This is shown in Figure 59.
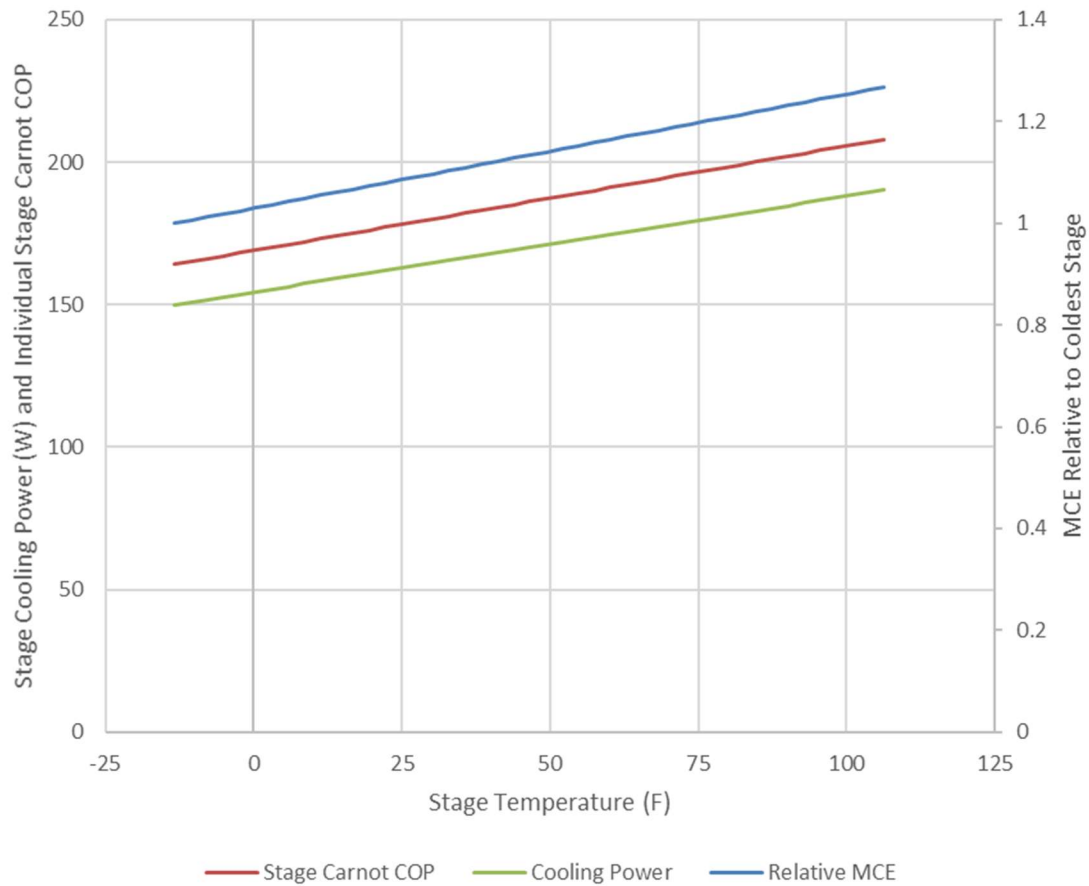
Figure 59: Ideal MCE as a function of temperature for a Carnot heat pump.

For Figure 59, 150 W of cooling at the cold end and power input requirements based on the Carnot cycle efficiency for each stage are assumed. Each stage is approximated to only interact with directly adjacent stages. Stage spacing is assumed to be 1.5 K, meaning that each stage has a span of 1.5 K. Carnot COP for each stage is based on temperature and span,

$$COP_{stage} = \frac{T_c}{T_h - T_c} \qquad (48)$$

Warmer stages must convey more heat in operation because of thermodynamic losses, where rejected heat must always exceed accepted heat, and each stage must follow the second law of thermodynamics. The cascade as a whole also follows this law indirectly, resulting in a total cascade COP of about 4 if all stages' losses are summed, equaling the Carnot COP for a cooling heat pump of the total span. Relative MCE in Figure 59 is the relative MCE required for each stage, as compared with the coldest stage. Stage strength changes between the cold and hot cascade ends could foreseeably be accomplished directly via material peak MCE. As an example, if the coldest stage operates with a 3 K peak MCE amplitude, the hottest stage should have a peak MCE amplitude of about 3.78, 26% greater than the coldest stage. This 26% increase allows thermodynamic losses to be perfectly balanced with a cascade's ideal operating point, allowing each stage to operate near peak strength and efficiency.

Other losses, such as viscous heat generation or radial heat leak, can be accounted for in the same way as thermodynamic losses in Figure 59. When a MCM cascade is perfectly matched to losses, each stage can operate at near peak strength with minimal losses. Cascade Schroeder-LaFeSiH exhibits 30% stronger warm-side MCM than the cold side based on temperature change, which is nearly ideal if the stage-to-stage variation is ignored. When a MCM cascade is not well matched to losses, the temperature gradient will compensate to reach equilibrium, forcing stages to operate off-peak, and generally reduce COP and power.

6 - COMMERCIAL VIABILITY OF THE TECHNOLOGY

The greater context of the present work is to drive magnetocaloric technology toward commercialization. Material variability should be reduced, but the driving force for this reduction is found in machine cost. Looking at Chapters 4 and 5 in isolation would lead one to believe that material property variation only leads to a marginal detriment to performance, which is partially true. However, it will be shown that a marginal decrease in efficiency and cooling power density leads to a major increase in estimated machine price. Several hurdles also exist in order to achieve this goal of commercialization, including microchannel production, overall system cost reduction through machine innovation and material variation reduction, and market need.

6.1 – Microchannel Size

One highlight of the present work is the massive effect of microchannel size on performance. Specifically, 0.0001 m channels produce much better cooling than 0.00025 m or 0.0005 m channels, with a strong trend to seek even smaller channels. Practically, there are limitations on channel size, although 0.00015 channels have been printed using magnetocaloric material at Oak Ridge National Labs using a scalable process (Momen, 2017). Scalability in this instance refers to the ability to produce large numbers of parts relatively cheaply and quickly in a factory setting, and is due to the inkjet printing process used. Inkjet, or binder jet, printing uses a print head with many nozzles, which spray a binder onto find powder to produce a solid part layer by layer. A single pass of the print head completes an entire layer, allowing relatively high speed

printing. Sintering or other processing can occur after initial printing to strengthen or

heat treat parts.
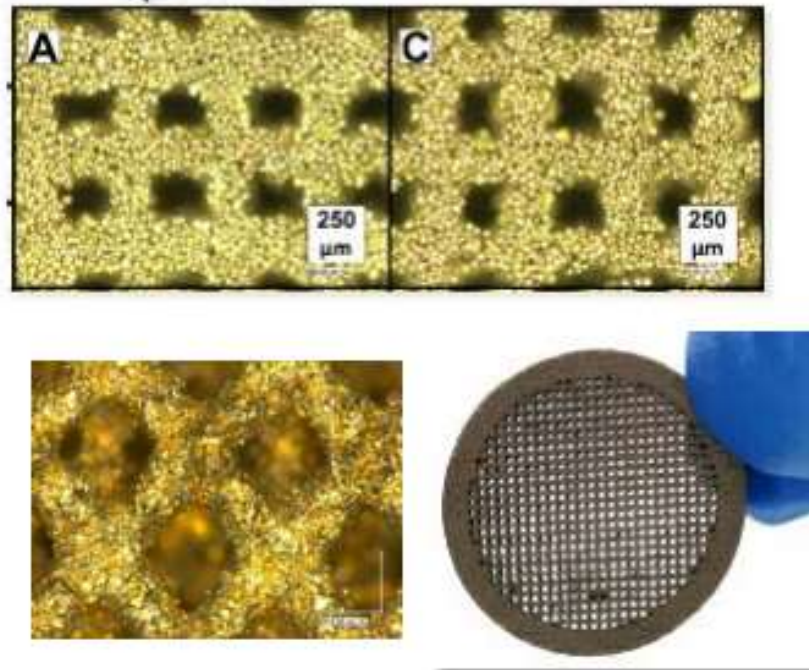
Figure 60: Images from (Momen, 2017) **showing printed magnetocaloric structures.**

Figure 60 shows an example of small 3D printed structures using magnetocaloric

material. 250 μm channels are shown, and 150 μm channels are considered printable

using current technology. This is an ongoing project that shows good potential to

provide the necessary microchannel structures at high production volume.

6.2 – Basic System Cost

Cost also needs to be considered as a part of the design process, and magnets

are one of the largest contributors to system cost based on internal work at GE

Appliances, as well as work by Bjørk et al. (2016) and Langebach et al. (2014). Cost

estimation and reduction of magnetic systems for magnetocaloric heat pumps has seen

considerable interest because of its relative criticality to move forward from research to product development for the mass market (Bjørk, 2010; Bjørk et al., 2016, 2010; Russek and Zimm, 2006; Tura and Rowe, 2014, 2011). Using multiple internal GE Appliances prototypes having a variety of magnetic systems as reference points, it is possible to correlate magnetic system requirements to regenerator size and measured magnetic field, providing the following relationship.

$$V_{mag} = 0.5\, L_{regen}\, A_{regen}\left(1.42215\, H^2 + H^{5.36762}\right) \qquad (49)$$

where V_{mag} is volume of magnetic material, L_{regen} is regenerator length, A_{regen} is regenerator frontal area, and H is magnetic field strength, in Tesla. \$40 per kg is assumed as bulk pricing on magnets, which are likely high performing Neodymium magnets (Langebach et al., 2014). Density is approximated as 7900 kg/m^3. Applying this relationship on the zero material variation study shows the cost of magnetic field strength, which rises dramatically between 1 and 1.5 Tesla fields strengths.
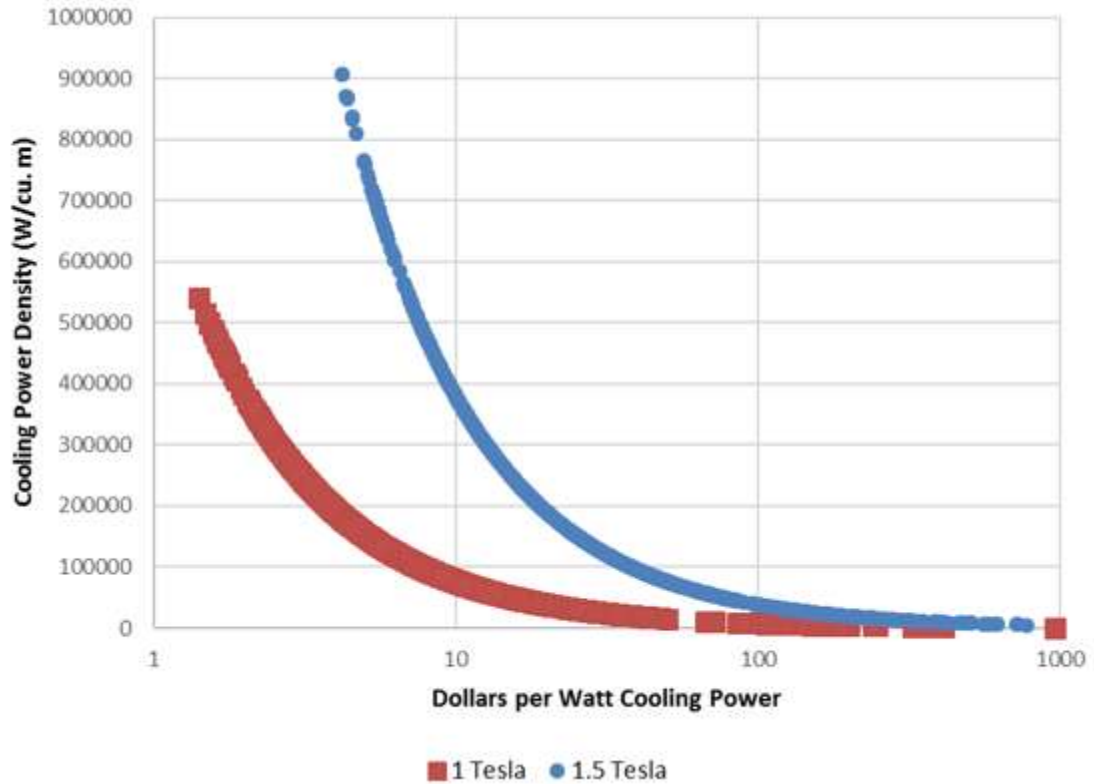
Figure 61: Cooling power density as a function of magnet cost per Watt cooling power, where the cost function is log scaled.

Figure 61 shows the nonlinear relationship between magnetic system cost per Watt and cooling power density. Larger magnetic fields provide higher cooling power density consistently. This also shows that magnetic field strength needs to be reduced to the absolute minimum level in order to build a cost effective product, and that no designs fell below $2 per Watt cooling power. A household refrigerator requiring 150 Watts of cooling would cost approximately 300 dollars within the constraints of this study, including only the magnetic system, which contains the vast majority of total machine cost. 150 Watts is approximately the cooling requirement for a large household refrigerator (Langebach et al., 2014). Motors, pumps, structure, and all other components are not included in this metric. There are a range of methods to reduce this

112

cost considerably, but using a magnetic field below 1 Tesla may be a necessity. In

contrast, maximum efficiency is achieved with 1.5 Tesla, showing the delicate balance

required in system design.
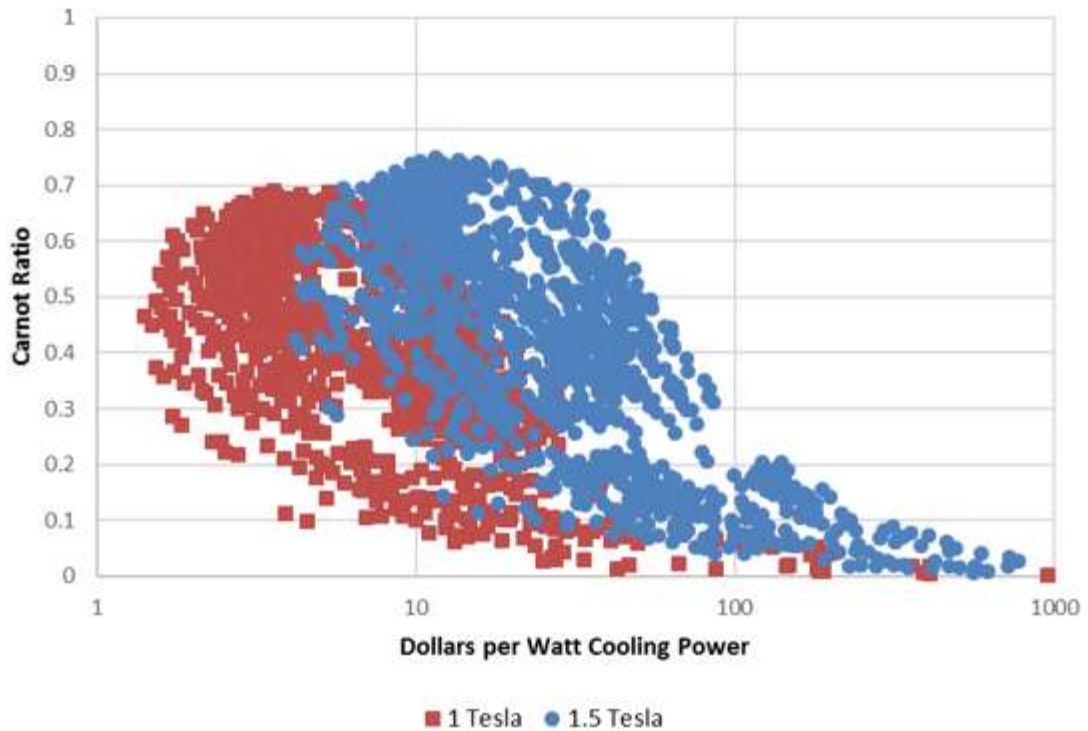
Figure 62: Carnot ratio as a function of magnet cost per Watt cooling power in the zero variation

study, where the cost function is log scaled.

For efficiency, Figure 62 shows another powerful relationship between magnetic

field strength and cost per Watt cooling power. Higher magnetic fields provide higher

efficiencies, but at a great increase to system magnetic cost. Higher efficiency is

meaningless to the average consumer if the cost is too great, as it becomes

unaffordable. Within the scope of the present work, a system designed to provide 72%

of Carnot COP would cost $1500 for 150 W cooling power with just the magnetic

subsystem; well beyond the total cost of many refrigerators in the market today. The

$300 system based on cooling power density alone in Figure 61 is equivalent in efficiency to high end vapor compression systems.

Regenerator cost must be put into perspective alongside magnetic system cost. Mass production of magnetocaloric materials has also been a topic for research for the same reasons as magnetic system cost (Zhang et al., 2017). Assuming magnetocaloric material is not more expensive than magnetic material, $40 per kg is assumed (Langebach et al., 2014). MCM volume is calculated as

$$V_{MCM} = L_{regen}A_{regen}(1 - \varepsilon) \tag{10}$$

where L_{regen} is regenerator length, A_{regen} is regenerator frontal area, and ε is void fraction.
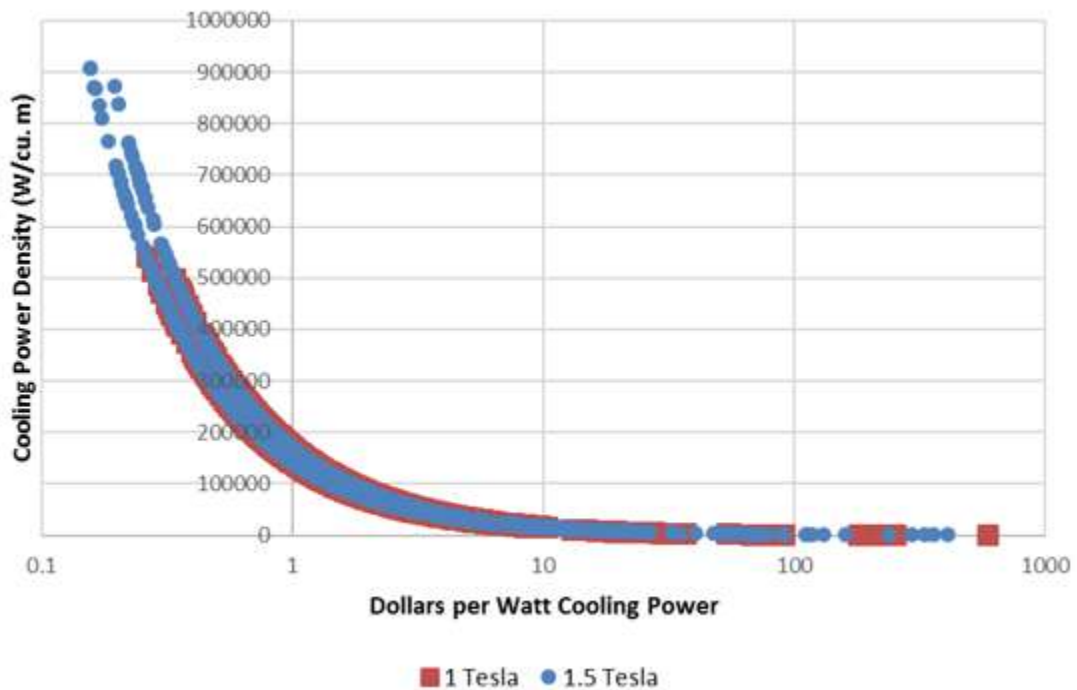
Figure 63: Cooling power density as a function of cost per watt cooling power of MCM, where the cost function is log scaled.

114

Figure 63 shows very little difference between magnetic field strength in the cost function for MCM, and bottoms out at about 0.16 dollars per Watt cooling power. Efficiency responds very differently, as shown in Figure 64.
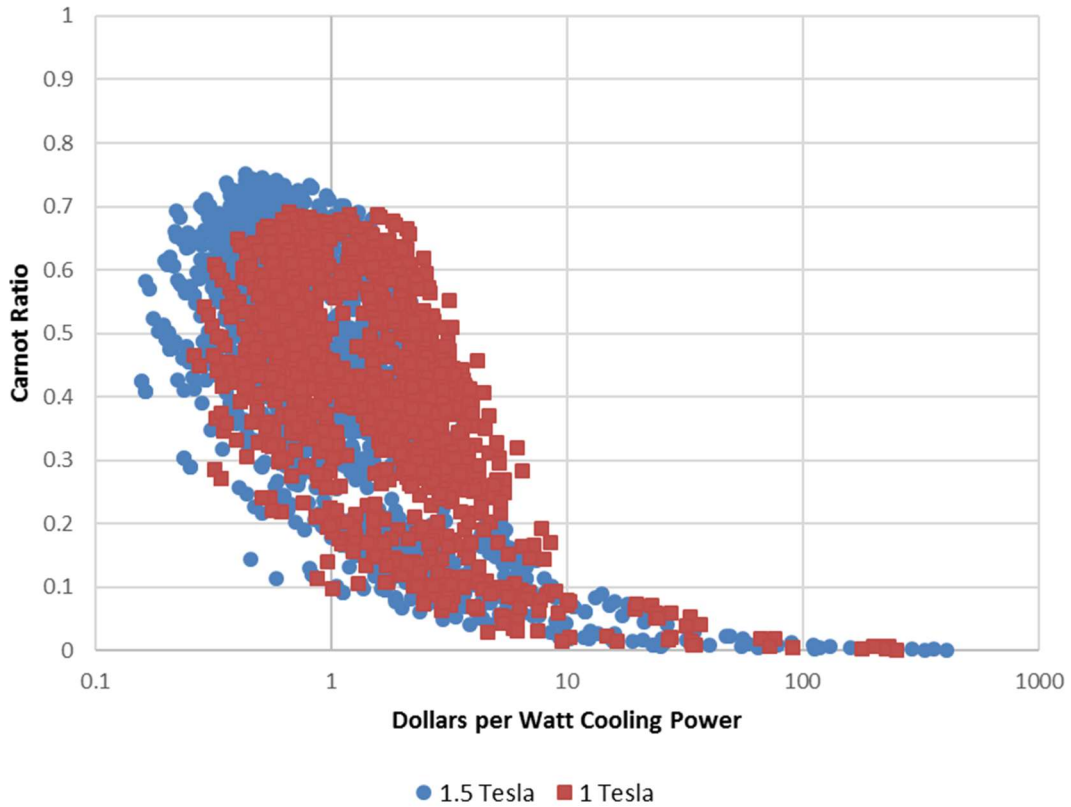
Figure 64: Carnot ratio as a function cost per Watt cooling power of MCM in the zero variation study, where the cost function is log scaled.

A clear distinction between magnetic field levels is apparent, with higher fields producing lower cost system at higher efficiency. The trend toward higher magnetic field levels for MCM cost is in direct contrast with the trend for magnetic system costs. Basic systems operating at 60% of Carnot COP cost about 0.16 dollars per Watt of Cooling, and high performing system at 72% of Carnot COP cost double that. Therefore, total

MCM cost for 150 W cooling ranges from $24 to $50 for the same respective system designs. This is about 3% of the cost of magnetic materials for the same size system.

Other components such as the motor, pump, controls, valves, lines, etcetera can be estimated to cost $80 additional (Langebach et al., 2014). A basic magnetocaloric system achieving 60% of Carnot COP would cost a total of $404 with magnets, regenerator, and other components totaled. A system achieving 75% of Carnot COP is estimated to cost $3080. Total system cost for a vapor compression system can be estimated at $64 (Langebach et al., 2014), which is greatly exceeded by even the lowest cost magnetocaloric system.

6.3 – Split Regenerator System Cost

One exemplative method to reduce cost greatly is to implement a split system, where 2 unique and independent regenerators operate concurrently across different temperature spans. Patents exist for such systems, although implementation can vary greatly. For example, patent number US20190024952 discloses a positive displacement hydraulic system utilizing 2 heat transfer fluids (Schroeder and Benedict, 2017).
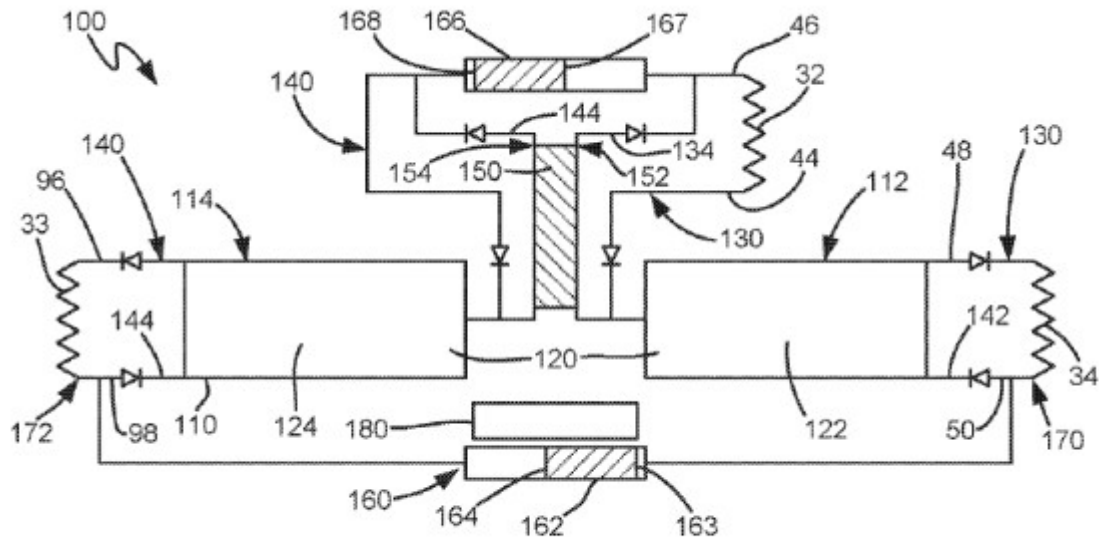
FIG. 4

Figure 65: Figure 1 of US20190024952, depicting a split magnetocaloric system (Schroeder and Benedict, 2017).

In Figure 65, regenerators 124 and 122 are connected to each other thermally via heat exchanger 150, but separated hydraulically. Such a system allows better heat transfer fluids, such as water, to be used on a large portion of the total span. Water has a higher heat capacity and lower viscosity than most alternatives. For example, water would work well as a heat transfer fluid from 105 F down to 40 F or slightly below, having a freezing point of 32 F. This regenerator would reject heat via heat exchanger 34, and absorb heat from heat exchanger 150 and 32. Glycol or another fluid with a much lower freezing point would operate between 45 F and -10 F, would reject heat to the water-containing regenerator via heat exchanger 150, and would absorb heat from heat exchanger 33. In order to cool a fresh food compartment down to 35 F, the warmer regenerator section would likely need a small amount of freezing point suppression, but could still reap many of the same rewards as can be found with pure water.

117

In order to assess the improvement of a split system, a small set of case studies was performed as in section 4.1, but without the extensive analysis, simply to provide a realistic relationship between predicted costs and material variability level, to be shown in Figure 61. For the example cases, channel size was restricted to 100 μm because it was by far the most successful size in Chapter 4. Length was restricted to 0.075 m per section and the highest levels of magnetization time and flow ramp time were omitted because the best designs in Chapter 4 did not use the highest respective levels of each. Each of the two regenerator sections contains 25 stages, which maintains similar stage temperature spacing to Chapter 4 studies. Otherwise, parametric levels were retained from Chapter 4 using zero material property variation. The simulation tool described in Chapter 2 was simply run twice to account for each of the two regenerators in the split system. As in chapter 4, the design parameters do not deviate substantially away from validated ranges. Substantial improvements in both Carnot ratio and cooling power density were observed. The coldest portion of the split system has an average cooling power density that is 35% lower than the warmer portion using the same design and operational parameters. Ratio of Carnot COP is 20% lower for the cooler portion than the warmer portion. The water-containing, warmer span, regenerator section is predicted to be both more efficient and more powerful than the colder regenerator section in this small set of example cases.
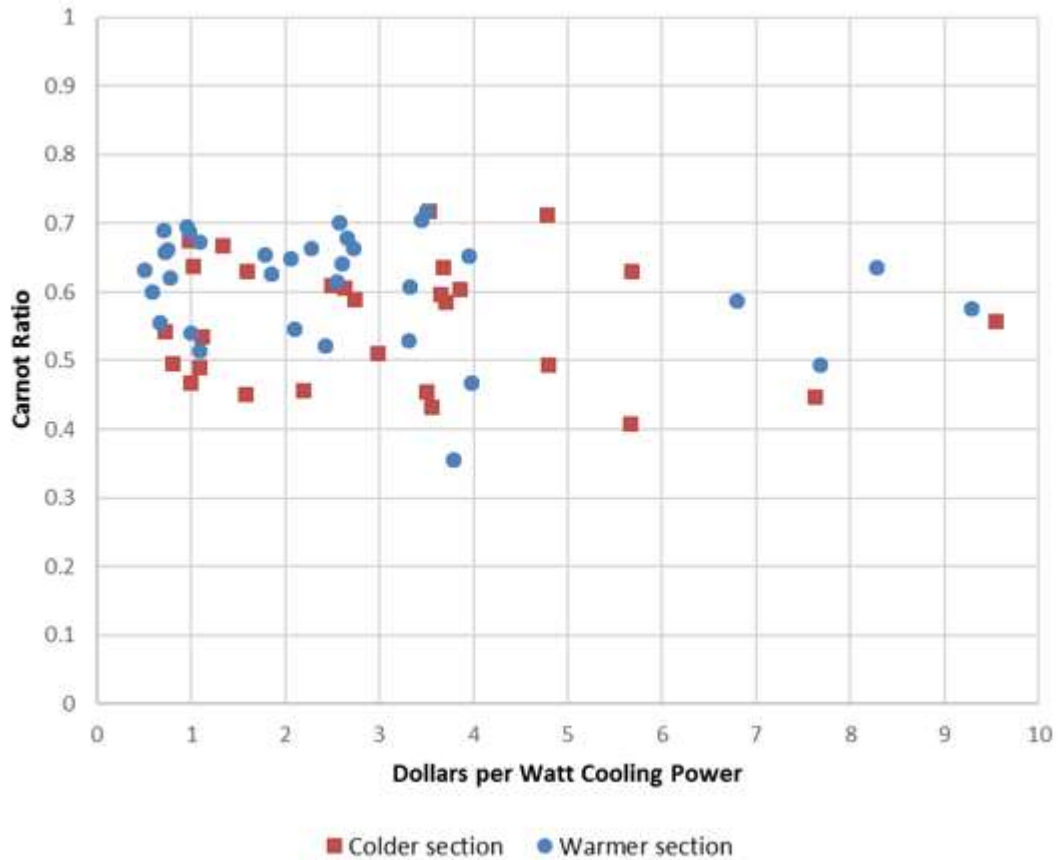
Figure 66: Magnet cost function versus Carnot ratio for the colder regenerator section and colder regenerator section.

Figure 66 shows a points cloud that is much less densely populated than Figure 34, Figure 42, or Figure 47, and shows the same relationship for non-split systems without and with variability. However, designs achieving more than 70% of Carnot COP are still present in both parts of the split regenerator system. For the hypothetical system with 150 W of cooling needed, we can approximate a 50% split between the freezer and fresh food compartments. Approximately half of the cooling load is used by the freezer compartment, and half by the fresh food compartment. In this case only 75 W of cooling will be necessary for the coldest portion of the split system, directly removing 25% of total magnetic system cost by a reduction in regenerator volume by

25%. By selecting low individual designs from the points in Figure 66, a total system

efficiency can be deduced. First, rejected heat from each section is calculated as

$$Q_{out} = \frac{Q_{in}}{COP} + Q_{in}$$
(50)

where Q_{out} is rejected heat in Watts, Q_{in} is absorbed heat in Watts, and COP is

coefficient of performance. Q_{in} is determined by freezer cooling needs, 75 W, for the

colder section. For the warmer section,

$$Q_{out} = \frac{\left(Q_{out_{FZ}} + Q_{FF}\right)}{COP_{FF}} + Q_{out_{FZ}} + Q_{FF}$$
(51)

where $Q_{out_{FZ}}$ is rejected heat from the colder section, Q_{FF} is fresh food cooling

requirements, and COP_{FF} is fresh food regenerator coefficient of performance.

	Q HX (W)	COP	COP Carnot	Carnot Ratio	Q in (W)	Q out (W)	Cost Ftn ($/W)	Mag cost ($)	MCM cost ($)
Freezer	75	4.5	8.175	55%	75	91.7	1	75	14
Fresh food	75	4.85	7.687	63%	166.7	201.0	0.5	83	16
Total System	150	2.94	3.91	75%	150	201.0	1.06	158	29

Table 11: Comparison of split system performance and cost to baseline un-split systems with zero material variation.

Table 11 shows the performance and cost of a split system operating at 75% of

Carnot COP, which is only which is only $187 in estimated cost for the magnetic system

and regenerator materials. Adding other components brings this total $267 (Langebach

et al., 2014). Non-split magnetocaloric systems are more than 10 times more expensive

than split systems with equivalent efficiency and cooling power. The overall split system

uses less energy than a non-split system due to the thermodynamic improvements and

load balancing. By running the same set of split system design points with multiple

120

levels of variation, a relationship can be shown for system magnetic and regenerator

cost versus material variation level at 75% of Carnot COP.
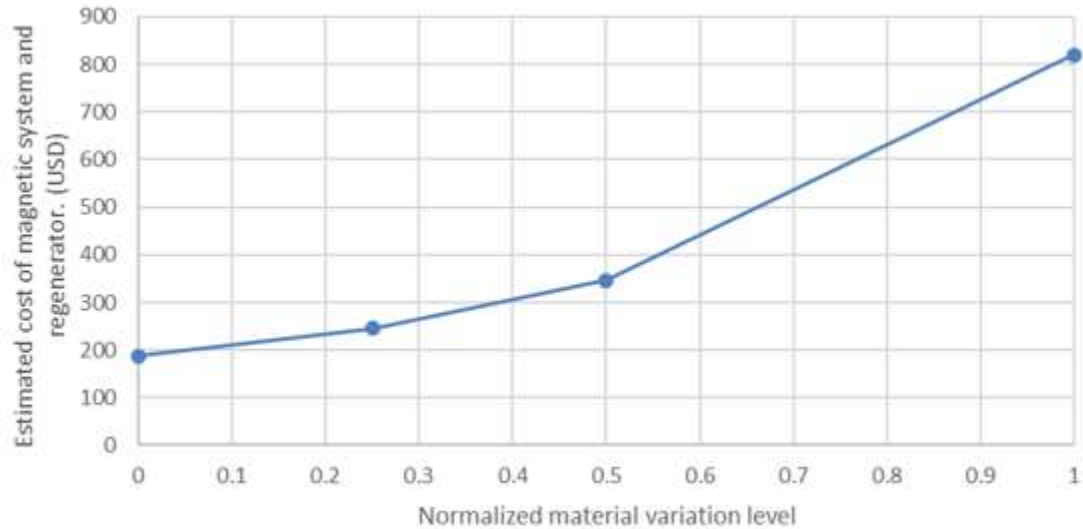
Figure 67: System estimated cost as a function of material property variation level, including only magnet material and magnetocaloric material costs.

Figure 67 shows a massive impact to cost related to material property variation,

with diminishing returns as zero variation is approached. Material variability inflates

projected heat pump cost by 400%, from about $200 to $800 when comparing existing

material variation levels to zero material property variation. A 50% reduction in material

properties results in 57% cost reduction. An additional 50% reduction (25% of the

original level) results in 29% additional reduction (70% total reduction from baseline).

Most importantly the total system cost begins to approach levels that may entice

businesses to adopt this technology. Another cost-benefit relationship exists when

considering the process to produce magnetocaloric material, which could conceivably

become costlier in order to reduce property variation. This is a separate but closing

related issue that could be addressed with additional research.

Figure 67 represents only magnetic and MCM cost, but it shows that there are very large improvements to be made to basic systems to make them work well from a cost perspective. Negative aspects of a split system relate to system complexity. A split system requires a more substantial hydraulic system and an extra heat exchanger, as well as the hardware needed to mechanically operate 2 distinct magnetic and regenerative systems. The cost and complexity addition in using a split system is likely overwhelmed by the cost savings. A Loss waterfall plot puts regenerator losses into perspective in Figure 68.
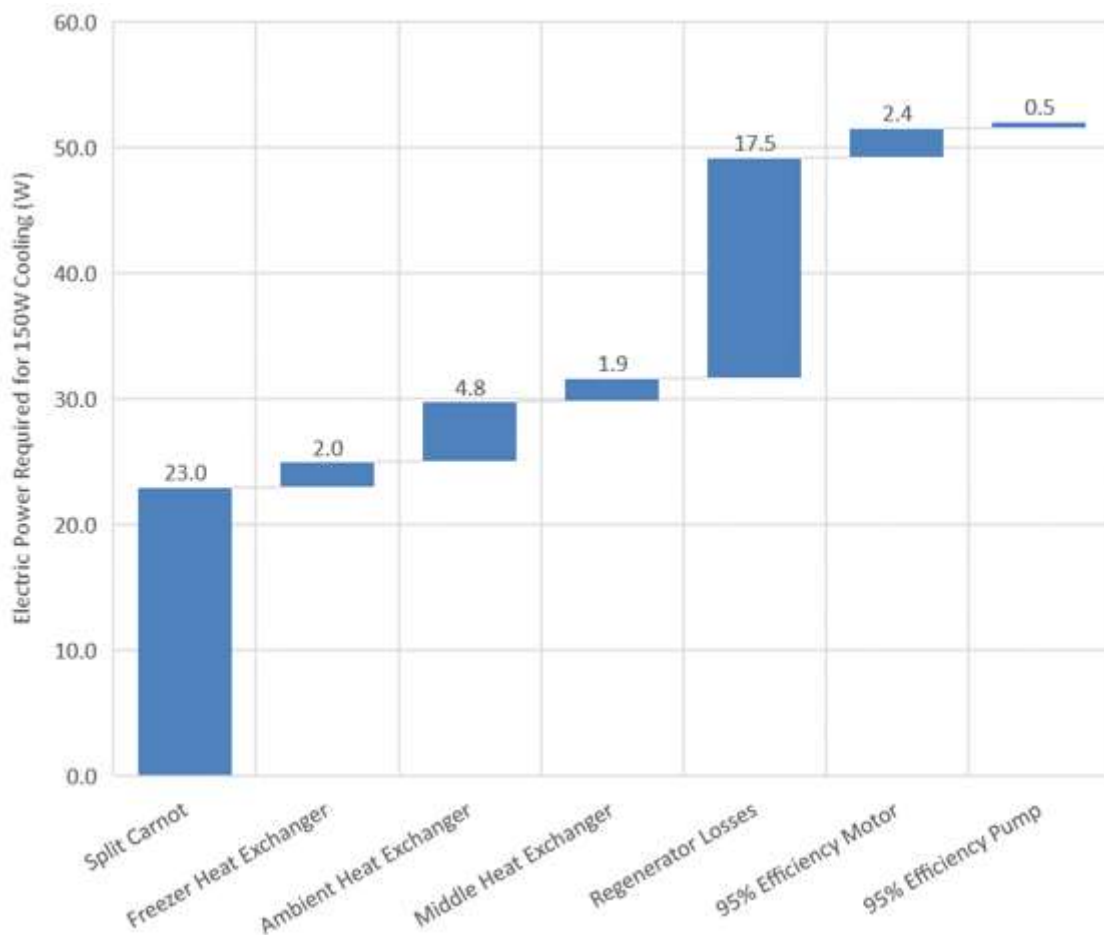
Figure 68: Loss waterfall, showing power requirement additions for a Carnot cycle, heat exchangers, and regenerator, motor, and pump losses.

A split Carnot cycle operating at 0 F, 40 F, and 90 F for heat exchanger

temperatures requires 23 W of energy input to produce 150 W of total cooling. This

represents the lower limit for such a system, and all components add electrical energy

draw to the appliance by decreasing COP. Heat exchangers add power input based on

changes to the Carnot COP calculation; equation 32.

$$COP_{Carnot} = \frac{T_{cold}}{T_{warm} - T_{cold}}$$ (31)

For example, adding a real freezer heat exchanger means that the heat pump must

absorb heat at -10 F rather than 0 F, the freezer air temperature. Regenerator losses

account for over 50% of total losses in Figure 68, showing a large opportunity for further

improvement. A relatively high efficiency pump and motor are much smaller

components, although still important to consider.

6.4 – Removing Design Constraints to Reduce Cost

A large amount of cost reduction and performance gain can likely be made by

removing design constraints. One such design constraint is a symmetric, or even, flow

profile, which has typically been assumed for research. An example of a design to

produce uneven flow can be found in patent number US9927155B2, which discloses a

planar rotating diverter valve for a magnetocaloric heat pump (Boeder et al., 2014).

Other design constraints to be explored include flow profile shape, cascade Curie

temperature profile, and cascade span (Monfared and Palm, 2015). These all strongly

affect efficiency and must be balanced together. Some design constants can be made

into functions of location, such as cross sectional area (Dall'Olio et al., 2017). A tapered

regenerator can provide benefits, such as having more cross sectional area on the

regenerator hot side, where more heat must flow as compared to the cold side.

Other design constants that can be made into variable functions of position include magnetic field strength, void fraction, channel diameter, and stage spacing or temperature gradient. Nearly any combination is possible assuming 3D printing will be used for production. By increasing the flexibility of the design an ideal balance can be found for the highest possible efficiency at a reasonable cost, taking material variability into consideration as well.

7 – CONCLUSIONS AND FUTURE WORK

7.1 - Conclusions

Within the present work a computer model was described which was used to simulate magnetocaloric regenerator performance based on various design parameters. A large design envelope study was performed for a cooling heat pump within a refrigerator, with 9 input parameters at 2 or 3 levels per parameter. The design point study showed maximum efficiencies of around 75% of Carnot COP measured at the regenerator ends. The model was extended to include random variation in magnetocaloric material properties based on normal distributions and standard deviations for material input parameters, which allowed realistic material variation to be simulated. Three levels of variation were used, based on measured data on several cascades of magnetocaloric material. Lower limit performance, which is the most relevant output, showed a 3% drop in maximum efficiency due to material variation at levels measured on real material. Maximum cooling power density also suffered a similar reduction. Average efficiency and cooling power density suffered a larger reduction, exceeding 10%. These results expand upon work by Lei et al. (2015) and Lei et al. (2016), and are largely in agreement. For instance, the inclusion of random variation of materials within the study leads to some cases exceeding the highest performing zero variation cases, but lower limit and average performance suffer.

A new cost model for magnetic material and magnetocaloric material was implemented, showing a basic magnetocaloric system cost to be over $300, achieving equivalent efficiency to vapor compression systems. Cost is projected to be greater than $1500 to achieve 20-30% improvements over existing technology having a single regenerator span. An innovation was described to split the system into 2 sections using 2 different heat transfer fluids, which brings the estimated price down below $200 for the magnetic system and regenerator of a system 30% more efficient than vapor compression systems if material variation is reduced to negligible levels. If material variability is not reduced, system cost exceeds $800 for a such a high efficiency system. Other approaches were also described in brief to bring cost down by even more, which all fall under the category of future work. In summary:

1. Large cascades of new and existing measured material data were compiled using existing methods to parameterize all material curves.

2. Linear functions to relate Split-Lorentzian curve parameters to material Curie temperature were fitted to be used in simulations.

3. Using an existing simulation tool, a broad design space of magnetocaloric regenerators were simulated, varying 9 input parameters across 2 or 3 levels each for a refrigerator application.

4. The simulation tool was modified to generate magnetocaloric cascades of material randomly based on new input parameters for material variation

5. Parameterized material data was used to simulate points using realistic material variability

6. Material variability was found to reduce average performance by about 10%, as measured by cooling power density and ratio of Carnot COP.

7. A new function was created to estimate required magnetic mass for any arbitrary magnetocaloric machine design based on magnetic field strength and regenerator volume. This is useful for future cost estimates of magnetocaloric machines.

8. A cost model was implemented, which showed that material variability inflates projected heat pump cost by 400%, from about $200 to $800.

7.2- Future Work

The field of magnetocalorics is open to continued research, much of it centered on machine design. Complexity of these magnetocaloric systems necessitates creative approaches to finding designs which are robust enough to perform with real material variation consistently. If computational power was limitless, a brute force approach would work well, simulating iterations on each design until lower limit performance converges. Although this was the approach of the present work, a realistic design search would be exponentially larger than the present work. More levels would be needed for all parameters to find an ideal design. Therefore, there is a good opportunity to develop optimization strategies to allow a short path to commercialization, such as using genetic algorithms (Lei et al., 2015). Future work will need to address sensitivity to fluctuations in absorption and rejection temperatures and pull down time, because real applications need to cool a load from room temperature under a variety of environmental conditions. Additional work could also be done to reduce costs for machines, which in turn makes the technology more attractive for businesses. This may include additional study of split systems and other innovative machine concepts.

REFERENCES

Amaral, J.S., Tavares, P.B., Reis, M.S., Araújo, J.P., Mendonça, T.M., Amaral, V.S., Vieira, J.M., 2008. The effect of chemical distribution on the magnetocaloric effect: A case study in second-order phase transition manganites. J. Non. Cryst. Solids 354, 5301–5303. https://doi.org/10.1016/j.jnoncrysol.2008.05.078

Aprea, C., Greco, A., Maiorino, A., Masselli, C., 2015. A comparison between rare earth and transition metals working as magnetic materials in an AMR refrigerator in the room temperature range. Appl. Therm. Eng. 91, 767–777. https://doi.org/10.1016/j.applthermaleng.2015.08.083

Aprea, C., Greco, A., Maiorino, A., Mastrullo, R., Tura, A., 2014. Initial experimental results from a rotary permanent magnet magnetic refrigerator. Int. J. Refrig. 43, 111–122. https://doi.org/10.1016/j.ijrefrig.2014.03.014

Bahl, C.R.H., Engelbrecht, K., Eriksen, D., Lozano, J.A., Bjørk, R., Geyti, J., Nielsen, K.K., Smith, A., Pryds, N., 2014. Development and experimental results from a 1 kW prototype AMR. Int. J. Refrig. 37, 78–83. https://doi.org/10.1016/j.ijrefrig.2013.09.001

Barclay, J. ~A., 1983. Theory of an active magnetic regenerative refrigerator. NASA Conf. Publ. https://doi.org/10.1017/CBO9781107415324.004

Barcza, A., Katter, M., Zellmann, V., Russek, S., Jacobs, S., Zimm, C., 2011. Stability
and magnetocaloric properties of sintered La(Fe, Mn, Si) 13Hz alloys. IEEE Trans.
Magn. 47, 3391–3394. https://doi.org/10.1109/TMAG.2011.2147774

Basso, V., Küpferling, M., Curcio, C., Bennati, C., Barzca, A., Katter, M., Bratko, M.,
Lovell, E., Turcaud, J., Cohen, L.F., 2015. Specific heat and entropy change at the
first order phase transition of La(Fe-Mn-Si)13-H compounds. J. Appl. Phys. 118,
053907. https://doi.org/10.1063/1.4928086

Benedict, M. A., Sherif, S.A., Beers, D.G., Schroeder, M., 2016a. Un nouveau modèle
de matériaux magnétocaloriques de premier ordre avec une validation
expérimentale. Int. J. Refrig. 70, 138–147.
https://doi.org/10.1016/j.ijrefrig.2016.07.001

Benedict, Michael A., Sherif, S.A., Beers, D.G., Schroeder, M.G., 2016b. Design and
performance of a novel magnetocaloric heat pump. Sci. Technol. Built Environ. 22,
520–526. https://doi.org/10.1080/23744731.2016.1185889

Benedict, M.A., Sherif, S.A., Schroeder, M., Beers, D.G., 2017a. The impact of
magnetocaloric properties on refrigeration performance and machine design. Int. J.
Refrig. 74, 576–583. https://doi.org/10.1016/j.ijrefrig.2016.12.004

Benedict, M A, Sherif, S.A., Schroeder, M., Beers, D.G., 2016c. The impact of
magnetocaloric properties on refrigeration performance and machine design
L'impact des propriétés magnétocaloriques sur la performance frigorifique et la
conception de machine. Int. J. Refrig. 74, 574–581.
https://doi.org/10.1016/j.ijrefrig.2016.12.004

Benedict, M.A., Sherif, S.A., Schroeder, M.G., Beers, D.G., 2016d. Experimental Impact

of Magnet and Regenerator Design on the Refrigeration Performance of First-Order Magnetocaloric Materials. Int. J. Refrig. 74, 188–197. https://doi.org/10.1016/j.ijrefrig.2016.09.023

Bjørk, R., 2010. Designing a magnet for magnetic refrigeration.

Bjørk, R., Bahl, C.R.H., Nielsen, K.K., 2016. The lifetime cost of a magnetic refrigerator. Int. J. Refrig. 63, 48–62. https://doi.org/10.1016/j.ijrefrig.2015.08.022

Bjørk, R., Bahl, C.R.H., Smith, A., Pryds, N., 2010. Review and comparison of magnet designs for magnetic refrigeration. Int. J. Refrig. 33, 437–448. https://doi.org/10.1016/j.ijrefrig.2009.12.012

Blázquez, J.S., Moreno-Ramírez, L.M., Ipus, J.J., Kiss, L.F., Kaptás, D., Kemény, T., Franco, V., Conde, A., 2015. Effect of α-Fe impurities on the field dependence of magnetocaloric response in LaFe$_{11.5}$Si$_{1.5}$. J. Alloys Compd. 646, 101–105. https://doi.org/10.1016/j.jallcom.2015.06.085

Boeder, A., Chell, J., Jacobs, S., Leonard, J.P., Auringer, J., 2014. Magnetic refrigeration system with unequal blows. US9927155B2.

Brown, G. V., 1976. Magnetic heat pumping near room temperature. J. Appl. Phys. 47, 3673–3680. https://doi.org/10.1063/1.323176

BUH, J., 2010. The Magnetocaloric Effect and Magnetocaloric Materials. Univerza v Ljubljani.

Burriel, R., Sazatornil, M., Palacios, E., Barcza, A., Katter, M., 2011. Accurate determination of the magnetocaloric parameters of LaFeCoSi compounds, in: Refrigeration Science and Technology.

Conti, J.J., Holtberg, P.D., Diefenderfer, J.R., Napolitano, S.A., Schaal, M., Turnure, J.T., Westfall, L.D., 2014. Annual Energy Outlook 2014. Annu. Energy Outlook 1–269. https://doi.org/10.1007/s13398-014-0173-7.2

Dall'Olio, S., Lei, T., Engelbrecht, K., Bahl, C.R.H., 2017. Effet de l'effilage sur le lit d'un régénérateur magnétocalorique. Int. J. Refrig. 84, 300–308. https://doi.org/10.1016/j.ijrefrig.2017.08.012

Dan'kov, S., Tishin, a., Pecharsky, V., Gschneidner, K., 1998. Magnetic phase transitions and the magnetothermal properties of gadolinium. Phys. Rev. B 57, 3478–3490. https://doi.org/10.1103/PhysRevB.57.3478

Dinesen, a R., Linderoth, S., Mørup, S., 2005. Direct and indirect measurement of the magnetocaloric effect in La 0.67 Ca 0.33− x Sr x MnO 3 ± δ (). J. Phys. Condens. Matter 17, 6257–6269. https://doi.org/10.1088/0953-8984/17/39/011

Engelbrecht, K., 2008. A Numerical Model of an Active Magnetic Regenerator Refrigerator with Experimental Validation by.

Engelbrecht, K., 2004. A numerical model of an active magnetic regenerator refrigeration system 280.

Engelbrecht, K., Bahl, C.R.H., 2010. Evaluating the effect of magnetocaloric properties on magnetic refrigeration performance. J. Appl. Phys. 108. https://doi.org/10.1063/1.3525647

Engelbrecht, K., Bahl, C.R.H., Nielsen, K.K., 2011. Experimental results for a magnetic refrigerator using three different types of magnetocaloric material regenerators. Int. J. Refrig. 34, 1132–1140. https://doi.org/10.1016/j.ijrefrig.2010.11.014

Engelbrecht, K., Nielsen, K.K., Bahl, C.R.H., Carroll, C.P., van Asten, D., 2013. Material

   properties and modeling characteristics for MnFeP[sub 1−x]As[sub x] materials for

   application in magnetic refrigeration. J. Appl. Phys. 113, 173510.

   https://doi.org/10.1063/1.4803495

Gschneider Jr., K.A., Pecharsky, V.K., Tsokol, A.O., 2005. Recent developments in

   magnetocaloric materials. Reports Prog. Phys. 68, 1479–1539.

   https://doi.org/10.1088/0034-4885/68/6/R04

Hausen, H.A., 1943. No Title. VDI Beih Verfahrenstech 91.

Jacobs, S., Auringer, J., Boeder, A., Chell, J., Komorowski, L., Leonard, J., Russek, S.,

   Zimm, C., 2014. The performance of a large-scale rotary magnetic refrigerator. Int.

   J. Refrig. 37, 84–91. https://doi.org/10.1016/j.ijrefrig.2013.09.025

Jeppesen, S., Linderoth, S., Pryds, N., Kuhn, L.T., Jensen, J.B., 2008. Indirect

   measurement of the magnetocaloric effect using a novel differential scanning

   calorimeter with magnetic field. Rev. Sci. Instrum. 79, 1–5.

   https://doi.org/10.1063/1.2957611

Kaeswurm, B., Barcza, A., Vögler, M., Geiger, P.T., Katter, M., Gutfleisch, O., Cohen,

   L.F., 2016. Behaviour of the Young's modulus at the magnetocaloric transition in

   La(Fe,Co,Si)13. J. Alloys Compd. 697, 427–433.

   https://doi.org/10.1016/j.jallcom.2016.11.360

Katter, M., Zellmann, V., Reppel, G.W., Uestuener, K., 2008. Magnetocaloric Properties

   of La(Fe, Co, Si)(13) Bulk Material Prepared by Powder Metallurgy. Ieee Trans.

   Magn. 44, 3044–3047. https://doi.org/10.1109/TMAG.2008.2002523

132

Langebach, R., Klaus, M., Haberstroh, C., Hesse, U., 2014. Magnetocaloric Cooling
    Near Room Temperature - A Status Quo with Respect to Household Refrigeration.
    Int. Refrig. Air Cond. Conf.

Lei, T., Engelbrecht, K., Nielsen, K.K., Neves Bez, H., Bahl, C.R.H., 2016. Study of
    multi-layer active magnetic regenerators using magnetocaloric materials with first
    and second order phase transition. J. Phys. D. Appl. Phys. 49, 345001.
    https://doi.org/10.1088/0022-3727/49/34/345001

Lei, T., Nielsen, K.K., Engelbrecht, K., Bahl, C.R.H., Neves Bez, H., Veje, C.T., 2015.
    Sensitivity study of multi-layer active magnetic regenerators using first order
    magnetocaloric material La(Fe,Mn,Si)13Hy. J. Appl. Phys. 118, 014903.
    https://doi.org/10.1063/1.4923356

Marcos, J., Casanova, F., Batlle, X., Labarta, A., Planes, A., Mañosa, L., 2003. A high-
    sensitivity differential scanning calorimeter with magnetic field for
    magnetostructural transitions. Rev. Sci. Instrum. 74, 4768–4771.
    https://doi.org/10.1063/1.1614857

Momen, A.M., 2017. Magnetocaloric Refrigerator Freezer Project Outcome. Oak Ridge,
    TN.

Monfared, B., Palm, B., 2015. Optimization of layered regenerator of a magnetic
    refrigeration device. Int. J. Refrig. 57, 103–111.
    https://doi.org/10.1016/j.ijrefrig.2015.04.019

Morrison, K., Sandeman, K.G., Cohen, L.F., Sasso, C.P., Basso, V., Barcza, A., Katter,
    M., Moore, J.D., Skokov, K.P., Gutfleisch, O., 2012. Evaluation of the reliability of
    the measurement of key magnetocaloric properties: A round robin study of

La(Fe,Si,Mn)H ?? conducted by the SSEEC consortium of European laboratories, in: International Journal of Refrigeration. pp. 1528–1536. https://doi.org/10.1016/j.ijrefrig.2012.04.001

Nieto de Castro, C.., Lourenço, M.J.., Sampaio, M.., 2000. Calibration of a DSC: its importance for the traceability and uncertainty of thermal measurements. Thermochim. Acta 347, 85–91. https://doi.org/10.1016/S0040-6031(99)00420-7

Pecharsky, V.K., Gschneidner Jr, K.A., 1999. Magnetocaloric effect and magnetic refrigeration. J. Magn. Magn. Mater. 200, 44–56. https://doi.org/10.1016/S0304-8853(99)00397-2

Pecharsky, V.K., Jr, K. a G., 1999. Magnetocaloric e ! ect and magnetic refrigeration 200, 44–56.

Pecharsky, V.K., Pecharsky, V.K., Gschneidner, K.A., Gschneidner, K.A., Pecharsky, A.O., Tishin, A.M., 2001. Thermodynamics of the magnetocaloric effect. Phys. Rev. B - Condens. Matter Mater. Phys. 64, 1444061–14440613. https://doi.org/10.1103/PhysRevB.64.144406

Pryds, N., Clemens, F., Menon, M., Nielsen, P.H., Brodersen, K., Bjørk, R., Bahl, C.R.H., Engelbrecht, K., Nielsen, K.K., Smith, A., 2011. A monolithic perovskite structure for use as a magnetic regenerator. J. Am. Ceram. Soc. 94, 2549–2555. https://doi.org/10.1111/j.1551-2916.2011.04398.x

Rowe, A., Tura, A., 2006. Experimental investigation of a three-material layered active magnetic regenerator. Int. J. Refrig. 29, 1286–1293. https://doi.org/10.1016/j.ijrefrig.2006.07.012

Russek, S.L., Zimm, C.B., 2006. Potential for cost effective magnetocaloric air conditioning systems. Int. J. Refrig. 29, 1366–1373. https://doi.org/10.1016/j.ijrefrig.2006.07.019

Sager, R., Paulson, D., 1982. REGENERATION EXPERIMENTS BELOW 10K IN A REGENERATIVE-CYCLE CRYOCOOLER, in: Gasser, M. (Ed.), Ref Rigeration for Cryogenic Sensors. Goddard Space Flight Center, Greenbelt, Maryland, pp. 81–95.

Schroeder, M., 2014. Transient heat transfer between a magnetocaloric packed particle bed and stagnant interstitial fluid. Electron. Theses Diss. https://doi.org/http://dx.doi.org/10.18297/etd/1782

Schroeder, M., Benedict, M., 2017. Refrigerator appliance with a caloric heat pump. US20190024952.

Schroeder, M.G., Brehob, E., 2016. A flexible numerical model of a multistage active magnetocaloric regenerator. Int. J. Refrig. 65, 250–257. https://doi.org/10.1016/j.ijrefrig.2016.01.023

Smith, A., Nielsen, K.K., Bahl, C.R.H., 2014. Scaling and universality in magnetocaloric materials. Phys. Rev. B - Condens. Matter Mater. Phys. 90, 1–17. https://doi.org/10.1103/PhysRevB.90.104422

Tishin, A.M., Spichkin, Y.I., 2003. The magnetocaloric effect and its applications. Institute of Physics Pub.

Tura, A., Rowe, A., 2014. Concentric Halbach cylinder magnetic refrigerator cost optimization. Int. J. Refrig. 37, 106–116.

https://doi.org/10.1016/j.ijrefrig.2013.09.005

Tura, A., Rowe, A., 2011. Permanent magnet magnetic refrigerator design and experimental characterization. Int. J. Refrig. 34, 628–639. https://doi.org/10.1016/j.ijrefrig.2010.12.009

U.S. Department of Energy, 2012. Buildings energy databook. Energy Effic. Renew. Energy Dep. 286.

von Ranke, P.J., de Oliveira, N.A., Alho, B.P., Plaza, E.J.R., de Sousa, V.S.R., Caron, L., Reis, M.S., 2009. Understanding the inverse magnetocaloric effect in antiferro- and ferrimagnetic arrangements. J. Phys. Condens. Matter 21, 056004. https://doi.org/10.1088/0953-8984/21/5/056004

Wang, C., Long, Y., Ma, T., Fu, B., Ye, R., Chang, Y., Hu, F., Shen, J., 2011. The hydrogen absorption properties and magnetocaloric effect of La0.8Ce0.2(Fe1−xMnx)11.5Si1.5Hy. J. Appl. Phys. 109, 07A910. https://doi.org/10.1063/1.3549560

Yibole, H., Guillou, F., Zhang, L., van Dijk, N.H., Brück, E., 2014. Direct measurement of the magnetocaloric effect in MnFe(P, X)(X = As, Ge, Si) materials. J. Phys. D. Appl. Phys. 47, 075002. https://doi.org/10.1088/0022-3727/47/7/075002

Zhang, T., Wang, C. yong, Li, L., Zhang, Y., Liu, C. lan, 2017. Mass production of magnetocaloric LaFeMnSiB alloys with hydrogenation. J. Iron Steel Res. Int. 24, 462–468. https://doi.org/10.1016/S1006-706X(17)30070-5

APPENDIX I – FITTED LORENTZIAN DATA FOR LaFeSiH-1 CASCADE

Stage	dT Peak (K)	T Peak (K)	HWHM (K)
1	2.51	264	6.25
2	2.42	265.5	6
3	2.86	267.4	5.1
4	2.6	268.7	5.65
5	2.67	270.3	5.6
6	2.77	271.3	5.6
7	2.88	273.1	5.4
8	2.76	274.8	5.35
9	2.87	276.3	5.3
10	2.93	276.9	5.1
11	2.87	278.3	5.1
12	3.01	280.1	4.9
13	3.18	281.6	4.85
14	3.12	283.2	4.75
15	3.16	284.6	4.8
16	3.21	286	4.55
17	3.25	287.6	4.45
18	3.36	289	4.55
19	3.46	289.9	3.95
20	3.24	291.8	4.45
21	3.13	293.2	4.6
22	3.04	294.7	4.75

23	3.21	296.5	4.45
24	3.25	297.6	4.45
25	3.24	299	4.45
26	3.31	301	4.2
27	3.7	302	3.7
28	3.35	303.7	4.3
29	3.29	305.4	4.45
30	3.41	306.8	4.35
31	3.45	308.3	4.15
32	3.31	310.4	4.25
33	3.43	314.4	3.95

APPENDIX II – FITTED LORENTZIAN DATA FOR LaFeSiH-2 CASCADE

Stage	dT Peak (K)	T Peak (K)	HWHM (K)
1	4.12	310.84	6.81
2	4.76	309.84	5.34
3	4.16	308.87	5.84
4	4.24	307.66	6.51
5	4.41	306.17	6.12
6	4.79	305.18	5.36
7	4.52	304.55	5.87
8	4.4	303.37	5.98
9	4.52	302.25	5.88
10	4.05	301.36	7.14
11	4.06	300.25	6.95
12	3.97	299.38	6.88
13	3.99	298.41	6.78
14	3.68	296.78	7.81
15	3.76	296.4	8.1
16	4.23	295.81	6.59
17	3.99	294.9	6.92
18	4.18	293.79	5.56
19	3.99	292.38	7.35
20	4.05	290.91	7.48
21	3.91	290.67	7.62
22	3.96	289.64	7.59
23	3.96	288.64	7.69

24	4.07	287.44	7.61
25	3.65	286.92	7.96
26	3.67	285.78	8.17
27	3.62	285.01	8.51
28	3.79	283.7	8.17
29	3.56	282.82	8.6
30	3.76	281.13	7.52
31	3.58	280.05	8.32
32	3.42	279.71	9.52
33	3.24	278.57	10.18
34	3.35	277.35	9.2
35	3.2	276.34	9.08
36	3.36	275.12	8.49
37	3.11	274.22	9.26
38	3.24	273.11	9.1
39	3.24	272.01	9.23
40	3.23	271.07	9.44
41	3.2	269.87	9.67
42	3.13	269.81	10.34
43	3.13	268.86	9.81
44	3.16	267.93	9.78
45	3.14	266.94	9.83
46	3.1	265.51	9.9
47	2.91	264.61	10.11
48	2.99	263.76	10.81
49	2.98	262.63	10.8
50	2.76	260.96	11.61
51	2.76	260	11.6
52	2.64	259.37	11.53
53	2.73	258.04	11.85
54	2.73	257.01	11.91
55	2.66	255.74	12.01
56	2.58	254.47	12.03

APPENDIX III – LIST OF ACRONYMS

AMR: Active magnetocaloric regenerator

COP: Coefficient of performance

MCM: Magnetocaloric material

MCE: Magnetocaloric effect

FOPT: First order phase transition

SOPT: Second order phase transition

HWHM: Half width at half max

FWHM: Full width at half max

CURRICULUM VITAE

NAME: Michael Goodman Schroeder

ADDRESS: 12301 Center Grove ln, #109

Louisville, KY 40223

DOB: August 11, 1988 – Lima, OH

EDUCATION: B.S., Mechanical Engineering

University of Toledo

2007 – 2011

M.S., Mechanical Engineering

University of Louisville

2012 – 2014

PATENTS: 69 filed and 27 granted at the time of writing. Topics include

magnetocaloric technology, heat exchangers, image analysis, refrigerator

features, dishwasher wash systems, and more.

INDUSTRY

EXPERIENCE:

Engineering co-op, General Electric Appliances - Louisville, KY

2009 to 2011 – Dishwasher energy reduction, clothes washer new product hydraulic system design, dishwasher wash system development, magnetocaloric machine modeling and design.

Edison Engineering Development Program, GE Appliances - Louisville, KY

2012 to 2015 – Front load washers out of balance detection software, dryer algorithmic optimization, refrigeration sealed systems advanced development, computer aided design team. Created interstitial heat thermo-fluid model for magnetocaloric packed beds.

Magnetocaloric Research Team, GE Appliances - Louisville, KY

2015 to 2017 - System modeling and experimentation, heat transfer modeling and experimentation, machine design and optimization. Assess various new heat pump technologies for GE Appliances. Managed research agreement between Oak Ridge National Labs and GE Appliances. Presented magnetocaloric paper at Purdue HVAC conference.

Refrigeration Advanced Systems Team, GE Appliances - Louisville, KY

2017 to 2019 - Magnetocaloric research, design, and modeling, heat leak modeling, refrigeration feature development. Assess

various new heat pump technologies for GE Appliances.

Managed a second research agreement between Oak Ridge

National Labs and GE Appliances. Recognized as technical

expert in alternative heat pump technologies and modeling.

PUBLICATIONS ("REFERENCES" SECTION SHOWS ADDITIONAL INFORMATION):

Transient heat transfer between a magnetocaloric packed particle bed and stagnant interstitial fluid (Schroeder, 2014)

A flexible numerical model of a multistage active magnetocaloric regenerator (Schroeder and Brehob, 2016a)

A new model of first-order magnetocaloric materials with experimental validation (Benedict et al., 2016b)

Design and performance of a novel magnetocaloric heat pump (Michael A. Benedict et al., 2016c)

The impact of magnetocaloric properties on refrigeration performance and machine design (Benedict et al., 2017a)

Experimental impact of magnet and regenerator design on the refrigeration performance of first-order magnetocaloric materials (M.A. Benedict et al., 2016d)